



## City Research Online

### City, University of London Institutional Repository

---

**Citation:** Zhang, Z. Y. (1993). Fibre optic fluorescence thermometry. (Unpublished Doctoral thesis, City, University of London)

This is the accepted version of the paper.

This version of the publication may differ from the final published version.

---

**Permanent repository link:** <https://openaccess.city.ac.uk/id/eprint/29636/>

**Link to published version:**

**Copyright:** City Research Online aims to make research outputs of City, University of London available to a wider audience. Copyright and Moral Rights remain with the author(s) and/or copyright holders. URLs from City Research Online may be freely distributed and linked to.

**Reuse:** Copies of full items can be used for personal research or study, educational, or not-for-profit purposes without prior permission or charge. Provided that the authors, title and full bibliographic details are credited, a hyperlink and/or URL is given for the original metadata page and the content is not changed in any way.

FIBRE OPTIC FLUORESCENCE  
THERMOMETRY

by

ZHI YI ZHANG

A thesis submitted for the degree of  
Doctor of Philosophy

CITY UNIVERSITY

Department of Electrical, Electronic  
and Information Engineering

August 1993

# Table of Contents

---

---

Table of Contents.....	2
List of Tables.....	5
List of Figures.....	6
Acknowledgements.....	13
Declaration.....	14
Abstract.....	15
Symbols and Abbreviations.....	16
1. Fibre Optic Fluorescence Thermometry: Introduction.....	19
1.1. Introduction.....	19
1.2. Fibre optic temperature measurement.....	20
1.2.1. Historical overview.....	20
1.2.2. Advantages of fibre optic temperature measurement.....	21
1.2.3. Sensor devices.....	23
1.3. Fluorescence-based fibre optic thermometry.....	30
1.3.1. Photoluminescence.....	30
1.3.2. Early fluorescence thermometer schemes.....	33
1.3.3. Fluorescence lifetime-based schemes.....	35
1.3.3.1. Pulse measurement of fluorescence lifetime.....	36
1.3.3.2. Phase and modulation measurement.....	41
1.3.3.3. Phase-locked detection of fluorescence lifetime.....	42
1.4. Structure of the thesis.....	47
1.5. Aims and objectives of the thesis.....	48
2. Temperature Dependences of Cr <sup>3+</sup> Fluorescence Lifetimes.....	49
2.0. Abstract.....	49
2.1. Introduction.....	50
2.2. Temperature dependence of Cr <sup>3+</sup> fluorescence in low field crystals.....	52
2.3. Temperature dependence of Cr <sup>3+</sup> fluorescence in high field crystals.....	57
2.3.1. Two level model for the Cr <sup>3+</sup> fluorescence in high fields.....	57
2.3.2. The configurational coordinate model for the Cr <sup>3+</sup> fluorescence in high fields.....	61
2.3.3. Other contributions to temperature dependence at low temperatures.....	62
2.4. Discussion.....	65

2.5.	Impact on subsequent experimental work . . . . .	68
3.	Phase-Locked Detection of Fluorescence Lifetime . . . . .	69
3.0.	Abstract . . . . .	69
3.1.	Introduction . . . . .	70
3.2.	From lock-in to phase-locked detection . . . . .	71
3.3.	PLD with analog modulation of excitation source and single reference signal (PLD-AMSR) . . . . .	74
3.4.	PLD with pulse modulation and single reference signal (PLD-PMSR) . .	76
3.5.	The selection of the phase shift ratio, $\alpha$ . . . . .	79
3.6.	The impact of excitation leakage on single reference PLD schemes. . . . .	84
3.7.	Pulse modulated PLD with two reference signals (PLD-PMTR) . . . . .	86
3.8.	Discussion . . . . .	91
3.9.	Impact of this work . . . . .	92
4.	Cr <sup>3+</sup> Fluorescence Thermometers and Applications of PLD Techniques. . . . .	93
4.0.	Abstract . . . . .	93
4.1.	Introduction . . . . .	94
4.2.	Optical arrangement of fluorescence lifetime thermometers. . . . .	95
4.3.	Ruby based thermometer using PLD-PMSR technique with potential range 20 to 600°C . . . . .	100
4.3.1.	Experimental setup. . . . .	100
4.3.2.	Development of the high-temperature fibre probe. . . . .	103
4.3.2.1.	Characteristics of the metal-coated fibres used . . . . .	103
4.3.2.2.	Probe fabrication . . . . .	104
4.3.3.	The calibration of the thermometer system . . . . .	106
4.3.4.	Further improvement . . . . .	109
4.4.	Alexandrite based thermometer using PLD-PMTR technique with potential range -100 to 700°C . . . . .	114
4.4.1.	Absorption and fluorescence spectra . . . . .	115
4.4.2.	Experimental setup. . . . .	117
4.4.2.1.	Temperature probe . . . . .	117
4.4.2.2.	Excitation source and fluorescence detection. . . . .	118
4.4.2.3.	Signal processing . . . . .	119
4.4.3.	Experimental results. . . . .	120
4.4.4.	Potential for applications down to -100°C. . . . .	123
4.5.	Cr:LiSAF based thermometer for biomedical applications. . . . .	125
4.5.1.	Application background. . . . .	125
4.5.2.	Absorption and emission spectra of Cr:LiSAF . . . . .	126

4.5.3. Experimental set-up for clinical test . . . . .	127
4.5.4. Experimental results . . . . .	129
4.5.5. Further considerations in the application . . . . .	132
4.6. Discussion . . . . .	133
5. Cross Referencing between Blackbody Radiation and Fluorescence Lifetime . .	139
5.0. Abstract . . . . .	139
5.1. Introduction . . . . .	140
5.2. Theoretical background . . . . .	143
5.3. Construction of the temperature probe . . . . .	146
5.4. Configuration of the thermometer . . . . .	147
5.5. Experimental results . . . . .	149
5.6. Discussion . . . . .	152
6. Conclusions and Future Work . . . . .	153
6.1. Assessment of fibre optic thermometers. . . . .	153
6.2. Cross comparison to previous experimental devices . . . . .	155
6.3. Conclusions . . . . .	157
6.4. Discussion and future work . . . . .	160
6.4.1. Cryogenic temperature measurement . . . . .	160
6.4.2. Limitation of the signal processing schemes. . . . .	161
6.4.3. Investigation of other sensing materials . . . . .	162
6.5. Further potential of this work. . . . .	163
References . . . . .	165
Appendix A: A circuit design example of PLD-PMSR scheme . . . . .	174
Appendix B: A list of publications by the author relevant to the thesis: . . . . .	175

## List of Tables

---

---

- Table 1.1: Fibre optic temperature sensor schemes.
- Table 2.1: Empirical values of parameters in the configurational coordinate model of Cr:LiSAF fluorescence.
- Table 2.2: Empirical values of the parameters in appropriate models, fitted to the alexandrite fluorescence lifetime data.
- Table 2.3: Empirical values of the parameters in appropriate models, fitted to the ruby fluorescence lifetime data ranging from 300 to 500 K.
- Table 3.1: Values of  $x_0$  against some typical values of the phase shift ratio  $\alpha$  or  $\beta$  in various PLD schemes.
- Table 4.1: Reproducibilities of the measurements made by the ruby based thermometer system.
- Table 4.2: The observations of the consecutive measurements made in the laboratory.
- Table 4.3: Measurement ranges and resolutions of the discussed thermometer systems.
- Table 6.1: Assessment of early commercialised fibre optic thermometer systems, by Harmer<sup>[83]</sup>.
- Table 6.2: The assessment of various experimental devices developed at the laboratory.

## List of Figures

---

- Figure 1.1: Interferometric film temperature sensor mounted on fibre optic pedestal.
- Figure 1.2: Schematic of a fibre optic thermometer system using the thin-film Fabry Perot temperature sensor shown in Figure 1.1 [33].
- Figure 1.3: Interrelationship between LED spectrum and film reflectance [33].
- Figure 1.4: (a) Basic principle of the temperature sensing system described by Kyuma *et al* [26].; (b) Schematic diagram of the fibre-optic measurement system; (c) Configurational of the fibre-optic temperature sensor.
- Figure 1.5: The fibre temperature probe of Accufiber's blackbody radiation thermometer systems [34].
- Figure 1.6: Excitation and emission spectra of magnesium fluorogermanate activated with tetravalent manganese.
- Figure 1.7: Absorption and emission spectra of  $\text{LiSrAlF}_6: \text{Cr}^{3+}$ .
- Figure 1.8: An example of concentration quenching. In ruby the observed decay time of the fluorescence at 77 K is independent of chromium concentration up to a concentration of around 0.3 weight % of  $\text{Cr}_2\text{O}_3$  in the material [39].
- Figure 1.9: Schematic representation of Luxtron model 1000 [19].
- Figure 1.10: ASEA model 1010 temperature sensor [40].
- Figure 1.11: Two-point time constant measurement technique [28].
- Figure 1.12: Schematic illustration of the integration technique used by Sholes and Small (1980) [18].
- Figure 1.13: Illustration of the balanced integration method.
- Figure 1.14: Illustration of linearised digital curve fit technique.
- Figure 1.15: Phase and modulation measurement of fluorescence lifetime.

- Figure 1.16: Phase-locked detection of fluorescence lifetime using single reference signal. FID: fluorescence inducing and detecting devices;  $\nu_m$ : signal to modulate the output intensity of the excitation light source;  $\nu_f$ : the fluorescence signal; LPF: low-pass electronic filter; VCO: voltage-controlled oscillator. (page 43)
- Figure 2.1: Simplified Tanabe-Sugono diagram. The broken lines represent the approximate energy level positions of the  $\text{Cr}^{3+}$  ion in various host crystals.
- Figure 2.2: Thermal characteristics of  $\text{Cr}^{3+}$  fluorescence in LiSAF. ●●●: data for the fluorescence lifetimes.  $\Delta\Delta\Delta$ : data for the fluorescence intensity.
- Figure 2.3: The single configurational coordinate model for  $\text{Cr}^{3+}$  fluorescence in low field crystals.  $r$ : configurational coordinate.
- Figure 2.4: Temperature dependences of the fluorescence lifetimes of Cr:LiBAF, Cr:LiCAF<sup>[54]</sup>, and Cr:LiSAF.
- Figure 2.5: The 2 level model for  $\text{Cr}^{3+}$  fluorescence in high field crystals.
- Figure 2.6: Temperature dependence of the alexandrite fluorescence. ●●●: the fluorescence lifetime data taken in this work. **Solid line**: the least squares curve of the two-level model [Eq.(2-6)] fitted to the lifetime data over the region 290 - 680 K. **Dashed line**: the least squares curve of the configurational coordinate model [Eq.(2-10)] fitted to the lifetime data over the region 300 - 930 K.  $\Delta\Delta\Delta$ : the lifetime data from Walling et al [51]. \* \* \*: data for the fluorescence intensity at the broadband vibronic emission ( $>\sim 690$  nm) induced by a 662 nm diode laser.
- Figure 2.7: Temperature dependence of the ruby fluorescence. \* \* \*: the fluorescence lifetime data where a He-Ne laser (633nm) is used as the excitation source. **Solid line**: the least squares curve of the two-level model [Eq.(2-6)] fitted to the lifetime data over the region 300 - 475 K. **Dashed line**: the least squares curve of the configurational coordinate model [Eq.(2-10)] fitted to the lifetime data over the region 300 - 800 K.  $\Delta\Delta\Delta$ : data for the fluorescence intensity at the broadband vibronic emission ( $>\sim 695$  nm) induced by the He-Ne laser. o o o: the lifetime data from Nelson *et al* [60].
- Figure 2.8: The single configurational coordinate model for  $\text{Cr}^{3+}$  fluorescence in high field crystals.  $r$ : the configurational coordinate.

- Figure 2.9: Temperature dependence of ruby fluorescence lifetime at low temperatures.
- Figure 2.10: Temperature dependences of Cr<sup>3+</sup> fluorescence lifetime in various host materials. Materials with low strength of crystal field: **1.** LiSAF; **2.** LiBAF<sup>[54]</sup>; **3.** LiCAF<sup>[54]</sup>. Materials with high strength of crystal field: **4.** alexandrite<sup>[51, 59]</sup>; **5.** ruby (data from ~20 to 300 K obtained from Nelson *et al*<sup>[60]</sup>, those from 300 K and beyond by the author); **6.** emerald<sup>[52]</sup>.
- Figure 3.1: A two-phase lock-in system. FID: the fluorescence inducing and detecting devices. Mixer: switch type, double balanced demodulator. LPF: low pass filter. PSD: phase sensitive detector.
- Figure 3.2:  $z$  v.s.  $\phi$  where  $z$  is normalised to its minimum.
- Figure 3.3: A PLD-AMSR system. VCO: Voltage Controlled Oscillator.
- Figure 3.4: A PLD-PMSR system. (Components as Figure 3.1)
- Figure 3.5: Waveforms of signals designated in Figure 3.4.
- Figure 3.6:  $y$  v.s.  $x$  for PLD-PMSR.
- Figure 3.7:  $x_0$  v.s.  $\alpha$ . **Solid line:** for PLD-PMSR; **dashed line:** for PLD-AMSR.
- Figure 3.8:  $s_y$  &  $s_x$  v.s.  $\alpha$ . **Solid lines:** for PLD-PMSR; **dashed lines:** for PLD-AMSR.
- Figure 3.9: The impact of the excitation leakage (in the case of AMSR with  $\alpha=3/8$ ).
- Figure 3.10: A PLD-PMTR system. (Components as Figure 3.1)
- Figure 3.11: Waveforms of signals designated in Figure 3.10.
- Figure 3.12:  $x_0$  vs.  $\beta$  for PMTR in solid line;  $x_0$  v.s.  $\alpha$  for PMSR in dashed line.
- Figure 3.13: **Curve 1:**  $s_x$  vs.  $\beta$  for PMTR; **curve 2:**  $s_y$  vs.  $\beta$  for PMTR; **curve 3:**  $s_y$  vs.  $\alpha$  for AMSR; **curve 4:**  $s_y$  vs.  $\alpha$  for PMSR.
- Figure 3.14: The configuration of the pre-mixer for single sided PLD-PMTR.
- Figure 3.15: Waveforms of signals designated in Figure 3.14.

- Figure 4.1: Schematics of the optical arrangement and temperature probes for the  $\text{Cr}^{3+}$  fluorescence lifetime based fibre optic thermometers. **S**: the fluorescence material used as sensing element;  $\nu_m$ : signal to modulate the output intensity of the excitation light source;  $\nu_f$ : the detected fluorescence response from the sensing element; **LED**: light emitting diode; **F<sub>1</sub>**: short-pass optical filter; **F<sub>2</sub>**: band-pass or long-pass optical filter; **LD**: laser diode.
- Figure 4.2: Remote measurement probes <sup>[68]</sup>.
- Figure 4.3: Temperature probes for contact measurement. **(a)**. The reflection-type probe; **(b)**. the transmission-type probe.
- Figure 4.4: The ruby fluorescence lifetime based fibre optic thermometer system. **F<sub>1</sub>**: short-pass optical filter; **F<sub>2</sub>**: *R*-line band-pass optical filter.
- Figure 4.5: The absorption spectrum of ruby. From Evtuhov and Neeland <sup>[69]</sup>.
- Figure 4.6: The emission spectrum of ruby. From Fonger and Struck <sup>[52]</sup>.
- Figure 4.7: Temporal profiles of excitation light and fluorescence emission at room temperature. **Upper trace**: modulation signal applied to the LED with a frequency of  $\sim 40\text{Hz}$ . **Lower trace**: fluorescence response signal output by the photodetector shown in Figure 4.4.
- Figure 4.8: Schematic of the fibre-optic probe used with the ruby fluorescence lifetime based thermometer described in this thesis work.
- Figure 4.9: Characteristic calibration curve for the ruby fluorescence based thermometer in the region from room temperature to  $\sim 550^\circ\text{C}$ .
- Figure 4.10: The ruby fluorescence intensity recorded in the experiment.
- Figure 4.11: The calculated temperature measurement deviation of the ruby fluorescence thermometer system.
- Figure 4.12: Thermal characteristics of ruby fluorescence observed by the improved system.  $\Delta \Delta \Delta$ : data for the observed lifetime. **Solid line**: the least squares curve fitted to the lifetime data using the configurational coordinate model for  $\text{Cr}^{3+}$  fluorescence in a high field crystal, presented in Chapter 2. **Dashed line**: the relative temperature sensitivity of the observed lifetime. **• • •**: the observed fluorescence emission intensity.

- Figure 4.13: The calculated temperature measurement deviation of the improved ruby fluorescence thermometer system, in **solid line**. **Dashed line**: that of the previous system presented in Figure 4.11.
- Figure 4.14: Absorption spectrum of alexandrite at room temperature.
- Figure 4.15: Fluorescence spectrum of alexandrite at room temperature.  $\lambda_{ex}$ : excitation wavelength. From Powell *et al*<sup>[76]</sup>.
- Figure 4.16: Schematic of the optoelectronic setup of the alexandrite fluorescence based thermometer. **LD**: laser diode.
- Figure 4.17: Schematic of the optical fibre probe.
- Figure 4.18: **(a)** Ideal temporal profiles of excitation light and fluorescence emission. **Upper trace**: modulation signal applied to the laser diode. **Lower trace**: fluorescence emission signal. **(b)** Actual temporal profiles of excitation light and fluorescence emission received with leakage of excitation light. **Upper trace**: the intensity of the square wave modulated light output of the laser diode. **Lower trace**: fluorescence emission signal received showing leakage of excitation light.
- Figure 4.19: Observed alexandrite fluorescence lifetime vs.. temperature. o o o: data taken in the case of using 670 nm laser diode. x x x: data taken in the case of using 655 nm laser diode. ----: relative temperature sensitivity of the observed lifetime.
- Figure 4.20: Alexandrite fluorescence intensity vs.. temperature. • • •: data for fluorescence emission at low energy broadband ( $\lambda > 695\text{nm}$ ) induced by 670nm laser diode.
- Figure 4.21: Calculated temperature measurement deviation of the alexandrite based thermometer system, depicted as a function temperature.
- Figure 4.22: Polarised absorption and emission spectra of  $\text{LiSrAlF}_6:\text{Cr}^{3+}$  from Payne *et al*<sup>[37]</sup>.
- Figure 4.23: Schematic of the Cr:LiSAF fluorescence based thermometer.
- Figure 4.24: The configuration of the RF applicator.
- Figure 4.25: The observed lifetime of the Cr:LiSAF fluorescence decay and its temperature sensitivity.  $\Delta\Delta\Delta$ : data for the observed lifetime. **Solid line**:

curve fitting to the data. **Dashed line**: the relative temperature sensitivity of the observed lifetime.

Figure 4.26: The Cr:LiSAF fluorescence intensity recorded in this system. ●●●: data for the fluorescence intensity. **Dashed line**: curve fitting to the data.

Figure 4.27: Calculated temperature measurement deviation of the Cr:LiSAF based thermometer system. The part beyond 100 °C is extrapolated using the configurational coordinate model for Cr<sup>3+</sup> fluorescence in low strength fields.

Figure 4.28: Relative temperature sensitivities of the observed fluorescence lifetimes of various materials. 1: for ruby observed by the system using a green LED as excitation source and characterised with long time-constant; 1': for ruby observed using He-Ne laser excitation; 2: for alexandrite; 3: for Cr:LiSAF.

Figure 4.29: Error vs.. temperature curves. 1: for the ruby based system using green LED excitation; 1': for the improved ruby based system using He-Ne laser excitation; 2: for the alexandrite based system; 3: for the Cr:LiSAF based system.

Figure 5.1: Temperature dependences of Nd:YAG fluorescence. ○ ○ ○: data for the fluorescence lifetime; **solid line**: curve fitting to the fluorescence lifetime data; **dashed line**: curve fitting to the data for fluorescence intensity at 1064nm.

Figure 5.2: Fluorescence lifetime calibration curve for ScPO<sub>4</sub>:Eu<sup>3+</sup> from Bugos *et al*<sup>[79]</sup>.

Figure 5.3: Schematic of the optical fibre sensor probe.

Figure 5.4: Schematic of the opto-electronic sensor scheme. (S/H) sample and hold devices.

Figure 5.5 Time dependence of the signals used in the processing scheme. ( $v_m$  vs  $t$ ) input light modulation signal; ( $v_f$  vs  $t$ ) total light signal detected by the photodetector; ( $W(T)$ ) the radiation background signal; ( $v_{f1}$  vs  $t$ ,  $v_{f2}$  vs  $t$ ) outputs of the first stage of S/H devices.

Figure 5.6: Calibration graph of the fluorescence lifetime and blackbody radiation vs temperature. ● ● ●: data for the Nd:YAG fluorescence lifetime; **solid line**: curve fitted to the fluorescence lifetime data. ○ ○ ○: data for

thermally generated radiation normalised to the value at 850 °C; **dashed line**: the corresponding theoretical curve of blackbody radiation.

Figure 6.1: Temperature dependence of GSGG:Cr<sup>3+</sup> fluorescence lifetime. ○ ○ ○: data from Armagan and Bartolo [86]. ● ● ●: data from Healy et al [87].

Figure 6.2: Temperature dependence of emerald fluorescence lifetime from Fonger and Struck [52].

Figure 6.3: Temperature dependence of the Cr<sup>3+</sup> fluorescence lifetime calculated assuming different values of  $p$  by Henderson *et al* [90].

Figure 6.4: Pressure dependence of the lifetime of alexandrite R-line fluorescence in hydrostatic environment from Jia *et al* [96].

# Acknowledgements

The work reported in this thesis was conducted under the supervision of Professor Kenneth T. V. Grattan. I wish to express my sincere appreciation to him for his excellent supervision of this work and, for the inspiration and encouragement from him in the course of this study. I am grateful for countless helps that he have offered to me, which ranging from the arrangement of my participation of academic conferences and financial support for my study, to the reviewing of all my academic publications during this period of study.

I can hardly express my gratitude to Dr. Andrew W. Palmer for his precious comment and stimulating guidance in the entire course of this study. His help and encouragement have never ceased throughout different phases of my studies.

I am grateful for the financial support provided by the City University and the Science and Engineering Research Council. The financial support from the State Educational Commission of China at the early stage of my studies is also sincerely acknowledged.

Debts of gratitude are also owed to all the technical staff in the Department, especially Mr. Roger Valsler and Mr. David Jackson. The help offered by Mr. Roger Valsler and his expertise in the engineering of optical fibre accessories were essential to the conducting of the work reported. The assistance from Mr. David Jackson resulted in the production of a prototype thermometer system.

I would also like to express my gratitudes to all the research staff in the Optical Instrumentation Group, all of whom have been very kind in offering their time and expertise. Thanks are also owed to Mr. Z. Mouaziz and all of my colleagues in the optical instrumentation laboratory for their help and the friendly, joyful atmosphere surrounding me in the course of this work. Finally, my deepest gratitude is devoted to my parents and my wife, Peiqian. It is only with their love and support that my research is made possible.

# Declaration

The author hereby grant powers of discretion to the City University Librarian to allow the thesis to be copied in whole or in part without further reference to the author. This permission covers only single copies made for study purposes, subject to normal conditions of acknowledgement.

# Abstract

Starting with a review of the development of fibre optic temperature sensing techniques, this thesis is comprised of the author's work on the fibre optic fluorescence thermometry, a prominent branch of fibre optic thermometry. First, the temperature dependences of fluorescence in  $\text{Cr}^{3+}$  doped materials, a large family of promising temperature sensing materials are examined, which lay the theoretical basis of the fluorescence thermometry discussed herein. Based on the Tanabe-Sugano diagram, such temperature dependences are characterised with the crystal field strengths of the host materials and two single configurational coordinate models are proposed for the temperature dependences in materials with high and low crystal field strengths respectively. These models have successfully explained the great diversity in the temperature dependences of the  $\text{Cr}^{3+}$  fluorescence lifetimes, by their close fits to the experimental data of various corresponding materials.

Then, the work contributing to the instrumentation aspects of the fluorescence thermometry is discussed. Evolving from the lock-in amplifier technique, a category of novel, effective and versatile instrumentation approaches: the *phase-locked detection of fluorescence lifetimes* (PLD), is presented. The operating principles of these new signal processing approaches are described with theoretical analysis and graphic illustrations. The theoretical basis of the electronic design is provided.

After the descriptions of the PLD techniques, examples of their applications in various successful  $\text{Cr}^{3+}$  fluorescence based fibre optic thermometer schemes are presented, which are developed in the course of this study. These demonstrate that the PLD schemes can be operated over a wide consecutive measurement range of fluorescence lifetime with a high measurement resolution, and are particularly useful for temperature sensor applications using long lifetime ( $> 1 \mu\text{s}$ ) fluorescent media. Some considerations in relation to specific applications, e.g. in high temperature sensing or in medical RF hyperthermia treatment, are discussed including the fabrications of temperature fibre probes for various specified applications. The applications of the two single configurational coordinate models proposed in this work are also discussed showing their good potentials for the calibration of the  $\text{Cr}^{3+}$  fluorescence based thermometers.

Finally, the feasibility of the incorporation of the fluorescence thermometry with the long-established radiation thermometry, to extending the measurement range of a fibre optic temperature sensor is illustrated, by a fibre optic sensor scheme based the cross referencing between the fluorescence lifetime of Nd:YAG and the blackbody radiation at a single wavelength, 1064 nm. To conclude this thesis, a cross comparison to previous experimental work is made with a discussion of the future work, and the further potentials of this work are also investigated.

# Symbols and Abbreviations

${}^4A_2$	Ground electronic state of transition metal ions in crystal fields
$C_1, C_2$	Radiation constants, $C_1 = 2\pi hc^2$ and $C_2 = hc/k$
${}^\circ\text{C}$	Degree Celsius
$\text{Cr}^{3+}$	Trivalent Chromium Ion
$Dq/B$	Normalised octahedral crystal-field strength
$E, \Delta E$	Energy and energy splitting between two different energy states
${}^2E$	One of the low-lying electronic state of transition metal ions in crystal fields, from which the sharp <i>R</i> -line emissions initiate.
$E/B$	Normalised energy of the low-lying excited energy states
FID	Fluorescence inducing and detecting device
G	giga, $10^9$
$f$	Frequency of a repetitive signal
$h$	Planck constant, $6.625 \times 10^{-34}$ J s
$h\nu$	Quantum energy
$I$	Luminous intensity
k	kilo, $10^3$
$k$	Boltzmann constant, $1.38 \times 10^{-23}$ J K <sup>-1</sup>
K	Degree Kelvin
LD	Laser diode
LED	Light emitting diode
LPF	Low-pass electrical filter
m	meter, or milli, $10^{-3}$
M	mega, $10^6$

n	nano, $10^{-9}$
$n$	Population of an energy state
$\text{Nd}^{3+}$	Trivalent Neodymium Ion
<i>opt</i>	Optimum
PLD	Phase-locked detection of fluorescence lifetime
PLD-AMSR	Phase-locked detection with analog modulation of excitation source and single reference signal
PLD-PMSR	Phase-locked detection with pulse modulation of excitation source and single reference signal
PLD-PMTR	Phase-locked detection with pulse modulation of excitation source and two reference signals
PSD	Phase sensitive detector
RF	Radio frequency
<i>R</i> -line, $R_1$ , $R_2$	Emission resulting from the non-phonon ${}^2E \rightarrow {}^4T_2$ transitions
$s$ , $s$	Sensitivity, or second
$S$	Area
$t$	Time
$T$	Temperature, or time
$\tilde{T}$	Period of a repetitive signal
${}^4T_2$	One of the low-lying electronic state of transition metal ions in crystal fields, which is responsible for the low energy optical absorption band
$V$	The amplitude of a voltage signal
VCO	Voltage-controlled oscillator
$W$	Power
$x$ , $x_0$	The ratio of the period of the repetitive signal to the measured fluorescence lifetime in a phase-locked detection (PLD) system

$y$	The output of a phase sensitive detector
$\otimes$	Mixer, or switch type, double balanced demodulator in a phase sensitive detector
$\alpha, \beta$	Ratios of transition rates, or the phase shift ratios in a phase-locked detection (PLD) system
$\delta$	Sight path factor
$\varepsilon$	The emissivity of a surface
$\eta$	The ratio of excitation leakage amplitude to that of the fluorescence response
$\lambda, \Delta\lambda$	Wavelength and variance of wavelength
$\mu$	Micro-, $10^{-6}$
$\pi$	pi = 3.142
$\sigma$	Error, or deviation
$\tau$	Fluorescence lifetime, or the time-constant of a exponential signal
$v_f$	Fluorescence signal
$v_m$	Intensity modulation signal to the excitation source
$v_r$	Reference signal
$v_l$	Excitation light leakage
$v_{f+l}$	Fluorescence response signal contaminated by excitation light leakage
$\varphi$	Phase angle
$\omega$	Angular frequency

# Fibre Optic Fluorescence Thermometry: Introduction

---

### 1.1. Introduction

Temperature is one of the four or five most important parameters in industrial process control. The particular importance of the measurement of temperature is found equally in most spheres of scientific activity and daily life. Almost all chemical processes and reactions are temperature-dependent. Not infrequently in chemical plant, temperature is the only indication of the progress of the process. Where the temperature is critical to the reaction, a considerable loss of product or efficiency may result from incorrect temperatures. In some cases, loss of control of temperature can result in catastrophic plant failure with the attendant damage and possible loss of life.

There are many other areas of industry where temperature measurement is essential. Such applications include steam raising and electricity generation, plastics and glass manufacture and moulding, manufacturing processes in metallurgical industries, milk and dairy products and many other areas of the food industries. Further, in biomedical areas, the taking and the monitoring of patients' temperatures provide the basic diagnostic criterion, and it is essential during some hyperthermia treatments, for the safety of patients.

The importance of temperature measurement can even be seen simplistically by consideration of the financial aspects of the sensors and devices used world-wide. Estimates on the world-wide sales of temperature sensors run to several hundred million

pounds per year <sup>[1]</sup>, a figure that could be increased several times when the associated controllers, indicators, and other aspects of the measurement system are added.

Although a wide range of existing instruments is available for use either in industry or in laboratories, or under special industrial conditions, the innovation and the research and development activities have never ceased, due to the ever extending areas of use of thermometers in the industrial, the research and development and biological environments. These environments can present many significant difficulties for the determination of temperature. The region to be measured may be moving, extremely hostile, in a position where access is extremely difficult, or where the physical contacting of a sensing probe may even be impossible, or where the presence of interference from other electromagnetic noise excludes the use of electronic thermometers. Examples of these situations are the measurement of the temperature of a rotating blade of a turbine-engine, the monitoring of winding temperatures in electrical transformers, and the temperature monitoring during clinical RF heat treatment, etc. To seek alternative means of temperature sensing, one of the most active research and development areas is in thermometry based on the use of fibre-optics.

## **1.2. Fibre optic temperature measurement**

### **1.2.1. Historical overview**

It is already over two decades now since the first concepts of the use of fibre optic techniques for sensor purposes were discussed. The initial drive for the development of fibre optic sensors came from their potential use in military and aerospace applications where the cost factors of the introduction of new technology were less rigid and the working environment more hostile than is experienced with other areas of application.

In many cases fibre optic techniques simply make more convenient the use of "open air path" optical approaches, through the more convenient channelling of the light to and from the region of measurement <sup>[2]</sup>. Thus, for example, radiation pyrometry can easily be adapted to fibre optic measurement <sup>[3]</sup>. However, fibre optic sensors in their own right have been produced in recent years and much research effort has been directed toward the

development of this technology. As a result, a considerable body of publications has appeared and specifications for a number of commercial products have been advertised by major manufacturers.

In addition, fibre optics for communication purposes are now well established [4]. The U.S., Japan, and most European countries have extensive programmes of fibre optic cabling for the main trunk networks of their telecommunications systems. Many computer data links rely on fibre optics, and there is considerable discussion of the use of fibre optics as communications channels for data into the home. By this means the superior data handling capacity of fibre optics over conventional cabling may be used. All these have resulted in a considerable decrease in the price of fibre optics and their associated optoelectronic devices, i.e., emitters and detectors. With the increase in sophistication of electronic signal processing techniques, there is no reason why inexpensive fibre optic sensors relying upon sophisticated electronic signal processing cannot be commercialised at reasonable costs.

It is, however, disappointing to note that in spite of the wealth of information that has been published in the literature on fibre optic sensors, as yet the product range commercially available is small and few manufacturers are using fibre optic devices for actual industrial or process control. As a result, the industrial or medical sphere has not experienced the development of fibre optic sensors that was predicted up to 10 years ago in many of the earlier, somewhat over optimistic, papers of the field [5]. Nonetheless, steady progress is being made and the advantages of the use of fibre optic sensors, as discussed later, are evident. Contrasts and comparisons with the slow development of the use of the laser outside the laboratory can be made, as this technology has taken about 25 years to mature. Many commercial fibre optic products only now have evolved to product stage, following initial ideas and early research work of 10 years previously [6].

### **1.2.2. Advantages of fibre optic temperature measurement**

The primary reason for interest in fibre optic sensors in most cases stems from the fundamental differences between an optical fibre and a metal wire. These differences give fibre optic sensors the following advantageous characteristics:

### ***Electrical, Magnetic and Electromagnetic Immunity:***

This is the dominant attribute of the fibre optic sensor. The materials in the probe are typically good electrical insulators. Since they do not conduct electricity, the probes cannot (in principle) introduce electrical shorting paths or electrical safety problems. Likewise, since they do not absorb significant amounts of electromagnetic radiation fields or be heated by such fields with the resultant introduction of thermal artifacts into the readings. Last, but not least, stray fields cannot induce electrical noise in the fibres, so the probes exhibit a very high level of electromagnetic immunity (EMI) when used in electrically or magnetically hostile environments.

### ***Small sensor size:***

Since the typical sensor does not have to be any larger in diameter than the fibre itself, the sensor can, in principle, be extremely small. This allows use in applications such as in medicine or in microelectronics where size is critical. Further, since small size means small thermal mass, the fibre optic sensors typically exhibit a commensurate very rapid thermal response.

### ***Safety:***

The safety issue may be the main reason for the use of fibre optic sensors in some particular areas of application. Most fibre optic sensors require no electrical power at the sensor end of the system. They generate their own optical signal or they are "powered" remotely by radiation from a light source located within the instrument. Therefore they introduce no danger of electrical sparking in hazardous environments. There is reason to believe that at the normal levels of optical power coupled into fibre optics, i.e., levels of up to several hundred milliwatts of optical power, there is almost no hazard with any accidental fracture of cable and possible focusing of the optical radiation by the lensing effects of the broken end. Particularly in chemical industry, where highly explosive gases or gas mixtures may be used, this is an important consideration, but on the whole in normal use, fibre optic sensing systems can be considered intrinsically safe. A considerable discussion of this aspect has been made in reports commissioned by the U.K. Optical Sensors Collaborative Association by Tortishell <sup>[7]</sup> and others.

### ***Capability of remote measurements:***

The small size of the fibre and its electrical, chemical and thermal inertness allow long-term location of the sensor deep inside complex equipment and thereby provide access to difficult to address locations where temperature may be of interest. Beyond this, however, certain of the optical techniques allow non-contact or remote sensing of temperature. For example, the sensor may be located at some distance from the fibre tip. This is most easily accomplished with the fluorescence-based fibre optic techniques and with infrared radiometry. The point of interest may in fact be located on a moving or rotating part or behind a transparent window as in a pressure or vacuum chamber, and yet the radiation can be collected and analysed to gain the remote temperature information.

### ***Other advantages:***

Beyond these generic advantages, certain of the optical techniques exhibit an unusually wide range of operation with precision good enough to meet requirement. At the same time these techniques provide simplicity of calibration (or, as in the case of the fluorescence lifetime techniques, the absence of the need for calibration for individual probes).

## **1.2.3. Sensor devices**

There is perhaps most diversity in the techniques that are used for optically-based temperature measurement, as a result of the fact that, there are essentially as many ways of making a temperature measurement optically as there are temperature dependent optical properties. As the sensor can either be formed from the fibre itself (termed "intrinsically") or from a material or structure attached to the end of the fibre (termed "extrinsically"), the number of possible fibre optic temperature sensor devices is quite large. Indeed, there has been something of an explosion of device proposals seen in the literature. Extensive reviews have been given by Grattan [2, 8] and Wickersheim [9] on the proposed sensor schemes. Based on the classification methods used by these authors, some typical sensor schemes, among those which have been considered seriously to date, are listed in Table 1.1. according to the temperature dependent properties used.

In addition, a variety of simpler optomechanical schemes, such as those employing the changes in the intensity of reflected light, due to the thermally-induced displacement

**Table 1.1:** Fibre optic temperature sensor schemes.

Temperature dependent property used	Sensor material or structure	Examples of work by:
Optical reflection	Liquid crystal; Thermochromic material	Rozzell <i>et al</i> [13]; Brenci [14]
Optical scattering	Fibre itself	Dakin <i>et al</i> [15, 16]
Birefringence	Lithium niobate	Knox <i>et al</i> [17]
Fluorescence	Gallium arsenide; various phosphors	Sholes and Small [18]; Wickersheim and Alves [19]; Bosselman <i>et al</i> [20]; Grattan and Palmer [21]
Optical interference	Fabry Perot etalon	Saaski <i>et al</i> [22, 23]; Beheim [24]
Optical absorption	Gallium arsenide crystal; GaAs	Christensen [25]; Kyuma <i>et al</i> [26]
Thermally-generated radiation	Blackbody cavity	Dakin and Kahn [27]

of a reflecting surface, or grating displacement which has been proposed for pressure measurement [10], have been considered [2]. At the other extreme, highly sophisticated interferometric systems, such as the dual wavelength interferometric device which significantly extend the useful range of a normal interferometric system [2, 11], and those using white light interferometry which would be free of "switch-on" re-calibration [12], have been suggested.

First of all, among the wide choices of potentially usable sensor schemes listed above, the right selection for development would rely strongly on matching to the intended application. For industrial applications, system cost, range, ease of calibration, stability and durability would be the primary considerations; for bio-medical purposes, probe size, sterilisability, biocompatibility and precision as well as disposability (cost) would be important. If the application requires multi-point sensing, distributed sensing schemes such as those using optical scattering properties, may be the better answer; whereas if the temperatures are very high, as in an aircraft engine, the radiometric approach might be the best.

At a more basic level, there are some fundamental considerations as well. Sensor fabrication should, as far as possible, be simple. The performance of the instrument should not depend on which individual sensor is being used. Substitution of sensors should be quick and easy. Ideally, the system should not require calibration before use or after sensor replacement. If a calibration is required, it should be very simple to perform, preferably by the user. The sensor materials or structure, should also be very stable over time with repeated thermal excursions.

Most importantly, the performance of the system has to be insensitive to optical signal changes such as those caused by fibre bending, light source degradation, variable connector losses, or changes in fibre transmission over time. Many of the early sensor designs were based on detection of a simple change of light intensity with temperature. In these systems it was impossible to separate the effects of thermally induced changes in intensity from other non-thermal sources of signal change such as those just mentioned. Therefore, in the more successful systems available today, some type of intensity ratioing is employed or a temperature-sensitive parameter other than intensity (e.g. fluorescence lifetime) is detected.

To meet the requirements of the above list, a range of technologies are now becoming available. For point sensing in the low to moderate temperature range (e.g. -200 to +700 °C), the dominant techniques by far are based on the measurement of the fluorescence properties of selected sensor materials. This approach, particularly in those systems in which fluorescence lifetimes are measured, such as Luxtron model 750 [28] and those developed at City University [29 - 31], avoids the problem of non-thermal optical intensity variations. In addition, since the fluorescence lifetime is intrinsic to the sensor material, such a system is inherently self-calibrating. The fluorescence technique also leads to very simple sensor fabrication and allows the use of a single fibre, since exciting and emitted radiation are of different wavelength and therefore are easily separated by filters. If the sensor materials are properly selected, the fluorescence technique also yields a wide range of operation with great stability over time and with temperature exposure.

Among the sensors of the reflection type as classified in Table 1.1, are those in which the sensor material is a liquid crystal film. Such sensors were among the first fibre optic

temperature sensors to be developed. Rozzell *et al* <sup>[13]</sup> developed such a sensor for use in medical and biomedical applications. Later, Windhorn and Cain <sup>[32]</sup> have developed a more elaborate sensor in which the plane of polarisation is rotated by a sensor formed from a mixture of liquid crystals. A more recent device in this category is that developed by Brenci <sup>[14]</sup>. In biomedical applications, as pointed out by Grattan <sup>[2]</sup>, the potential problem of such a system exists in that the thermochromic material may spill and could be a health hazard to the patient. The limitations of liquid crystals also lie in their narrow range of operation and their inherent chemical instability. The latter problem leads to both calibration instabilities and unacceptable hysteresis and has prevented such systems from becoming commercially successful <sup>[9]</sup>.

Apart from that utilising fluorescence, two other types of point sensors are also available commercially. In one of them, the sensor is a small Fabry-Perot etalon made from a thin film of single-crystal silicon, on the order of 1 micrometer in thickness and sandwiched between two layers of an appropriate transparent material by micro electronic fabrication techniques, as shown in Figure 1.1 <sup>[33]</sup>. While the optical properties are not intrinsic to the materials alone, since structural variations also enter in, the sensors are simple to fabricate. Once a sensor is calibrated, its individual calibration is communicated to the instrument via an electrical interface. Two wavelength ratioing, using the extreme wavelengths of the emission from the LED light source, as illustrated in Figure 1.2 is used

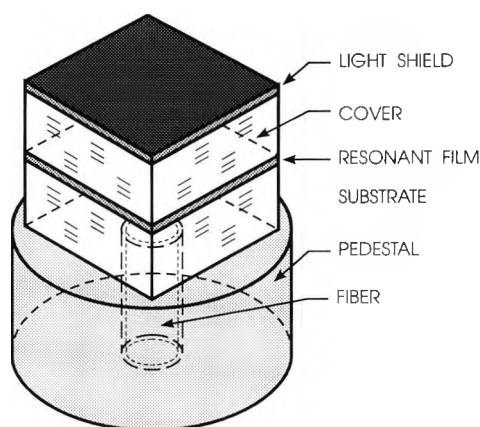


**Figure 1.1:** Interferometric film temperature sensor mounted on fibre optic pedestal.

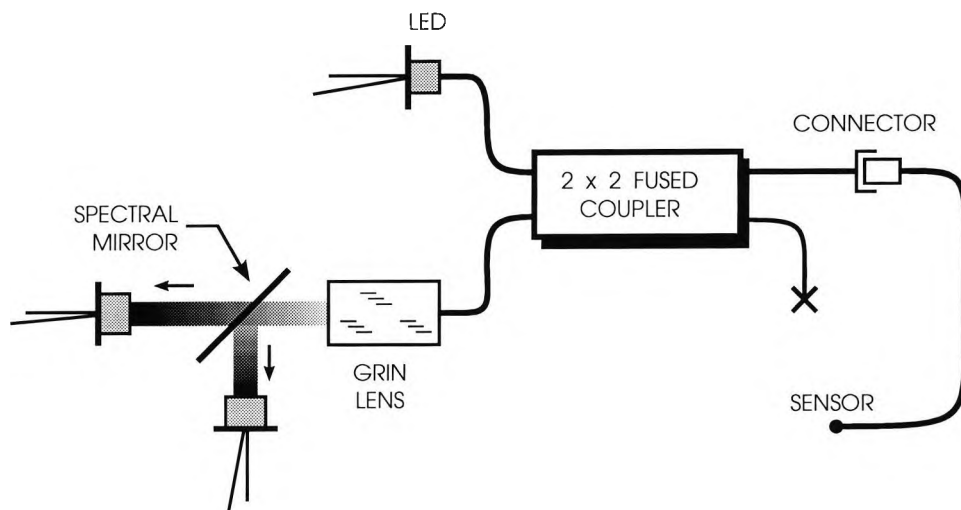


**Figure 1.2:** Schematic of a fibre optic thermometer system using the thin-film Fabry

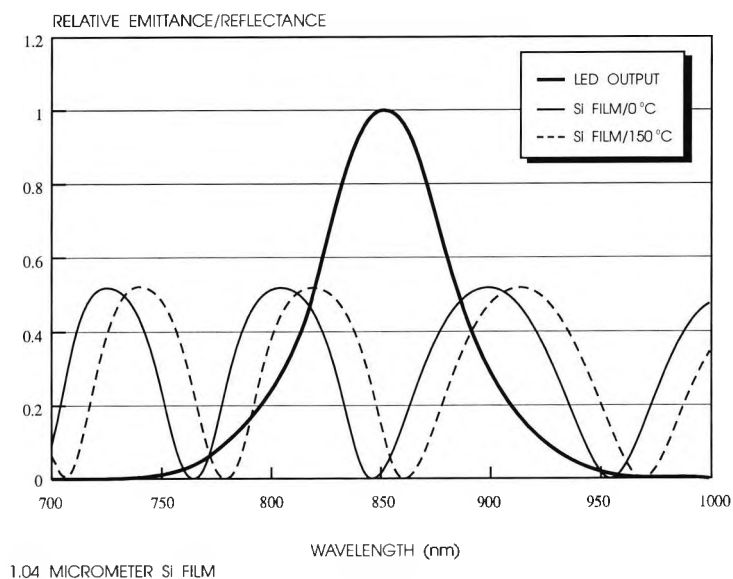


**Figure 1.3:** Interrelationship between LED spectrum and film reflectance [33].

to minimise the non-thermal intensity variation problems mentioned above. The interrelationship between the LED spectrum and the film reflectance is shown in Figure 1.3, at 0 and 150°C.

An example of the second type of instrument is that developed by Christensen [25]. In this system, the sensor is an absorbing gallium arsenide crystal fabricated as part of a compact structure which returns the transmitted signal back to the instrument through a parallel fibre using two 90° reflections [25]. The intensity changes in the sensor are

produced by the wavelength shift of the optical absorption edge of gallium arsenide with temperature. Although the version of this system which was originally introduced for use in medical hyperthermia operates at only a single wavelength, two wavelength ratioing can again be used to make the system less sensitive to non-thermal intensity changes. This system has been licensed to Clini-Therm, a manufacturer of hyperthermia therapy equipment.

An experimental device of the above type is also developed by Kyuma *et al* [26] in Mitsubishi Electric Corporation, Japan. Their system, depicted in Figure 1.4, uses either polycrystalline CdTe, or gallium arsenide as that used by Christensen [25]. As shown in Figure 1.4(c), the configuration of the sensor probe is different from that of Christensen's. It could simplify the manufacturing of probes, however, with added difficulty in the planting of probe in applications. The performance of the system is examined over the region from  $-10^{\circ}\text{C}$  to  $300^{\circ}\text{C}$ , and it is found that gallium arsenide sensor is more sensitive than the CdTe sensor at lower temperatures ( $<150^{\circ}\text{C}$ ). It was claimed that an accuracy of  $\pm 1^{\circ}\text{C}$  is achievable over the above temperature region.

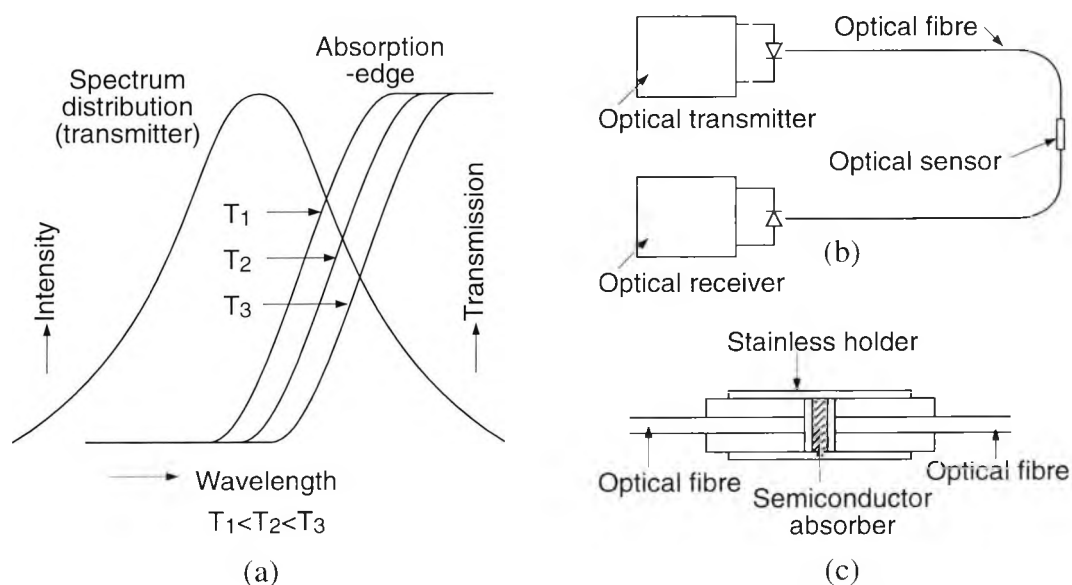


**Figure 1.4:** (a) Basic principle of the temperature sensing system described by Kyuma *et al* [26]; (b) Schematic diagram of the fibre-optic measurement system; (c) Configurational of the fibre-optic temperature sensor.

For use at moderate to very high temperatures (above 300°C), the fibre optic equivalent of the infrared radiometer is now available, e.g. Accufiber model 100 [34]. This is the only type of fibre optic system which can cover the range up to 2000 °C but is limited at lower temperature region. The probe is typically made of sapphire, as shown in Figure 1.5. Either a blackbody cavity is constructed at the tip of the sapphire fibre by means of an opaque coating or the sapphire fibre is simply used as a light pipe to collect and analyse thermal radiation from a particular portion of a hot source of interest. The thermally generated radiation is transmitted to the far end of the sapphire probe where it is coupled into a conventional optical fibre for transmission to the instrument. The conventional fibre does not transmit a sufficient amount of intermediate infrared radiation to allow measurements down to a few hundred degrees Celsius.

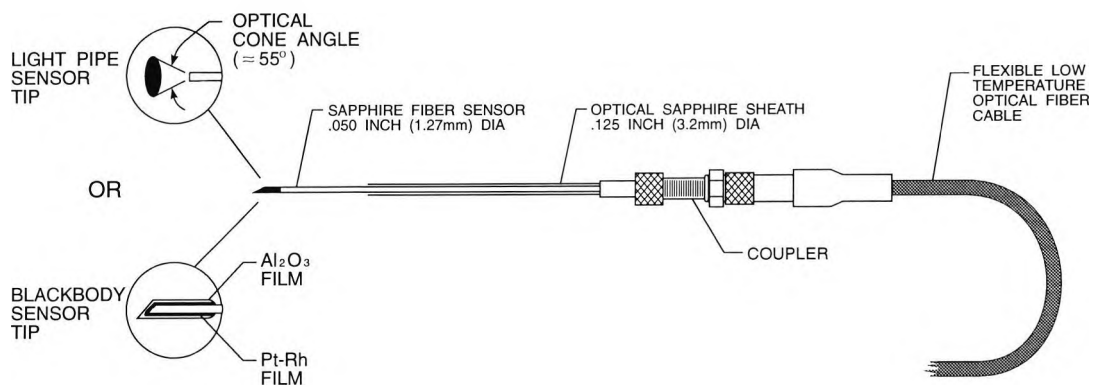


**Figure 1.5:** The fibre temperature probe of Accufiber’s blackbody radiation thermometer systems [34].

There are also a variety of types of distributed temperature sensors, most of which utilise some form of time domain reflectometry. The system which is the most developed commercially [15, 16] at this time uses laser-induced Raman scattering to produce two return (Stokes and anti-Stokes) optical signals from the fibre, the time of arrival of which indicates the location within the fibre of the region whose temperature is being sensed with relative intensity of the two back-scattered wavelengths carrying the temperature information. A single fibre loop some 2 kilometres in length can provide as many as 100 well separated sensing points. The measuring instrument tends to be quite sophisticated and therefore expensive, but the cost per sensing point given a large enough array of sensors,

can in fact be reasonable. Processing time is (presently) quite slow and the sensors are not small, typically consisting of a meter or more of coiled fibre. However, the potential of this technique for extended area measurement seems quite promising, presuming the right applications can be identified.

### 1.3. Fluorescence-based fibre optic thermometry

#### 1.3.1. Photoluminescence

Photoluminescence is the phenomenon of light emission, in excess of thermal radiation, from a material which is excited by some form of electromagnetic radiation incident in the ultraviolet, visible, or infrared regions. Such emission is the release of the energy gained from the absorption of the incident photon energy. It may be either fluorescence or phosphorescence, or both, while the distinction between the latter two terms is often somewhat arbitrary<sup>[35]</sup>. In conformity with current usage in the application field discussed hereby, the term fluorescence will be applied generally to all sort of photoluminescence, and the corresponding luminescent materials will be termed as fluorescent materials or "phosphors", thereafter.

The excitation spectrum of a fluorescent material, that is the incident radiation spectrum required for the induction of fluorescence, is determined by the absorption spectrum of the fluorescent material, which it often closely resembles, and by the efficiency with which the absorbed energy is transformed into fluorescence. Normally, the excitation spectrum is of higher photon energy (shorter wavelength) than that of the corresponding fluorescence. This is well demonstrated by the excitation and fluorescent emission spectra, shown in Figure 1.6, of the tetravalent manganese activated magnesium fluorogermanate<sup>[36]</sup>, which is well-known as colour corrector for high pressure mercury vapour street lamps and has been used as the sensing material in a fluorescence based fibre optic thermometer scheme by Luxtron<sup>[28]</sup>. In this scheme, a xenon flash lamp is used as excitation light source. In Figure 1.7 is another example given by the absorption and emission spectra of a newly developed laser material  $\text{LiSrAlF}_6: \text{Cr}^{3+}$ <sup>[37]</sup>, an analysis of the fluorescence lifetime of which is quite useful for temperature sensing in bio-medical

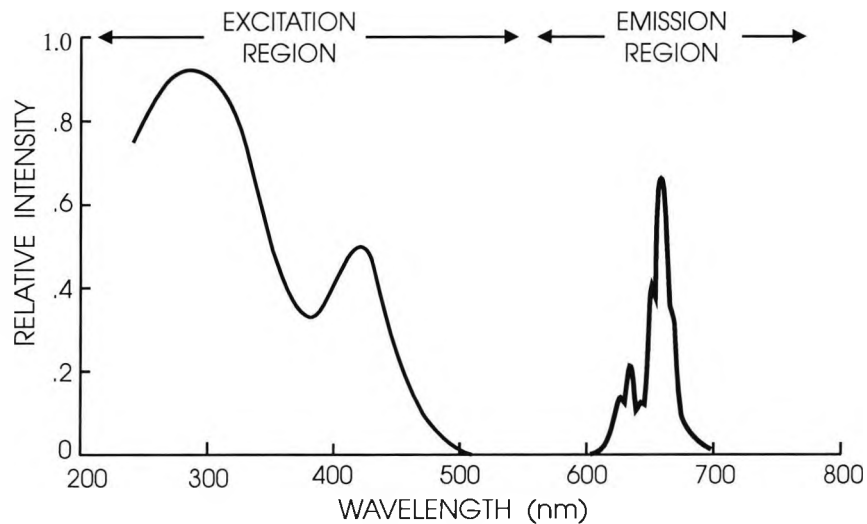


**Figure 1.6:** Excitation and emission spectra of magnesium fluorogermanate activated with tetravalent manganese.

region [38,30]. A compact and low cost visible laser diode emitting at 670nm can effectively induce fluorescent emission from this chromium activated material.

The initial persistence of fluorescent emission following the removal of excitation depends on the lifetime of the excited state. This emission decays exponentially and the time-constant of such a exponential decay is used as the measure of the lifetime of the excited state, often termed as *fluorescence lifetime* or *fluorescence decay time*. In fluorescence thermometry, most materials used have relatively longer fluorescence lifetimes ( $> 10^{-6}$  s). It means that fluorescence corresponds to weakly allowed transitions between

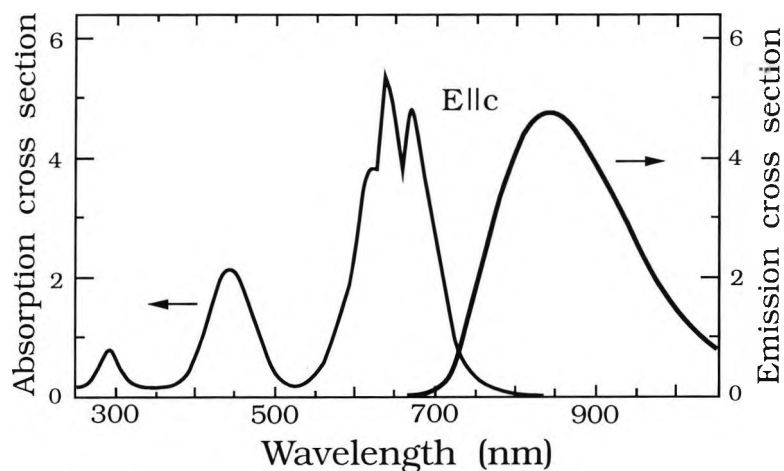


**Figure 1.7:** Absorption and emission spectra of  $\text{LiSrAlF}_6: \text{Cr}^{3+}$ .

electronic energy levels of the fluorescent material. The material emits light because that is one of the ways for the electron, once excited by incident radiation, to give up its energy and to return from the excited state to the ground one. Any reasonably effective competitive relaxation process can shorten the lifetime of the excited state. A variety of competitive processes, some radiative and some non-radiative, exist. Hence all luminescent materials can be expected to exhibit a temperature-dependent fluorescence lifetime, and temperature-dependent fluorescence intensity over some temperature range. These are the thermal properties used in fluorescence thermometry.

Several classes of potentially useful fluorescent materials exist. Most lamp phosphors and many solid state materials are insulating compounds containing ionic "activators". The spectra of the rare-earth activators resemble, to a first approximation, of those of free ions, while the electronic spectra of the transition-metal activators differ from those of free ions quite significantly due to the strong interaction with the crystal fields of host materials. Many of the early CRT and television phosphors are semiconductors such as ZnS, CdS, or CdZnS, the emission from which corresponds approximately to the semiconductor band edge observed in absorption. There are also organic materials, both liquid and solid, which exhibit "molecular" fluorescence. Finally there are self-activated materials and materials with charged defects (colour centres) which also exhibit fluorescence.

The choice of sensor material determines range, sensitivity, and stability. By considering the latter factors, it is found that inorganic insulating compounds, such as most lamp phosphors and many solid state laser materials, are the most suitable materials for thermometric applications. Indeed, these materials are most commonly used in the existing fluorescence thermometer schemes.

Finally it is worth of mentioning the relation between fluorescence properties and the concentration of activator content. The fluorescence intensity increases initially with increases in the concentration of activator content. However, the increase in the concentration above a certain critical value can lead to a reduction in fluorescence intensity. This is called *concentration quenching*. It can also be observed from the reduction in the lifetime with the increase in the concentration, as shown in Figure 1.8 in the case of ruby, where

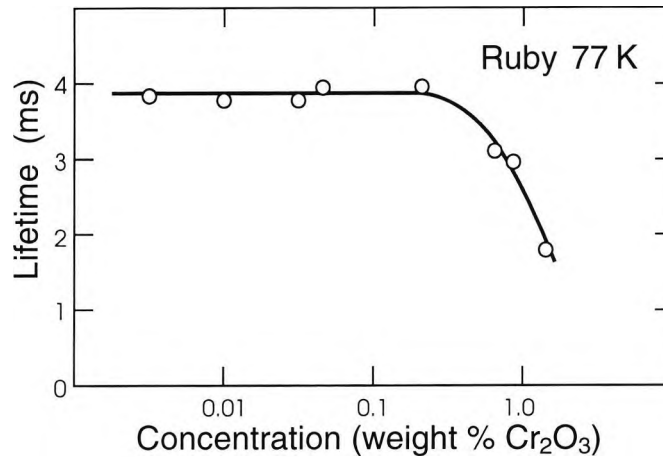


**Figure 1.8:** An example of concentration quenching. In ruby the observed decay time of the fluorescence at 77 K is independent of chromium concentration up to a concentration of around 0.3 weight % of Cr<sub>2</sub>O<sub>3</sub> in the material [39].

the activator is the Cr<sup>3+</sup> ion. Therefore, it is of advantage to select an activator concentration short of the critical value to achieve a good level of fluorescence intensity.

### 1.3.2. Early fluorescence thermometer schemes

A variety of fibre optic thermometry systems using fluorescence sensors have become available over the past few years. Most of the earliest systems are based on the temperature dependent fluorescence intensity of appropriate materials. One example of early commercial systems is the Luxtron model 1000, shown as Figure 1.9, which utilised europium-activated lanthanum and gadolinium oxysulphide as alternate sensor materials [19]. The fluorescence from these rare-earth phosphors consists of sharp lines originating from different excited states of the trivalent europium ion. Since the relative populations of these excited states after excitation are strong functions of temperature, the relative intensities of the emission lines are also quite temperature dependent. By measuring the intensities of two lines originating on different excited states, the system derives the temperature from the ratio of the line intensities.

Another example of early systems is the ASEA model 1010, shown as Figure 1.10, introduced by ASEA AG, a large Swedish automation and energy systems company. In this system, the sensor is a small crystal of gallium arsenide sandwiched between gallium aluminum arsenide layers [40]. The sensor is caused to luminesce in the vicinity of its band absorption edge by radiation from a gallium arsenide LED. As the temperature of the

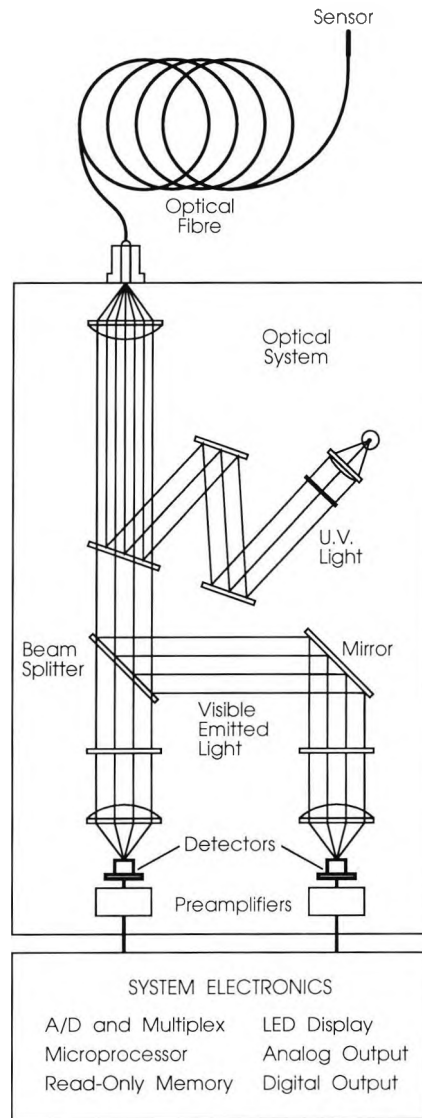


**Figure 1.9:** Schematic representation of Luxtron model 1000 [19].

sensor is raised, its emission broadens and shifts to progressively longer wavelengths. Portions of the luminescence are transmitted through two optical filters with adjacent pass bands, the intensity in each pass band is measured, and a ratio is constructed which can then be correlated with temperature.

Although a substantial number of intensity-based systems, such as the Luxtron model 1000, the ASEA model 1010 and the like, were built, it was seen that the technique had limitations in terms of performance and cost [28]. These limitations stem from the need of an additional "referencing channel", e.g. the luminescence intensity at another wavelength, for the separation of the effects of thermally induced changes in intensity from other

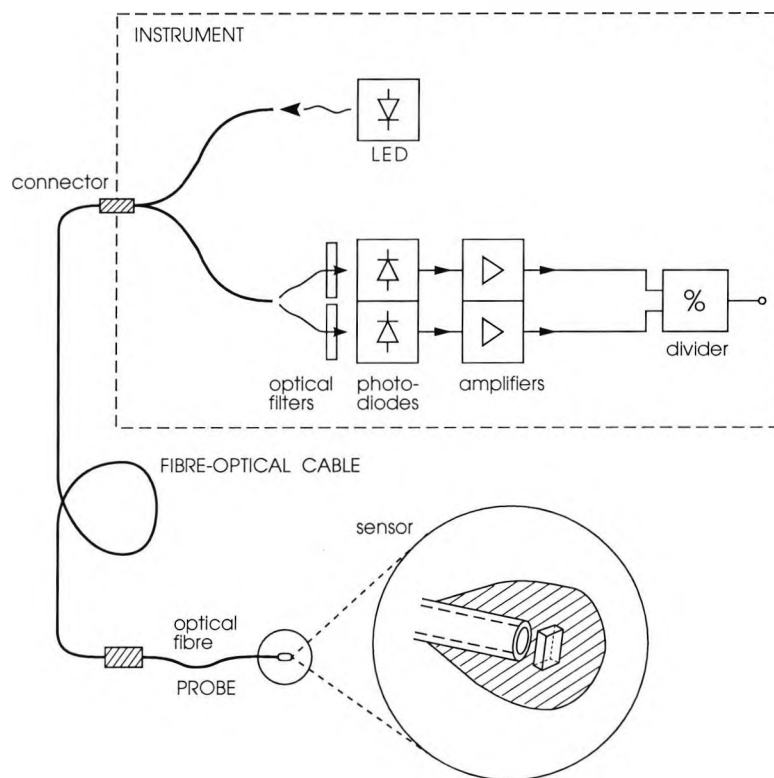


**Figure 1.10:** ASEA model 1010 temperature sensor [40].

non-thermal sources of signal change, such as fibre bending, light source and detector degradation, etc. As a result, the technique based on the measurement of fluorescence lifetimes was developed [18, 20, 21] and it is much preferred in the development of fluorescence-based commercial systems to date.

### 1.3.3. Fluorescence lifetime-based schemes

In such a category of schemes, the temperature-dependent lifetime of fluorescence in appropriate material is utilised. There are a variety of fluorescent materials potentially useful for temperature sensing, as mentioned in section 1.3.1., and those materials which have been used, were often selected with relatively longer lifetime ( $> 10^{-6}$  s) so that no special high speed electronic components are needed and the design of lifetime detection electronics could be simple and low cost. Since the temperature of an appropriate fluorescent material can be determined from the measurement of a single intrinsic parameter (its fluorescence lifetime), the system in this category is to a first approximation calibration-

free. With such system, virtually any probe configuration can be used interchangeably since the measurement of the fluorescence lifetime does not depend on the exact signal level or on the particular optical configuration.

In addition to choosing the right fluorescent material to meet the requirement of the desired applications, the achievement of an effective, simple and economic electronics scheme for the detection of the fluorescence lifetime is also critical in the development of an acceptable sensor system with potential for commercialisation. Quite a few signal processing techniques for the detection of the fluorescence lifetime have been used in fluorescence-based thermometry systems. Indeed, all these systems can be categorised according to the signal processing techniques used, in the following items.

#### **1.3.3.1. Pulse measurement of fluorescence lifetime**

The common feature of the schemes in this category is that the excitation light applied to the fluorescent material is a high intensity "delta" function pulse (e.g. a laser pulse or that from a flash lamp) or an rectangular pulse, and the measurement is derived from the observation of the fluorescence decay after the removal of the excitation light. The following are the outlines of some typical schemes which are of this type and have been used in thermometry applications.

##### ***Two-point time constant measurement:***

This is a very straightforward method which was used by several groups of workers in the early stage of the development of a fluorescence-based sensor system [21, 28, 41]. The fundamental principle of this technique can be well illustrated in Figure 1.11. This is to compare the intensity level at two points along the exponential decay curve after the excitation pulse has terminated. The circuitry is designed to measure first the value of decaying signal,  $I_0$ , that occurs at a fixed time,  $t_1$ , after the termination of the excitation pulse. A second voltage  $I_0/e$  is then calculated and established as a reference level. When the decaying signal falls to that level, the time  $t_2$  at which crossover occurs is noted. The interval between  $t_2$  and  $t_1$  is the time constant,  $\tau$ , of the exponentially decaying signal. In most cases, the fluorescence decay process observes a single or "quasi-single" exponential law, as that shown in Figure 1.11. Thus time constant,  $\tau$ , is used as the measure of fluorescence lifetime.

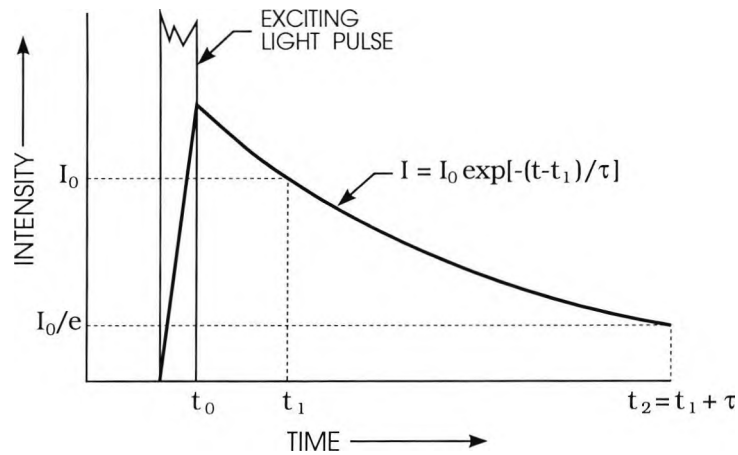


**Figure 1.11:** Two-point time constant measurement technique [28].

Timing circuits are provided for measuring precisely the time between  $t_2$  and  $t_1$ . That time difference can be correlated directly with the temperature of the fluorescent sensor by reference to an empirically determined "look up" table stored digitally within the instrument.

This type of method is simple and inexpensive in relation to the electronic components used. Since the fluorescence signal is measured after the excitation pulse is over, the detector optics do not have to be designed to discriminate strongly against stray signals from the excitation source. However, a significant disadvantage of this type of system is that the signal is only measured at two times and, as a result, precision is rather limited.

This two-point measurement technique is used in the system reported by Wickersheim and Sun [28], where a lamp phosphor, tetravalent manganese activated magnesium fluorogermanate, mentioned above is used as fluorescent sensor. The excitation and emission spectra of this sensor material are shown in Figure 1.6. With a xenon flash lamp used as the excitation source, the observed fluorescence lifetime ranges from approximately 0.5 ms at 450°C to more than 5 ms near liquid nitrogen temperature. It is claimed that an accuracy of  $\pm 2^\circ\text{C}$  over the whole range can be achieved without calibration of the instrument. With a single point calibration,  $\pm 0.2^\circ\text{C}$  accuracy is claimed.

**Integration method:**

To achieve higher precision from the pulse measurement, several techniques have been developed which are based on the integrations of the decaying fluorescence signal over different periods of time. One example is the signal processing scheme used by Sholes and Small [18] in their non-fibre study of ruby fluorescent decay. As illustrated schematically in Figure 1.12, when the decaying fluorescence falls below a preset level, the start of the measurement process is triggered. The signal is integrated at two fixed delay times,  $T_1$  and  $T_2$ , and then the integration values over these periods of time,  $A$  and  $B$  are sampled. After the signal has decayed to zero, the integrator is reset and restarted. Integrated noise and dc offset levels are then sampled for the same two fixed delays, and are given by  $C$  and  $D$ , which are equivalent to the noise and dc offset components in  $A$  and  $B$  respectively. Therefore, the fluorescence lifetime,  $\tau$ , could be obtained by solving the following implicit relation:

$$\frac{A - C}{B - D} = \frac{1 - e^{-T_1/\tau}}{1 - e^{-T_2/\tau}} \quad (1-1)$$

Another example is the balanced integration method described by Sun [42]. This technique is designed to achieve  $0.01^\circ\text{C}$  resolution using tetravalent manganese activated

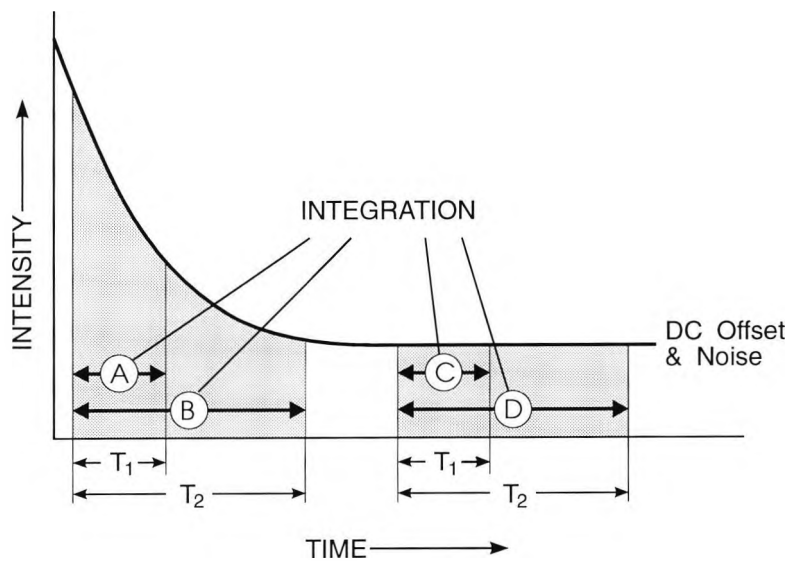


**Figure 1.12:** Schematic illustration of the integration technique used by Sholes and Small (1980) [18].

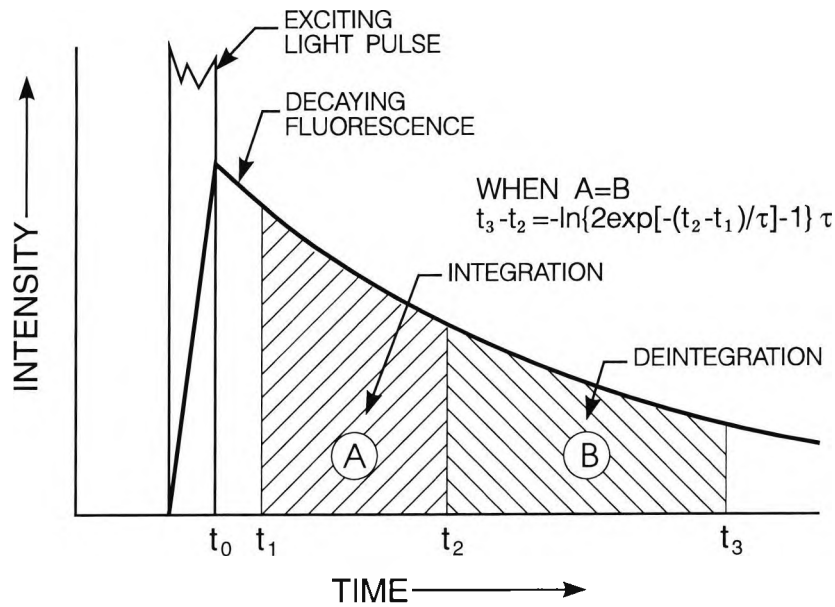


**Figure 1.13:** Illustration of the balanced integration method.

magnesium fluorogermanate, the same sensor material which have been used with the two-point measurement by Wickersheim and Sun [28], as mentioned above. The system utilises a dual-slope integrator to balance the integrals of two sequential areas under the decay curve of the phosphor, as shown in Figure 1.13. The first integration is carried out over a preselected fixed time interval. Integration starts at a predetermined time,  $t_1$ , after the excitation pulse has terminated. Upon completion of this initial integration, i.e. at  $t_2$ , polarity is reversed and negative integration (deintegration) begins. This continues until the second integrated area exactly equals the first and the combined integral equals zero. The time of the zero crossing,  $t_3 - t_2$ , is measured with high resolution ( $t_0 < 20\text{ns}$ ). The observed value of  $t_3$  can be related to the decay time of the phosphor and hence to its temperature.

The result of this balanced integration system is very sensitive to any background signal, whether optical or electronic. Hence ac noise must be minimised and any dc offsets must be measured and corrected, e.g. in some way similar to that used by Sholes and Small [18] and illustrated in Figure 1.12. It is also be pointed out that the dynamic range of this system is fairly narrow ( $\sim 100^\circ\text{C}$  for a given choice of the initial integration period) relative to that of the less precise two-point system [42].

### Digital curve fit method

Recently Luxtron has introduced a modular system WTS-11 designed to monitor winding temperature in power transformers <sup>[43]</sup>, utilising a technique which takes advantage of the newest, commercially available, high-speed digital signal processors (DSPs), and it has been described in detail by Sun <sup>[42]</sup> and is termed "digital curve fit method".

In this system, an un-named fluorescent material is used, the excitation spectrum of which allows the use of a convenient excitation source, e.g. a red LED or laser diode. When the sensor is excited by sequential light pulses from an LED or laser diode, a repetitive decaying luminescent signal results. A selected portion of each decay curve is digitised after the detected signal has passed through a low noise, wide bandwidth amplifier. The digital samples, after correction for any offset, shown in Figure 1.14, are then processed by the DSP to provide the best exponential by means of a least squares curve fitting technique. The exponential is first converted to a straight line by taking the natural logarithm of the digitised signal values. The slope of the best fit straight line is proportional to the decay time of the luminescence.

The result of a number of curve fits are averaged to further reduce the effects of noise. The averaged decay time is then compared with values stored in a digital look-up table to determine the temperature of the sensor.

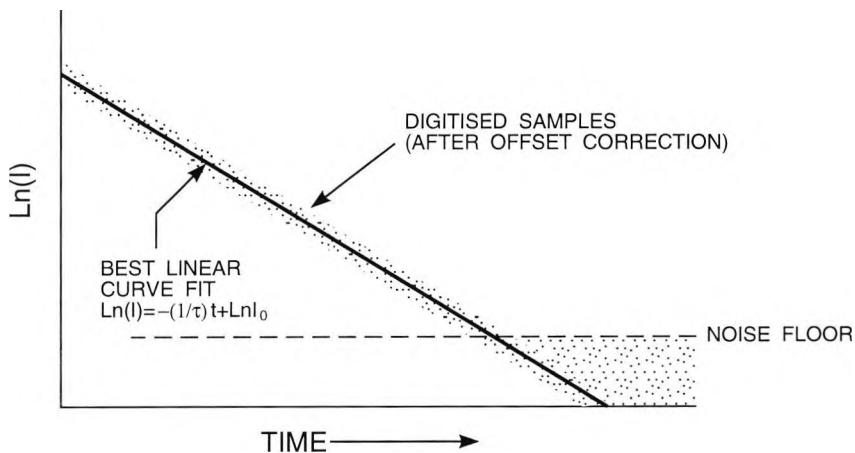


Figure 1.14: Illustration of linearised digital curve fit technique.

The use of this technique with a DSP has resulted in a rather compact instrument . It was reported that the development of this technique is aimed to eliminate dependence on many of the drift-prone components and should thereby improve system stability [42]. However, no assessment of it in such aspects was given by the reporter.

In fact, an investigation into the errors caused by baseline offset and noise in the least-squares estimation of exponential lifetimes, has already been carried out by Dowell and Gillies [44]. It shows that the two-parameter estimation, which only estimates  $I_0$  and  $\tau$  and assumes zero baseline (or called dc) offset such as that illustrated in Figure 1.14, is rather sensitive to small, residual baseline offset. The normalised lifetime-estimation error is proportional to the normalised offset. The ratio is greater than 3 when the normalised observation time  $\beta > 3$ , where  $\beta = T/\tau$ ;  $T$  is the actual time of observing the signal and  $\tau$  the lifetime. Therefore, as a matter of fact, the performance of the digital-curve-fit technique will greatly rely on the effectiveness of the measure utilised to correct the dc offset in the observed signal. The three-parameter least-squares estimation, that is, including the estimation of the dc offset, might be a better solution. However, it requires a reiterative numerical algorithm, and this will not only increase the complexity of programming, but also greatly prolong the signal processing time.

### 1.3.3.2. Phase and modulation measurement

A schematic representation of this category of techniques is depicted in Figure 1.15. The intensity of the excitation light is sinusoidally modulated so that the fluorescence response from the sensor material is forced to follow the same sinusoidal law, but lagging behind the excitation light by a phase shift  $\varphi$ , which is expressed as

$$\tan\varphi = 2\pi f\tau. \quad (1-2)$$

Thus, the fluorescence lifetime  $\tau$  can be derived from a measurement of  $\varphi$ .

This technique is of high accuracy and is meant to be used in precision measurement instrumentation, for it is inherently insensitive to dc-offset and the ac-noise in the sinusoidal signal which can be substantially reduced by a great variety of electronic devices ranging from various electronic analogue filters, digital filters to the most effective lock-in amplifiers.

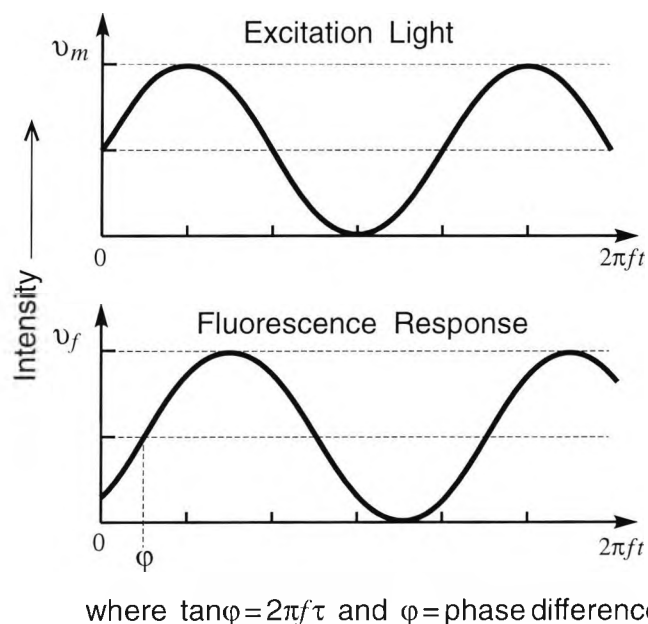


**Figure 1.15:** Phase and modulation measurement of fluorescence lifetime.

At the early stage of development, the lack of a convenient and economic excitation modulation scheme, has limited the use of such a phase shift technique in fluorescence thermometry. Now with the wide availability of cheap and easily modulated high-power LEDs or laser diodes, this technique has found its application in the thermometry area. Grattan *et al* [29] have demonstrated the use of this technique in a ruby fluorescence-decay thermometer, where a high-power green LED was used as the excitation light source. Over the range from room temperature to 170°C, a quite satisfactory measurement deviation was achieved under a poor signal-to-noise ratio condition. A similar system was also reported by Augousti *et al* [45], which uses alexandrite as the sensor material and was capable of accuracy of  $\pm 1^\circ\text{C}$  over a range 20-150°C, with a response time of 1s.

However, since the kind of system requires the measurement of fluorescence during the excitation period, it is highly sensitive to the excitation light leakage to the detector and the optics required to prevent such leakage would make the system quite costly.

### 1.3.3.3. Phase-locked detection of fluorescence lifetime

This is a new category of signal processing approach, which has been developed for the achievement of a simple, inexpensive and versatile electronic scheme for the detection of fluorescence lifetime, and has been successfully applied to several fibre-optic ther-

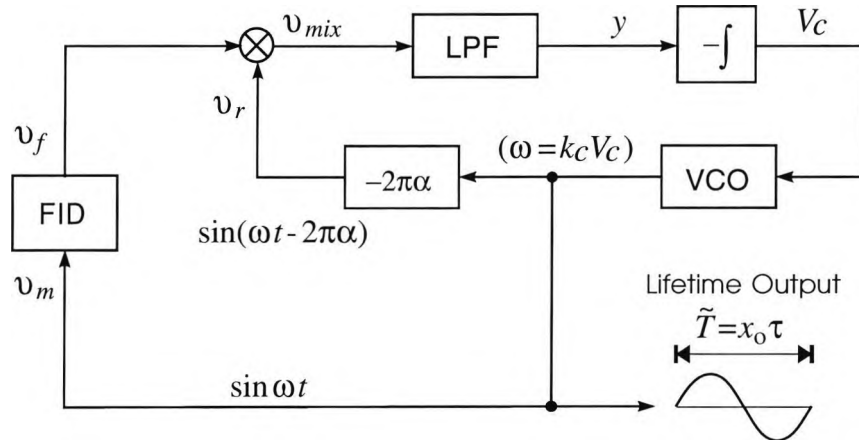


**Figure 1.16:** Phase-locked detection of fluorescence lifetime using single reference signal. FID: fluorescence inducing and detecting devices;  $v_m$ : signal to modulate the output intensity of the excitation light source;  $v_f$ : the fluorescence signal; LPF: low-pass electronic filter; VCO: voltage-controlled oscillator.

momenter schemes. Though as illustrated schematically in Figure 1.16, these schemes stem from the *phase and modulation techniques*, but they differ from them in several important aspects. In general, the excitation light source is modulated by a signal from a voltage-controlled oscillator (VCO), either a sine-wave or square wave. The fluorescence response signal from the sensor follows the variation of excitation light in intensity, but lags behind it by a phase shift,  $\phi$ , which corresponds to the fluorescence decay time as expressed in Eq.(1-2). This signal is sent to a lock-in amplifier to mix with a reference signal derived from the VCO output with a phase lag of a fixed fraction,  $\alpha$ , of the period. Then the resulting mixed signal is filtered by a low-pass filter (LPF) and further integrated. The resultant voltage signal is fed back to control the output frequency of the VCO. The VCO will finally be driven to operate at a frequency at which the integration of the mixed signal is zero. The period of this frequency is directly proportional to the lifetime, and thus the measurement. This allows a high resolution to be achieved over a wide range of lifetimes. It has been found in such systems that while the frequency varies with the fluorescence lifetime, the phase shift between the excitation and fluorescence signals is always kept at a constant value, determined by the reference delay ratio,  $\alpha$ . Therefore this category of techniques has been termed "phase-locked detection" by Zhang *et al* [31].

### ***Closely related early scheme - simple oscillator method:***

The earliest scheme which is closely related to the *phase-locked detection* technique is that described by Bosselmann<sup>[46]</sup>. In this scheme, a positive feedback is formed by sending the fluorescence response signal back to control the output intensity of the excitation light source, via a timing circuit which amplifies the signal with an added phase shift, so that the system will oscillate at a frequency determined by the combination of the time-constant of the timing circuit and the fluorescence lifetime. The measurement of the lifetime is derived from the oscillating frequency, which is subject to the parameter drifts of the timing circuit. The sensitivity of the frequency to the lifetime is also limited by the fact that is given by the combination of the lifetime and the time-constant of the timing circuit.

### ***Phase-locked detection using single reference signal:***

A revision of the simple oscillator method was reported later by Bosselmann *et al*<sup>[20]</sup> which gives a primitive form of the phase-locked detection technique, and has been classified as the *phase-locked detection using single reference signal* by Zhang *et al*<sup>[31]</sup>. The operation mechanism of this scheme is similar to that depicted in Figure 1.16 except that a VCO of square-wave type is used, that is, the excitation light is square-wave modulated. The sensor material used in the thermometer system is a chromium-activated rare earth aluminum borate. In this system, the standard deviation of consecutive measurement is 0.04°C over the temperature region from 0 to 70°C, and no detectable long term drift is observed.

A conclusion that the measurement sensitivity of using square-wave modulation is greater by a factor of 2 than that of using sinusoidal modulation was made by Bosselmann *et al*<sup>[20]</sup> from a comparison between this primitive phase-locked detection scheme and the simple oscillator scheme mentioned before. In fact, the fundamental difference between these two techniques lies in their configurations instead of the modulation modes used. In the simple oscillator system, the fluorescent material is directly used as a timing component in a oscillator by means of opto-electronic coupling, and hence the oscillating frequency is determined by the combination of the fluorescence lifetime and the time-constant of an additional electronic timing circuit, which limits the sensitivity of the oscillating frequency to the lifetime. However, in the phase-locked detection system, the oscillation is generated by a voltage-controlled oscillator with the oscillating frequency only controlled by the

fluorescence lifetime, and thereby the sensitivity of the frequency to the lifetime is higher than that in the former case.

Perhaps the first detailed discussion of such a technique (shown in Figure 1.16) was given by Zhang *et al* in the work <sup>[47]</sup> related to this thesis, based on both mathematical analysis and experimental simulation. Examples of the electronic design of the corresponding system and the application of the technique in a ruby fluorescence-based fibre-optic sensor system are also listed. This shows that there is no difference in the measurement sensitivity between a system using square-wave modulation and one using sinusoidal modulation. However, the former performs a little better in terms of the measurement resolution.

As demonstrated by the work of several groups of workers <sup>[20, 47, 48]</sup>, this system is highly suitable for high precision, wide range applications. However, like the phase and modulation measurement schemes, since the system requires measurement of fluorescence during the excitation period, even a tiny fraction of excitation light leaking into the photodetector will seriously degrade the performance of the system. An excess of such leakage can even cause the operation of the system to fail <sup>[31]</sup>. Therefore, high quality optics might be needed to prevent such leakage and this would make the system rather costly and bulky.

### ***Phase-locked detection using two reference signals***

The problem of excitation light leakage in a high-temperature sensor scheme based the fluorescence lifetime of crystalline alexandrite <sup>[49]</sup>, has led to the introduction of a new version of the phase-locked detection technique, termed the *phase-locked detection using two reference signals* by Zhang *et al* <sup>[31]</sup> in this thesis. In that work <sup>[49]</sup>, two reference signals derived from a VCO output are used to mix successively with the fluorescence signal, so as to delete the excitation leakage component from the final integration of the mixed signal which is used to control the oscillating frequency of the VCO. It has been proved theoretically and experimentally, that such a technique is intrinsically immune to the impact of excitation light leakage. Therefore, in the phase-locked detection system, it is no longer necessary to use high cost optics in the optical arrangements.

In the system which uses crystalline alexandrite as the sensor material [49], a measurement reproducibility of  $\pm 1^\circ\text{C}$  is achieved over a wide temperature region from 20 to  $700^\circ\text{C}$ . The same technique is applied to another fibre optic thermometer system which is designed for bio-medical sensing applications and uses  $\text{LiSrAlF}_6:\text{Cr}^{3+}$  as sensor material [38]. The standard deviation of the measurement recorded by this system is better than  $0.01^\circ\text{C}$  within the  $20^\circ\text{C}$  and  $50^\circ\text{C}$  region.

The easing of the requirement for high quality optics by using this two reference technique, and employing those characteristics which are somewhat inherent to the phase-locked detection techniques, such as high precision, wide measurement range and so on, would make this category of technology much to be preferred in the development of cost-effective fluorescence-based fibre-optic thermometers.

## 1.4. Structure of the thesis

This thesis is comprised of the work carried out by the author in the development of the fibre optic fluorescence thermometry. Beginning with an introduction to the subject of fibre optic fluorescence thermometry as presented above, the work will then explore theoretical basis of the fluorescence thermometry: the temperature dependences of fluorescence materials in Chapter 2. Mostly based of the original work of the author, the discussion will concentrate on the temperature dependences of the fluorescence characteristics and lifetimes of  $\text{Cr}^{3+}$  doped materials. A number of models will be given which can successfully interpret the great variety of the temperature dependences shown by the fluorescence lifetimes of  $\text{Cr}^{3+}$  doped materials, according to the crystal field strengths of the host materials. The great variety of such temperature dependences as well as other spectroscopic characteristics, e.g. the wide-band absorption spectrum, fluorescent emission over the deep red to infrared part of spectrum which is easy to detect, have made  $\text{Cr}^{3+}$  doped materials be one group of the most promising sensor materials for fluorescence thermometry use.

Chapter 3 discusses work contributing to the instrumentation aspects of the fluorescence thermometry with the presentation of a category of novel, effective and versatile instrumentation approaches: the *phase-locked detection of fluorescence lifetimes*. Examples of the applications of these techniques in various successful fibre optic thermometer schemes are presented in Chapter 4. The opto-electronic construction of the related thermometers, the fabrication of the fibre probes for biomedical or high temperature applications, as well as other instrument design considerations are covered in Chapter 4. In addition, the development of a special, gold-coated high temperature fibre probe is also described in this Chapter.

In Chapter 5, the possibility of extending the measurement range of fibre optic temperature sensor, is discussed by means of the cross referencing between blackbody radiation and fluorescence lifetime, in a new approach independently proposed by the author and co-workers.

Finally, the conclusion of this work is presented in Chapter 6, together with the points of the author's view on the aspect of the future work and further development of the fluorescence thermometry.

## **1.5. Aims and objectives of the thesis**

- (1) Investigate established work on fluorescence thermometry;
- (2) Develop and examine the theoretical basis of the fluorescence of suitable materials;
- (3) Develop and examine new electronic schemes;
- (4) Develop experimental systems for a range of temperatures
- (5) Cross compare results with previous work - limitation of the methods.

# Temperature Dependences of Cr<sup>3+</sup> Fluorescence Lifetimes

---

## 2.0. Abstract

In this Chapter, the temperature dependences of the fluorescence lifetimes of Cr<sup>3+</sup> doped insulating crystals, which have been used as temperature sensing elements or have such potential uses over different temperature regions, are reviewed in terms of their crystal field strengths. Two single configurational coordinate models are developed to aid the interpretation of the temperature dependence of Cr<sup>3+</sup> fluorescence in materials with low and high crystal field strengths, respectively. The validities of the two models are seen in their close fit to the lifetime data of Cr<sup>3+</sup> fluorescence in appropriate materials. The content of this Chapter forms the theoretical background of the entire thesis work. It shows that the temperature dependence of the fluorescence lifetime is intrinsic to the physical properties of the fluorescent material itself. As such, the temperature dependence is reproducible from material to material, and is of particular thermometric use. The models discussed here are also applicable to selection of a suitable fluorescent material for thermometric application over a specific temperature region, or to be used as empirical calibration formulae in the operation of various Cr<sup>3+</sup> fluorescence lifetime-based thermometers.

## 2.1. Introduction

The transition metal ions,  $\text{Cr}^{3+}$ , are widely used as active dopants in solid-state laser crystals. Unlike rare-earth ions such as  $\text{Nd}^{3+}$ ,  $\text{Cr}^{3+}$  ions in ionic crystals interact strongly with the crystal-field strength and the lattice vibrations. Thus  $\text{Cr}^{3+}$  activated materials are characterised by a wide optical absorption spectrum spanning the ultra violet (UV) through the red portion of the visible spectrum. This allows the use of cheaper and compact light sources for excitation, such as high power LEDs and visible laser diodes, highly suitable for practical sensor applications. Again due to the strong crystal-field interaction, the energy gaps of the electronic levels of  $\text{Cr}^{3+}$  ions vary from one host crystal to another, as do the temperature dependences of the fluorescence lifetimes of  $\text{Cr}^{3+}$  doped materials. Therefore, significant variety in such temperature dependent phenomena is observed and a useful level of control of this temperature dependence is made possible by systematic changes in the crystal field strength, through the variation of the host material or the crystal composition, to cater for differing thermometric needs over various temperature regions.

The electronic energy levels of the  $\text{Cr}^{3+}$  ion are well illustrated by the Tanabe-Sugano diagram<sup>[50]</sup> which plots  $E/B$ , the normalised energy of the low-lying excited states as a function of the normalised octahedral crystal-field strength  $Dq/B$ . A simplified Tanabe-Sugano diagram is presented in Figure 2.1, for the  $\text{Cr}^{3+}$  ion in an octahedral crystal field. The ground state is always the orbital singlet,  ${}^4A_2$ , irrespective of the strength of the octahedral crystal field. The energy splitting,  $\Delta E$ , between the low lying states,  ${}^4T_2$  and  ${}^2E$  is defined as:

$$\Delta E = E({}^4T_2) - E({}^2E). \quad (2-1)$$

It varies strongly with  $Dq/B$  and may be positive or negative, as shown in Figure 2.1. The broken lines indicate the energy level positions of a number of different crystals. In a high strength crystal field,  $Dq/B \gg 2.3$  as in ruby ( $\text{Al}_2\text{O}_3:\text{Cr}^{3+}$ ) and alexandrite<sup>[51]</sup>;  $\Delta E > 0$  ( $2350 \text{ cm}^{-1}$  and  $\sim 800 \text{ cm}^{-1}$  for ruby<sup>[52]</sup> and alexandrite<sup>[51]</sup> respectively), and the  $\text{Cr}^{3+}$  emission is dominated by the sharp *R* lines ( ${}^2E \rightarrow {}^4A_2$  transition). However, by contrast in a low strength crystal field,  $Dq/B \ll 2.3$ , as in LiSAF ( $\text{LiSrAlF}_6$ );  $\Delta E < 0$  and the dominant emission is the broad  ${}^4T_2 \rightarrow {}^4A_2$  band transition. The intrinsic lifetime of the  $\text{Cr}^{3+}$  ions of  ${}^4T_2$  is much shorter than that of the  ${}^2E$  state, e.g.  $6.6\mu\text{s}$  and  $1.54\text{ms}$  for  ${}^4T_2$  and  ${}^2E$

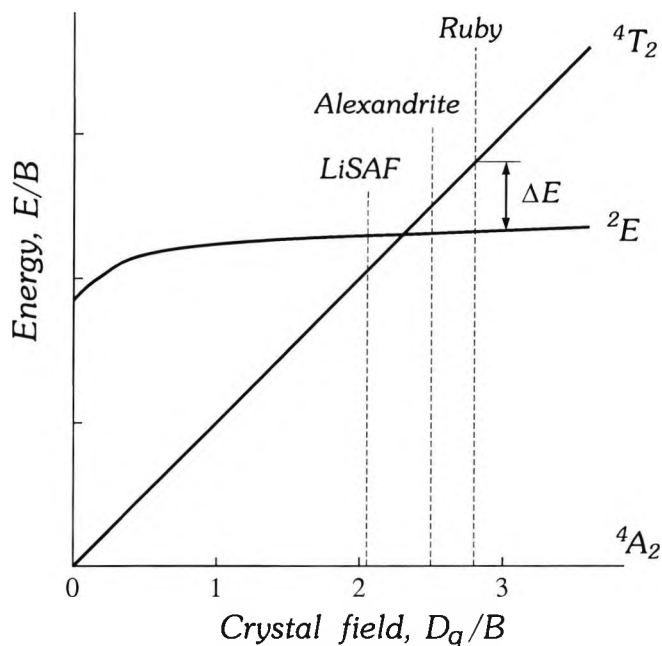


**Figure 2.1:** Simplified Tanabe-Sugono diagram. The broken lines represent the approximate energy level positions of the  $\text{Cr}^{3+}$  ion in various host crystals.

respectively in alexandrite<sup>[51]</sup>, and so the magnitude of  $Dq/B$  also gives the temperature dependence of the  $\text{Cr}^{3+}$  fluorescence lifetimes, showing different characteristics. For instance, in the case of  $Dq/B \gg 2.3$ , such a temperature dependence is mainly due to the thermally activated repopulation between the  ${}^2E$  and  ${}^4T_2$  states, over a wide temperature region (e.g. 300 ~ 600K for ruby and 150 ~ 700K for alexandrite). In the case of  $Dq/B \ll 2.3$ , the  ${}^2E$  state has little to do with this temperature dependence which is mainly determined by the non-radiative process of the  ${}^4T_2 \rightarrow {}^4A_2$  transition or the so-called *thermal quenching of fluorescence*.

Therefore, in the present study, the temperature dependences of the fluorescence lifetimes of  $\text{Cr}^{3+}$  doped insulating crystals, which have been used as temperature sensing elements or have such potential uses over different temperature regions, are reviewed in terms of the influence of the crystal field strength. The success of modelling work on the temperature dependences of  $\text{Cr}^{3+}$  fluorescence lifetimes is presented, and as a result empirical formulae resulting from the above work may be applied to fit the experimental

data of fluorescence lifetimes of  $\text{Cr}^{3+}$  in different host crystals, showing the potential for this to be used in the assessment and calibration of thermometers based on such materials.

## 2.2. Temperature dependence of $\text{Cr}^{3+}$ fluorescence in low field crystals

In a low crystal field, the lowest excited state is  ${}^4T_2$ . The  ${}^2E$  state is less populated by the excited  $\text{Cr}^{3+}$  ions, according to Boltzmann principle. Furthermore, due to the fact that the  ${}^2E \rightarrow {}^4A_2$  transitions are doubly forbidden by parity and spin, these transitions are one or two orders of magnitude weaker than the  ${}^4T_2 \rightarrow {}^4A_2$  transitions. Therefore their impact on the fluorescence lifetime, which is mainly determined by the radiative and non-radiative processes of the  ${}^4T_2 \rightarrow {}^4A_2$  transition in the material, is negligible. Its temperature dependence shares a similar profile to that of the fluorescence intensity, as demonstrated in Figure 2.2 by the experimental data of the  $\text{Cr}^{3+}$  fluorescence in the laser crystal LiSAF ( $\text{LiSrAlF}_6$ ), a low crystal field material.

A single configurational coordinate model with only one excited state, as depicted in Figure 2.3, could describe such a temperature dependence qualitatively, and also quantitatively to the extent that it is adequate for the present thermometric applications, as will be shown later. The excited and ground states involved are  ${}^4T_2$  and  ${}^4A_2$  respectively. The  ${}^4T_2 \rightarrow {}^4A_2$  transitions of the excited  $\text{Cr}^{3+}$  ions occur via two processes. One is the radiative transition initiated from **I**, the lowest energy point of the excited state. The other is a nonradiative process, that is the thermal quenching of the  $\text{Cr}^{3+}$  ions which have been thermally elevated to **Q**, the energy crossing of the excited and ground states and which will rapidly lose energy to reach the bottom of the ground state through nonradiative relaxation, as indicated schematically in Figure 2.3. The two processes are continuously competing with each other. The higher the temperature, the more excited ions will be elevated to the level crossing **Q**, and the stronger the nonradiative process will be. Normally the nonradiative transitions are much faster. Therefore, the  ${}^4T_2 \rightarrow {}^4A_2$  transition rates increase with elevated temperature, and a decrease of fluorescence lifetimes with temperature increase is observed.

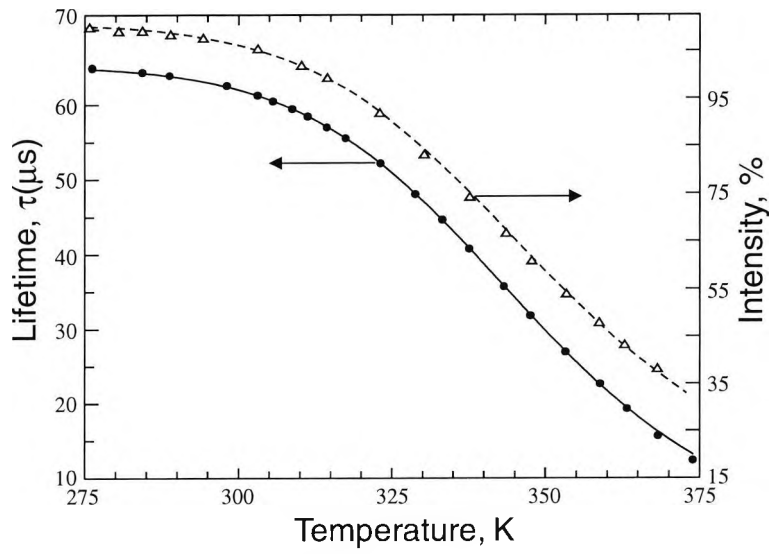


**Figure 2.2:** Thermal characteristics of  $\text{Cr}^{3+}$  fluorescence in LiSAF.  $\bullet \bullet \bullet$ : data for the fluorescence lifetimes.  $\Delta \Delta \Delta$ : data for the fluorescence intensity.

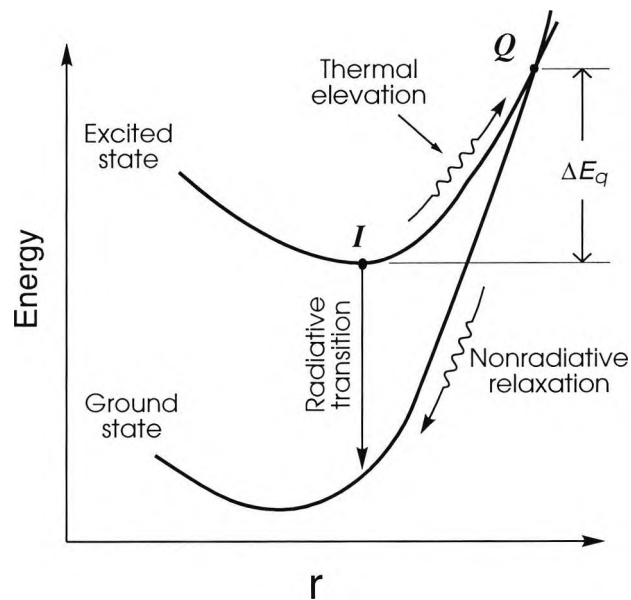


**Figure 2.3:** The single configurational coordinate model for  $\text{Cr}^{3+}$  fluorescence in low field crystals.  $r$ : configurational coordinate.

According to this model,  $1/\tau$ , the transition rate of  $\text{Cr}^{3+}$  in the excited state may be given by:

$$1/\tau = 1/\tau_i + (1/\tau_q) e^{-\Delta E_q / kT}, \quad (2-2)$$

where  $\tau$  is the observed fluorescence lifetime;  $1/\tau_i$  the intrinsic radiative rate at the excited state;  $1/\tau_q$  the thermal quenching rate;  $\Delta E_q$  the thermal activation needed to elevate ions at the bottom of the excited state to the level crossing **Q**;  $k$ , Boltzmann constant;  $T$ , the absolute temperature; and thus  $e^{-\Delta E_q / kT}$  represents the possibility of the excited ions being elevated to the energy corresponding to the crossing of the levels, **Q**. On the assumption that the output power and spectral characteristics of the excitation light source, as well as the absorbance of the luminescent sample over the corresponding spectrum are constant over the temperature region concerned, the observed fluorescence intensity,  $I$ , may be expressed as:

$$I = \frac{I_o}{1 + \beta e^{-\Delta E_q / kT}}, \quad (2-3)$$

where  $I_o$  is a constant determined by the excitation scheme used; and

$$\beta = \tau_i / \tau_q. \quad (2-4)$$

To obtain a direct expression for the fluorescence lifetime, Eq.(2-2) may be rewritten as:

$$\tau = \frac{\tau_i}{1 + \beta e^{-\Delta E_q / kT}}. \quad (2-5)$$

It is clearly shown by Eqs.(2-3) and (2-5), that the temperature dependences of the fluorescence intensity and the lifetime are similar.

The  $\text{Cr}^{3+}$  doped LiSAF is a recently developed laser crystal<sup>[37, 53]</sup>. Its crystal field strength, estimated from the spectroscopic data obtained by Payne *et al*<sup>[53]</sup>, is in the order of  $Dq/B=2.0$ . In the work related to this thesis<sup>[Ref 30]</sup>, it has been shown successfully for use in an fibre optic thermometer for the monitoring of temperature in clinical RF heat treatment. To compare with performance in such an application, Eqs.(2-3) and (2-5) are used in a fit of the experimental data of Cr:LiSAF fluorescence plotted in Figure 2.2 and the results are depicted as the dashed and solid lines respectively. The standard deviation

**Table 2.1:** Empirical values of parameters in the configurational coordinate model of Cr:LiSAF fluorescence.

	$\ln\beta$	$\Delta E_q, \text{cm}^{-1}$	$\tau_i, \mu\text{s}$
Values fitted to the lifetime data	18.89	4557	65.25
Values fitted to the intensity data	18.70	4533	—

for Eq.(2-5) to fit the Cr:LiSAF fluorescence lifetime data over the region 300-353K, is 0.12%, representing a very close agreement. The fitted values of  $\Delta E_q$ , and  $\beta$  as well as  $\tau_i$  are listed in Table 2.1. The differences between these values, fitted to the lifetime and intensity data respectively for  $\ln\beta$  and  $\Delta E$  are only of the order of 1%. These verify that the lifetime and intensity of  $\text{Cr}^{3+}$  fluorescence in LiSAF have the same temperature dependence, a conclusion also obtained theoretically from the configurational coordinate model in Figure 2.3.

Two other crystal materials, LiBAF ( $\text{LiBaAlF}_6$ ) and LiCAF ( $\text{LiCaAlF}_6$ ) are similar to LiSAF in chemical structure, and are also of low crystal field strength. From the spectroscopic data obtained by Stalder *et al* [Ref 54] and Payne *et al* [Ref 53], their crystal field strengths  $Dq/B$  are also in the order of 2.0. The temperature dependences of  $\text{Cr}^{3+}$  fluorescence lifetimes in LiBAF and LiCAF are plotted in Figure 2.4 according to the experimental data of Stalder *et al* [Ref 54], together with that in LiSAF. As shown by these examples, the fluorescence lifetimes of  $\text{Cr}^{3+}$  in the low crystal field are particularly sensitive to temperature variance over a limited temperature region. This characteristic makes the low field crystal materials quite suitable for thermometric applications where high measurement resolution is required over a relative narrow region of temperature, and thus confirm the observation that low field crystal materials can cater for such applications over various temperature regions. Typically, for measurements in the biomedical region, as in the application mentioned before, the temperature dependence of Cr:LiSAF fluorescence lifetime is most useful. Those of the Cr:LiBAF and Cr:LiCAF fluorescence lifetimes can be seen to have a significant potential for applications over the cryogenic region, 100K-250K, and the higher temperature region, 470K-650K, respectively.

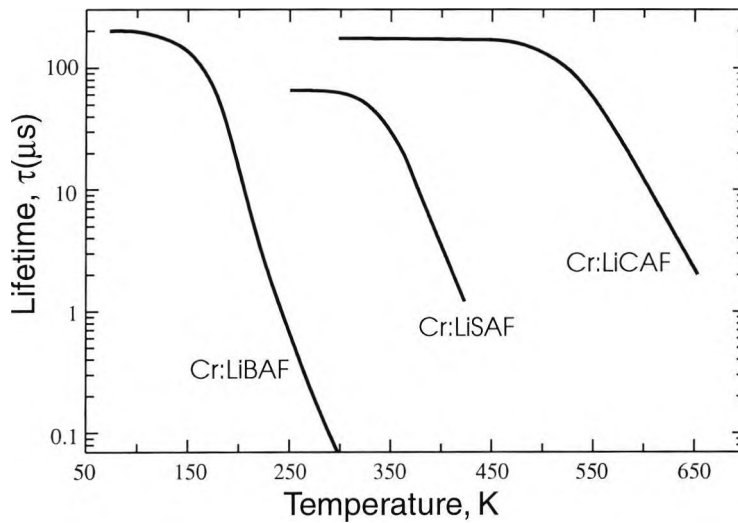


**Figure 2.4:** Temperature dependences of the fluorescence lifetimes of Cr:LiBAF, Cr:LiCAF<sup>[54]</sup>, and Cr:LiSAF.

The lower limit of effective use of the corresponding thermometer,  $T_{\min}$  may be determined by the sensitivity of the fluorescence lifetime to the temperature variance. For instance,  $T_{\min}$  can be selected to be the temperature where the fluorescence lifetime  $\tau$  is reduced to  $\sim 95\%$  of the intrinsic radiative lifetime,  $\tau_r$ , as  $\tau$  is quite insensitive to temperature change below this point and has little value for thermometric use. Due to the decrease of the fluorescence intensity with increasing temperature and the consequently decreasing signal-to-noise ratio, the performance of the thermometer would be expected to deteriorate at higher temperatures. Therefore the upper limit of the effective measurement range,  $T_{\max}$  should be set by the lowest signal-to-noise ratio that the instrument can tolerate. A practical value of  $T_{\max}$  could, for example, be chosen at the temperature where the fluorescence intensity is reduced to 1% of its maximum value. In addition, the highest temperature which the luminescent material can withstand, without change in the temperature dependence of its fluorescence, should also be considered in the determination of the upper limit mentioned above. This is normally much higher for doped thermometric crystal materials than for doped glasses (e.g. a study of  $\text{Nd}^{3+}$  doped materials, by Grattan *et al*<sup>[55]</sup>) due to permanent thermal decomposition.

## 2.3. Temperature dependence of Cr<sup>3+</sup> fluorescence in high field crystals

In a high strength crystal field ( $Dq/B \gg 2.3$ ), the lowest excited state of Cr<sup>3+</sup> is  ${}^2E$ . At low temperatures, the Cr<sup>3+</sup> luminescence is dominated by  ${}^2E \rightarrow {}^4A_2$  transitions so that long fluorescence lifetimes are observed, e.g.  $\sim 1.5$ ms at 100K for alexandrite<sup>[51]</sup> and  $\sim 3.5$ ms at 300K for ruby. With increasing temperature, a higher percentage of the excited Cr<sup>3+</sup> ions will populate the short lifetime  ${}^4T_2$  state and consequently, more  ${}^4T_2 \rightarrow {}^4A_2$  transitions will be initiated, which results in a decrease of the fluorescence lifetimes. Thus, at lower temperatures, the temperature dependence of the Cr<sup>3+</sup> fluorescence lifetimes is dominated by the thermally activated repopulation between the excited  ${}^2E$  and  ${}^4T_2$  states. At even higher temperatures, a higher level of nonradiative transitions appear which will significantly speed up the decrease in the fluorescence lifetimes. In this section, a discussion of a two-level model is undertaken, describing the temperature dependence of the fluorescence lifetimes due to the thermally activated repopulation between the  ${}^2E$  and  ${}^4T_2$  states at lower temperatures. This is developed to take account of both the thermally activated repopulation mentioned above and the nonradiative process, where a single configurational coordinate model with two excited levels is discussed for the temperature dependence over the whole region studied.

### 2.3.1. Two level model for the Cr<sup>3+</sup> fluorescence in high fields

At lower temperatures, where the nonradiative transitions of the excited Cr<sup>3+</sup> ions back to the ground state are negligible, the temperature dependence of the Cr<sup>3+</sup> fluorescence in high crystal fields can adequately be described by a two level model, which has been used by Walling *et al*<sup>[51]</sup> in the case of alexandrite (BeAl<sub>2</sub>O<sub>4</sub>:Cr<sup>3+</sup>) laser action, as shown in Figure 2.5. Due to the long lifetime of the  ${}^2E$  state, at elevated temperatures, most radiative transitions will initiate from the  ${}^4T_2$  state and the  ${}^2E$  functions more as a store of the excited ions; thus it is termed here the 'storage level'. The assumption that the  ${}^4T_2$  and  ${}^2E$  are in 'quasi-thermodynamic equilibrium' with one another can be made, and this is verified for ruby and alexandrite where the upper limits of the nonradiative relaxation times for the  ${}^4T_2 \rightarrow {}^2E$  transition are 7 ps for ruby and 27 ps for alexandrite respectively<sup>[56, 57]</sup>. Thus by taking account of the degeneracies of the  ${}^4T_2$  and  ${}^2E$  states, a mathematical

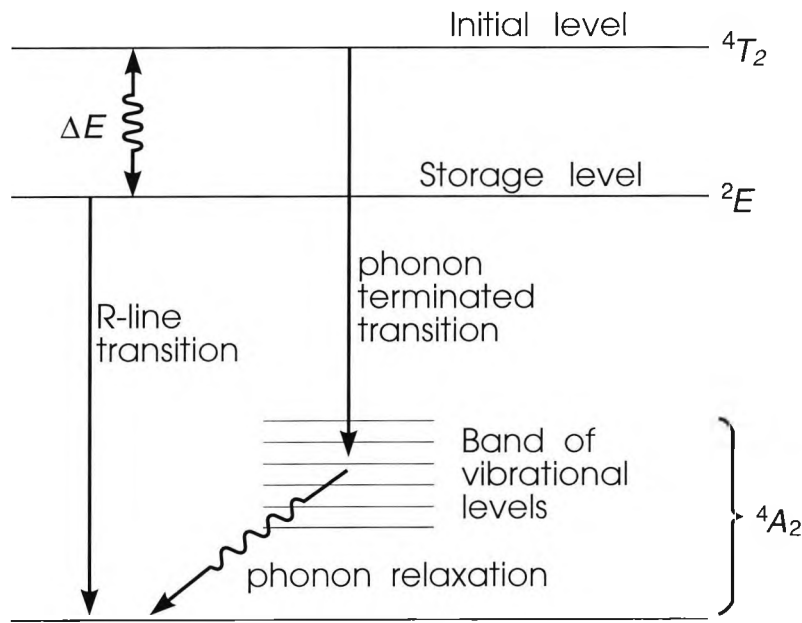


**Figure 2.5:** The 2 level model for  $\text{Cr}^{3+}$  fluorescence in high field crystals.

expression for the fluorescence lifetimes as a function of temperature can be deduced from the two-level model as the following:

$$\tau = \tau_s \cdot \frac{1 + C_d \cdot e^{-\Delta E/kT}}{1 + C_d \cdot (\tau_s / \tau_i) e^{-\Delta E/kT}} = \tau_s \cdot \frac{1 + 3e^{-\Delta E/kT}}{1 + \alpha e^{-\Delta E/kT}} \quad (2-6)$$

where  $\tau$  is the fluorescence lifetime;  $\Delta E$ , the energy gap between the  $4T_2$  and  $2E$  states as defined in Eq.(2-1);  $\tau_i$ ,  $\tau_s$ , the lifetimes of the  $4T_2$  and  $2E$  states; and  $C_d$ , the ratio of the degeneracy of  $4T_2$  to that of  $2E$ , with a value of 3;  $\alpha = C_d \cdot (\tau_s / \tau_i)$ .

The temperature dependences of alexandrite fluorescence are depicted in Figure 2.6, where the open triangles represent the fluorescence lifetime data from Walling *et al*<sup>[51]</sup> over the region 4-500K and the solid circles the data over the 290-940K region obtained by the author, as described in a related work<sup>[49]</sup>. The solid line is the least squares fit of Eq.(2-6) to the fluorescence lifetime data obtained in that work, ranging from 290K to 680K. It shows that the Eq.(2-6) fits to the fluorescence lifetime data quite well over the region 200K-700K. The fitted values of the parameters in Eq.(2-6), are listed in Table 2.2. According to the spectroscopic data obtained by Suchocki *et al*<sup>[58]</sup>, the energy difference

between the lowest members of the  ${}^4T_2$  and  ${}^2E$  states is  $807.5\text{ cm}^{-1}$  at 12 K. The fitted value of  $\Delta E$  is rather close to this spectroscopic value. The value of  $\tau_s$  was measured by Walling *et al*<sup>[51]</sup> to be 1.32 ms at 4 K (for the mirror site). Though based on data beyond a temperature of 290 K, the observed value of  $\tau_s$  fits the above value quite well. In earlier work<sup>[59]</sup>,  $\Delta E$  and  $\tau_s$  were fitted to be  $\sim 750\text{ cm}^{-1}$  and 2.52 ms, where the difference between the  ${}^4T_2$  and  ${}^2E$  states in degeneracies was neglected, that is, the value of  $C_d$  in Eq.(2-6) was taken as 1. Here, based on the same data, a much closer fitting is achieved by taking account of the degeneracy difference.

As shown in Figure 2.6, there are two temperature regions where the discrepancy between the fluorescence lifetime data and the fitted curve is quite significant. One is from 4 K to  $\sim 200$  K over which the discrepancy is due to the rise in lifetime with increasing temperature between 4 and 70 K caused by thermal excitation in excited ions from the lower  ${}^2E$  to the longer lifetime upper  ${}^2E$  level<sup>[51]</sup>. Over this region, the relationship between the fluorescence lifetime and the temperature is not monotonic, so it has little

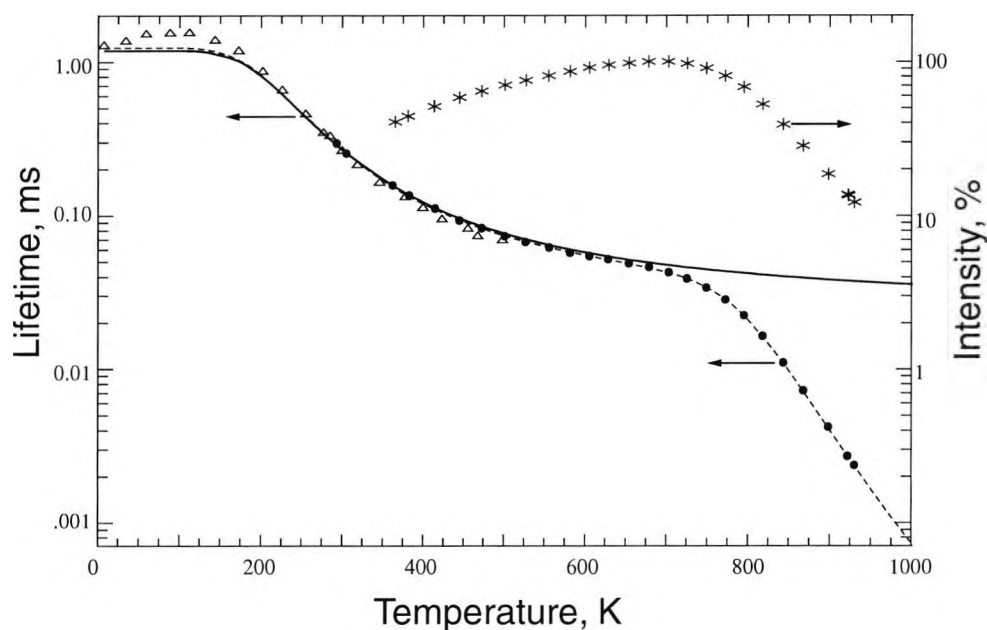


**Figure 2.6:** Temperature dependence of the alexandrite fluorescence. ●●●: the fluorescence lifetime data taken in this work. **Solid line:** the least squares curve of the two-level model [Eq.(2-6)] fitted to the lifetime data over the region 290 - 680 K. **Dashed line:** the least squares curve of the configurational coordinate model [Eq.(2-10)] fitted to the lifetime data over the region 300 - 930 K.  $\Delta\Delta\Delta$ : the lifetime data from Walling *et al*<sup>[51]</sup>. \* \* \*: data for the fluorescence intensity at the broadband vibronic emission ( $>\sim 690\text{ nm}$ ) induced by a 662 nm diode laser.

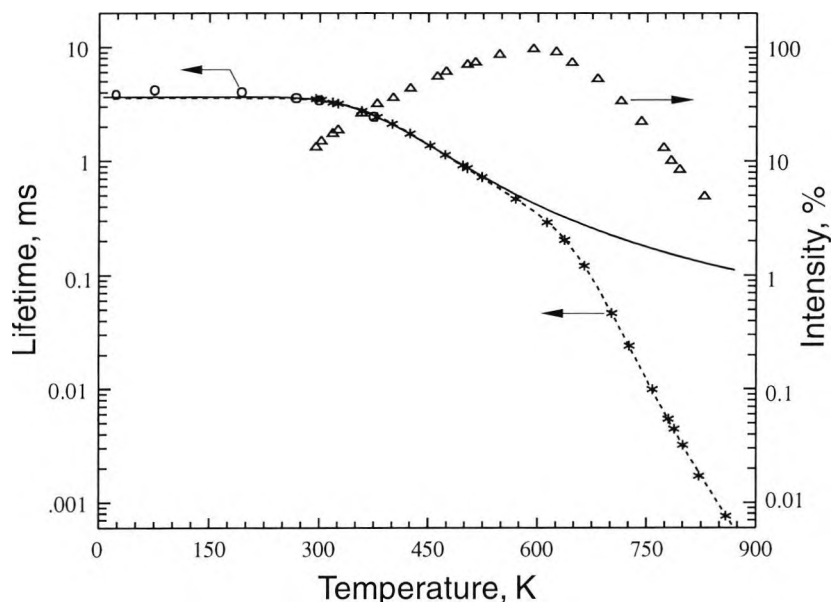


**Figure 2.7:** Temperature dependence of the ruby fluorescence. \*\*\*: the fluorescence lifetime data where a He-Ne laser (633nm) is used as the excitation source. **Solid line:** the least squares curve of the two-level model [Eq.(2-6)] fitted to the lifetime data over the region 300 - 475 K. **Dashed line:** the least squares curve of the configurational coordinate model [Eq.(2-10)] fitted to the lifetime data over the region 300 - 800 K.  $\Delta\Delta\Delta$ : data for the fluorescence intensity at the broadband vibronic emission ( $>\sim 695$  nm) induced by the He-Ne laser. o o o: the lifetime data from Nelson *et al* [60].

thermometric use. For the same reason, such a region also exists in the case of ruby, as shown in Figure 2.7 from 20 K to  $\sim 275$  K, where the solid line represents the least squares curve of Eq.(2-6) fitted to the lifetime data ranging from 300 K to 570 K.

The other region over which the fluorescence lifetime decreases sharply with increasing temperature is beyond  $\sim 700$  K. The decrease in the fluorescence intensity over the broad band emission with increasing temperature beyond this temperature, as shown in Figure 2.6, reveals that the discrepancy of the two-level model with the experimental data over this region is due to the nonradiative transitions which are becoming stronger with increasing temperature beyond  $\sim 700$  K. Again the same phenomenon can be observed in ruby at a lower temperature (beyond  $\sim 600$  K), as illustrated in Figure 2.7. The nonradiative transitions accelerate the decrease in the fluorescence lifetime with increasing temperature, and make the fluorescence lifetime much more sensitive to temperature variance at high temperatures. Therefore, it is of particular thermometric interest to take an account of the nonradiative transitions in the model of the  $\text{Cr}^{3+}$  fluorescence in high field materials, as is discussed in the following section.

### 2.3.2. The configurational coordinate model for the Cr<sup>3+</sup> fluorescence in high fields

To include the effect of the nonradiative transitions, a single configurational coordinate model, redrawn in Figure 2.8, has been used by the author and co-workers [59], in the case of alexandrite. According to this model, the change of the total population of the <sup>4</sup>T<sub>2</sub> and <sup>2</sup>E states, *n* is described by the rate equation,

$$\frac{dn}{dt} = - (1/\tau_s) n_s - [1/\tau_i + (1/\tau_q) e^{-\Delta E_q/kT}] n_i \quad (2-7)$$

where *n<sub>s</sub>*, *n<sub>i</sub>* are the populations of <sup>2</sup>E and <sup>4</sup>T<sub>2</sub> respectively; 1/τ<sub>s</sub>, 1/τ<sub>i</sub> and 1/τ<sub>q</sub>, ΔE<sub>q</sub> are as defined in Eq.(2-6). On the assumption that the <sup>4</sup>T<sub>2</sub> and <sup>2</sup>E states are in 'quasi-thermodynamic equilibrium' with one another, that is,

$$\frac{n_i}{n_s} = C_d e^{-\Delta E/kT} \quad (2-8)$$

where C<sub>d</sub> = 3, as defined in Eq.(2-6), the rate equation may be rewritten as:

$$\frac{dn}{dt} = - \frac{1/\tau_s + (3/\tau_i) e^{-\Delta E/kT} + (3/\tau_q) e^{-(\Delta E_q + \Delta E)/kT}}{1 + 3 e^{-\Delta E/kT}} n \quad (2-9)$$

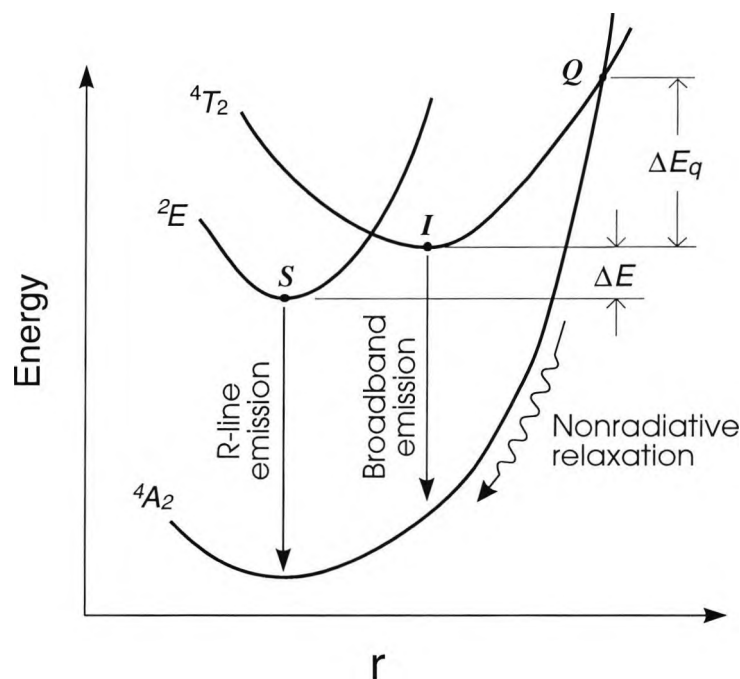


**Figure 2.8:** The single configurational coordinate model for Cr<sup>3+</sup> fluorescence in high field crystals. *r*: the configurational coordinate.

Therefore the fluorescence lifetime,  $\tau$  is given by:

$$\tau = \tau_s \frac{1 + 3 e^{-\Delta E/kT}}{1 + \alpha e^{-\Delta E/kT} + \beta e^{-(\Delta E_q + \Delta E)/kT}} \quad (2-10)$$

where  $\alpha = 3\tau_s/\tau_i$ ;  $\beta = 3\tau_s/\tau_q$ . The dashed line in Figure 2.6 is the least squares fitting of Eq (2-10) to the lifetime data from 290 K to 930 K for alexandrite. The fitted values for  $\Delta E$ ,  $\tau_s$  and  $\ln\alpha$  are listed in Table 2.2 by comparison to those fitted using the two level model, and the values for  $\Delta E_q$  and  $\ln\beta$  resulting are  $10,807 \text{ cm}^{-1}$  and 24.8 respectively. In this approximation, the samples used are separated by a temperature interval of  $\sim 20 \text{ K}$ . The standard deviation of the relative fitting errors of the lifetimes is  $\sim 0.3 \%$ . Eq (2-10) has also been applied to fit the lifetime data of ruby presented in Figure 2.7 from 300 K to 800 K. The fitted curve is depicted as the dashed line in the same figure. The deviation of the curve fitting is  $\sim 1\%$ .

**Table 2.2:** Empirical values of the parameters in appropriate models, fitted to the alexandrite fluorescence lifetime data.

	$\Delta E, \text{cm}^{-1}$	$\tau_s, \text{ms}$	$\ln\alpha$
Spectroscopic data	807.5 <sup>a</sup>	1.32 <sup>b</sup>	—
Two-level model (290 - 650 K)	857.0	1.17	5.40
Configurational coordinate model (290 - 930 K)	851.7	1.23	5.44

a. Suchocki *et al* [58], b. Walling *et al* [51].

### 2.3.3. Other contributions to temperature dependence at low temperatures

At sufficiently low temperatures, e.g.  $T < \Delta E/(k \ln\alpha)$  (that is  $T < 400 \text{ K}$  for ruby and  $T < 200 \text{ K}$  for alexandrite), contributions other than those from the thermalisation between the  $^4T_2$  and  $^2E$  states will have a significant effect upon the temperature dependence of the  $\text{Cr}^{3+}$  fluorescence lifetime in a high strength field, as will be shown in the case of ruby. The illustration of the temperature dependence of ruby fluorescence lifetime presented in Figure 2.7, is magnified at low temperatures in Figure 2.9. The solid line is the least squares fit of the two level model, expressed in Eq.(2-6), to the fluorescence lifetime data ranging

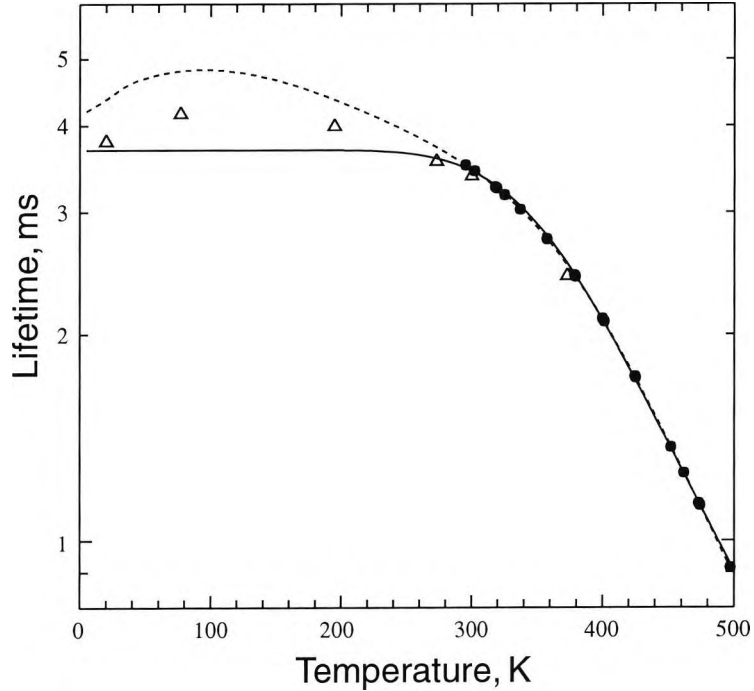


**Figure 2.9:** Temperature dependence of ruby fluorescence lifetime at low temperatures.

**Table 2.3:** Empirical values of the parameters in appropriate models, fitted to the ruby fluorescence lifetime data ranging from 300 to 500 K.

	$\Delta E, \text{cm}^{-1}$	$\tau_s, \text{ms}$	$\ln\alpha$	$\sigma_n, \%$
Spectroscopic data <sup>a</sup>	2350	—	—	—
Two-level model	1957	3.69	6.76	0.77
Modified two level model	2351	4.2	8.53	0.14

a. Data from Fonger and Struck <sup>[521]</sup>.

from ~300 K to 500 K, denoted by the solid circles. The corresponding fitted values of the parameters in Eq.(2-6) are listed in Table 2.3. The fitted value of  $\Delta E$  differs from the spectroscopic value,  $2350 \text{ cm}^{-1}$ , by ~17 %. Due to the size of this discrepancy, it would be expected that other mechanisms are involved in the determination of the temperature dependence. Also the increase in the fluorescence lifetime with increasing temperature at even lower temperatures,  $T < \sim 100 \text{ K}$  as observed in ruby and alexandrite, could not be interpreted in a satisfactory way by the two level model.

As clearly identified by Fonger and Struck<sup>[52]</sup> from the phonon sidebands of the ruby  ${}^2E \rightarrow {}^4A_2$  emission at 77 K, there are two prominent phonon energies given by:

$$h\nu_1 = 430 \text{ cm}^{-1}, \quad h\nu_2 = 280 \text{ cm}^{-1} \quad (2-11)$$

The ratio of the peak intensity of the sidebands corresponding to these two phonon energies,  $I(h\nu_1)/I(h\nu_2)$  is  $\sim 0.65$ . The contribution of the phonon-induced transitions to the temperature dependence results in an increase in emission probability by a factor of  $\coth(h\nu/2kT)$ .

In addition, the  ${}^2E$  state is further split into  $\bar{E}$  and  $2\bar{A}$  states by a tiny energy gap of  $\Delta E_R = 29.1 \text{ cm}^{-1}$  in ruby, which results in two sharp  $R$ -line emissions,  $R_1$  ( $693.4\text{nm}$ ,  $\bar{E} \rightarrow {}^4A_2$ ) and  $R_2$  ( $692\text{nm}$ ,  $2\bar{A} \rightarrow {}^4A_2$ ), familiar in the ruby laser. At temperatures close to  $\Delta E_R/k$  or below, the thermalisation between the  $\bar{E}$  and  $2\bar{A}$  states will dominate the temperature dependence of the fluorescence lifetime. Due to the longer radiative lifetime of the high lying  $2\bar{A}$  state, this gives rise to the increase in fluorescence lifetime with increasing temperature over certain parts of the "cryogenic region," as demonstrated by the temperature dependences of the alexandrite and ruby fluorescence lifetimes below 100 K. It has been verified by the work of Weinstein<sup>[61]</sup> that such thermalisation in ruby can be adequately described by simple Boltzman statistics over the region 0 - 100 K as:

$$I_{R2} / I_{R1} = \alpha_R \cdot e^{-\Delta E_R/kT} \quad (2-12)$$

where  $I_{R1}$ ,  $I_{R2}$  are intensities of  $R_1$  and  $R_2$  emission respectively; and the ratio  $\alpha_R$  is found to be:

$$\alpha_R = 0.65. \quad (2-13)$$

Therefore, to describe closely the overall temperature dependence of the  $\text{Cr}^{3+}$  fluorescence lifetime at low temperatures, the two level model expressed by Eq.(2-6) has to be modified to take account of the phonon-induced transitions and the splitting of the  ${}^2E$  state. Thus, in the case of ruby, by assuming that the  $R$ -line phonon sidebands induced by  $h\nu_1$  and  $h\nu_2$  originate from the  $R_1$  and  $R_2$  emission respectively, the two level model may be modified according to the following expression:

$$\tau = \tau_s \frac{1 + e^{-\Delta E_R/kT} + 6 \cdot e^{-\Delta E/kT}}{\coth(h\nu_1/2kT) + \alpha_R \coth(h\nu_2/2kT) \cdot e^{-\Delta E_R/kT} + \alpha \cdot e^{-\Delta E/kT}} \quad (2-14)$$

where  $\Delta E_R = 29.1 \text{ cm}^{-1}$ ; the values of  $h\nu_1$ ,  $h\nu_2$  and  $\alpha_R$  are given in Eqs.(2-11) and (2-13) respectively. The values of  $\Delta E$ ,  $\tau_s$  and  $\ln\alpha$  obtained by a least squares fit to the ruby fluorescence lifetime data ranging from  $\sim 300 \text{ K}$  to  $500 \text{ K}$ , are listed in Table 2.3. Not only does this modified model fit the lifetime data much better, with a standard deviation of 0.14 %, compared with that of 0.77 % achieved by the previous model, but also the value of  $\Delta E$  resulting from the using of this model agrees with the spectroscopic data quite well, as shown in Table 2.3.

## 2.4. Discussion

The temperature dependence of the  $\text{Cr}^{3+}$  fluorescence is strongly characterised by the crystal field strength. Further, the observation of the variation of the fluorescence lifetime with temperature can indicate whether the field strength of the host material is high or low. In a host with a low crystal field, the decrease in the  $\text{Cr}^{3+}$  fluorescence lifetime with increasing temperature changes rapidly only over one continuous temperature region, as is observed in the cases of LiSAF, LiBAF and LiCAF and shown in Figure 2.10. However, in a high field host, two such regions are found. For instance, in alexandrite, such regions range from  $\sim 150 \text{ K}$  to  $\sim 300 \text{ K}$  and from  $\sim 700 \text{ K}$  and beyond; in ruby, from  $\sim 300 \text{ K}$  to  $\sim 500 \text{ K}$  and from  $\sim 600 \text{ K}$  and beyond; and in emerald, from  $\sim 75$  to  $\sim 600 \text{ K}$  and from  $\sim 650 \text{ K}$  and beyond as shown in Figure 2.10.

Two configurational coordinate models, presented in Figure 2.3 and Figure 2.8 are sufficient to allow the interpretation of the temperature dependences of the  $\text{Cr}^{3+}$  fluorescence in crystal materials qualitatively, even quantitatively to an extent of sufficient precision for thermometric applications, as shown in the cases of Cr:LiSAF, alexandrite and ruby. In high field strength host crystals, two mechanisms, the thermal repopulation of the  ${}^4T_2$  and  ${}^2E$  states and the nonradiative process dominate the temperature dependence alternately over different temperature regions. Thus the fluorescence lifetimes are quite sensitive to temperature variances over a wide temperature region, and are suitable for wide range thermometric uses. In addition, the total fluorescence efficiency does not decrease

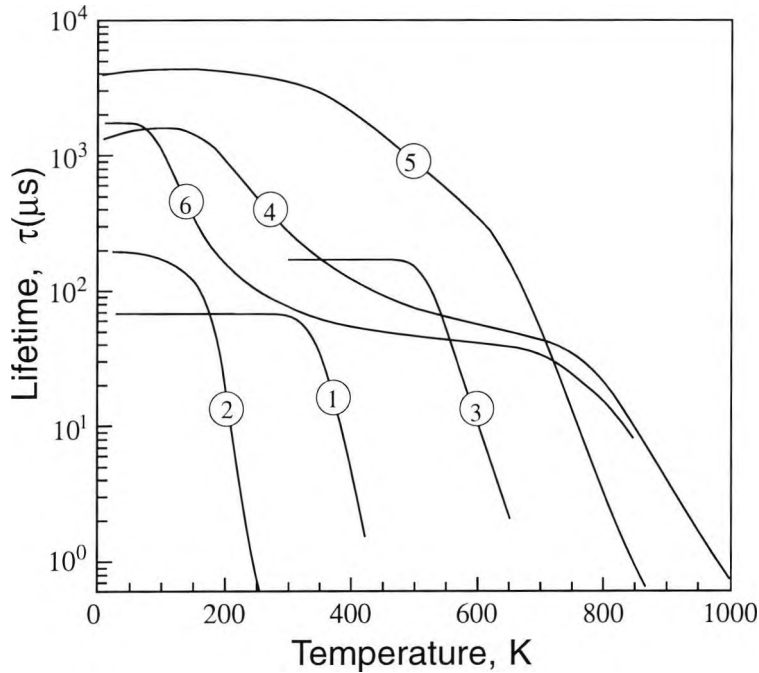


**Figure 2.10:** Temperature dependences of Cr<sup>3+</sup> fluorescence lifetime in various host materials. Materials with low strength of crystal field: **1.** LiSAF; **2.** LiBAF<sup>[54]</sup>; **3.** LiCAF<sup>[54]</sup>. Materials with high strength of crystal field: **4.** alexandrite<sup>[51, 59]</sup>; **5.** ruby (data from ~20 to 300 K obtained from Nelson *et al*<sup>[60]</sup>, those from 300 K and beyond by the author); **6.** emerald<sup>[52]</sup>.

with increasing temperature over the region where the thermal repopulation of the  $^4T_2$  and  $^2E$  states dominates, and an increase in absorption of the excitation light is observed, as in alexandrite<sup>[59]</sup>. These features are of significant advantage in achieving an acceptable signal-to-noise ratio in the corresponding optical thermometers. In low field crystals, only the nonradiative process dominates the temperature dependence, and the fluorescence intensity decreases with temperature increase, as with the lifetime. Therefore the measurement range of the corresponding lifetime based thermometer is rather limited, though high measurement resolution could be achieved.

By contrast, in Cr<sup>3+</sup> doped low field crystals, partly due to the lower degree of overlapping between the absorption and emission spectra, compared with that in high field crystals, the self-trapping of fluorescence is rather weak. In some low field crystals, the dependence of the fluorescence lifetime on the Cr<sup>3+</sup> concentration is rather slight even up to very high concentrations, e.g. from 2 % to 15 % for Cr:LiSAF<sup>[62]</sup> and from 1 % to 10 % for Cr:LiBAF<sup>[54]</sup>. These properties indicate that slight changes in the Cr<sup>3+</sup> concentration of the samples used in the thermometers, the size and the positioning of the sample

materials in the formation of the temperature probes, will have no significant effect on the measurements. As the result, the measurement reproducibility and the exchangeability of the temperature probes made of low field sensing materials could be better than those in the case of using high field materials, especially when probes are made by using the sensing materials which are of the same kind but are from different batches of crystal production.

## 2.5. Impact on subsequent experimental work

The purpose of the discussion of this Chapter is to explore the reason for the temperature dependence of the  $\text{Cr}^{3+}$  fluorescence lifetimes. It shows that the temperature dependence is intrinsic to the properties of a fluorescent material. Thus, such a temperature dependence is reproducible from fluorescent material to material, and can be of thermometric use. This lays the basis of the fluorescence thermometry discussed subsequently.

The work discussed here is, perhaps, the first published attempt which has been made to look into the mechanism of the temperature dependence of  $\text{Cr}^{3+}$  fluorescence lifetime for the purpose of thermometric applications. The proposed models for this temperature dependence are strongly application-oriented. They could be used to predict the temperature dependence of the  $\text{Cr}^{3+}$  fluorescence lifetime in a host material and hence to assist the selection of suitable material for thermometric application over a specific temperature region. They also could be used as empirical calibration formulae in the assessment of various  $\text{Cr}^{3+}$  fluorescence lifetime-based thermometers. These will be illustrated in various experimental works presented in Chapter 4, after the description, in Chapter 3, of a new category of effective signal processing techniques used in this thesis work for the detection of fluorescence lifetimes.

# Phase-Locked Detection of Fluorescence Lifetime

---

### 3.0. Abstract

A new category of signal processing schemes for the detection of fluorescence lifetime is discussed. These schemes are developed independently in this thesis work for applications in a number of inexpensive, compact and reliable fluorescence lifetime-based fibre optic thermometers. With phase-sensitive detectors being used to achieve a high noise-suppression ability, the schemes include some of the features of existing phase and modulation techniques for lifetime measurement. However, they differ from them in several aspects, especially in that they operate in a way rather similar to that of a phase-locked loop. Based on such schemes, the measured lifetime is converted to a repetitive signal whose period is directly proportional to it, and thus a high measurement resolution can be achieved. Such schemes can be operated over a wide consecutive measurement range of fluorescence lifetime, and they are particularly useful for temperature sensor applications using long lifetime ( $>1\mu\text{s}$ ) fluorescent media, such as the  $\text{Cr}^{3+}$  doped materials discussed in the previous Chapter. Illustrations of the applications of these schemes in lifetime-based fibre optic thermometers are to be presented in the following Chapters.

### 3.1. Introduction

Apart from the searching for better sensing materials, progress of fluorescence thermometry is often accompanied with the introduction of new signal processing techniques for the measurement of fluorescence lifetimes. This is illustrated by the diversity in the lifetime measurement techniques employed in various existing fluorescence thermometer schemes reviewed in Chapter 1. In fact, the various existing schemes are, quite often distinguished by the signal processing techniques employed, instead of the sensing materials used<sup>[42]</sup>. These reflect the importance of the achievement of an inexpensive, simple and versatile signal processing technique, in the commercialisation of the fluorescence thermometry.

In this thesis work, a whole category of new signal processing approaches, termed here the Phase-Locked Detection of fluorescence lifetime (PLD), has been independently developed and successfully applied to several fibre-optic thermometer schemes<sup>[30, 38, 47, 49, 63]</sup>, though as mentioned in Chapter 1, some primitive form of this category of schemes could be found in the work of Bosselmann *et al*<sup>[46, 20]</sup>. These schemes stem from the existing phase and modulation techniques<sup>[64]</sup>, but they differ from them in several important aspects. In particular, they operate in a way rather similar to that of a phase-locked loop, so that the measured lifetime is converted to a repetitive output signal which also serves as the modulation signal, and whose period is directly proportional the measured lifetime itself. Therefore the measurement can be made by determining the period of this repetitive output. This allows a high resolution to be achieved over a wide range of lifetimes. The operating mechanism and some important design considerations of a variety of Phase-Locked Detection (PLD) techniques are covered in this Chapter with theoretical analysis. The applications of these techniques in a number of fluorescence thermometer schemes will be given in the following Chapters.

### 3.2. From lock-in to phase-locked detection

The motivation for introducing the PLD schemes is seen in a simple analysis of the measurement error of a two-phase lock-in system used for fluorescence lifetime measurement. An illustration of such a system is presented in Figure 3.1. If the intensity of the excitation light is modulated by  $v_m$ , a sinusoidal signal, the DC-decoupled fluorescence response signal,  $v_f$  is given as:

$$v_f = V_A \sin(\omega t - \varphi), \quad (3-1)$$

and  $\varphi$ , its phase lag with respect to  $v_m$  is given by:

$$\tan \varphi = \omega \tau \quad (3-2)$$

where  $\omega$  is the radian frequency of the modulation signal;  $\tau$ , the fluorescence lifetime;  $V_A$ , the amplitude of fluorescence response signal and  $t$  the elapsed-time. Therefore the measurement of the fluorescence lifetime,  $\tau$  can be calculated from  $y_i, y_q$ , the outputs of the in-phase and quadrature PSDs (Phase Sensitive Detectors) shown in Figure 3.1 respectively, by the following formula:

$$\tau = \frac{\tan \varphi}{\omega} = \left(-\frac{y_q}{y_i}\right) \cdot \frac{1}{\omega} \quad (3-3)$$

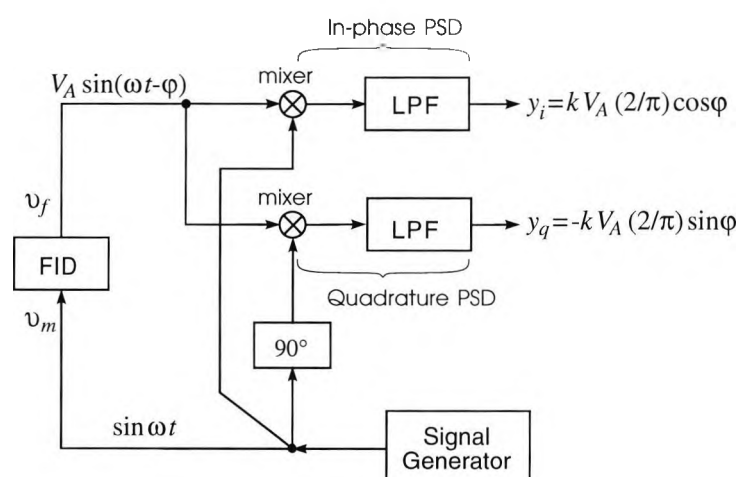


**Figure 3.1:** A two-phase lock-in system. FID: the fluorescence inducing and detecting devices. Mixer: switch type, double balanced demodulator. LPF: low pass filter. PSD: phase sensitive detector.

Thus, the standard deviation of the relative measurement error of the system maybe estimated to be:

$$\sigma_{\Delta\tau/\tau} = \left( \frac{\sigma_{y_i}^2}{y_i^2} + \frac{\sigma_{y_q}^2}{y_q^2} + \frac{\sigma_{\omega}^2}{\omega^2} \right)^{1/2} \approx \left( \frac{\sigma_{y_i}^2}{y_i^2} + \frac{\sigma_{y_q}^2}{y_q^2} \right)^{1/2} \quad (3-4)$$

where  $\sigma_{y_i}$ ,  $\sigma_{y_q}$  and  $\sigma_{\omega}$  are standard deviations of  $y_i$ ,  $y_q$  and  $\omega$  respectively; and the approximation is made that  $(\sigma_{\omega}/\omega)^2$  is negligible as compared with the other two terms in most application situations.

For a well balanced two-phase system, it may be assumed that,

$$\sigma_{y_i} = \sigma_{y_q} = \sigma_y \quad (3-5)$$

Then,

$$\begin{aligned} \sigma_{\Delta\tau/\tau} &= \sigma_y \left( y_q^{-2} + y_i^{-2} \right)^{1/2} \\ &= \frac{\sigma_y}{kV_A} \left( \cos^{-2}\varphi + \sin^{-2}\varphi \right)^{1/2} = \frac{\sigma_y}{kV_A} \frac{1 + \tan^2\varphi}{\tan\varphi} \end{aligned} \quad (3-6)$$

where  $k$  is the gain of the PSDs. In fact,  $V_A$ , the amplitude of the fluorescence response signal does also depend on  $\varphi$ , which as expressed in Eq.(3-2) is a function of the modulation frequency and the fluorescence lifetime: that is, it is given by:

$$V_A = \frac{V_{A0}}{[1 + (\omega\tau)^2]^{1/2}} = \frac{V_{A0}}{[1 + \tan^2\varphi]^{1/2}}, \quad (3-7)$$

where  $V_{A0}$  is a constant independent of  $\varphi$ . As a result,

$$\sigma_{\Delta\tau/\tau} = \frac{\sigma_y}{kV_{A0}} z(\varphi), \quad (3-8)$$

and

$$z(\varphi) = \frac{(1 + \tan^2\varphi)^{3/2}}{\tan\varphi} \quad (3-9)$$

where  $z(\varphi)$  is depicted as a function of  $\varphi$  in Figure 3.2. It can be shown that the minimum value of  $z$  occurs at a corresponding value of phase lag,  $\varphi_{opt}$  where

$$\varphi_{\text{opt}} = \arctan (1/\sqrt{2}) \approx 35.3^\circ \quad (3-10)$$

Therefore in order to minimise  $\sigma_{\Delta\tau/\tau}$ , the measurement should be made under the condition that  $\varphi$ , the phase shift of the fluorescence response is as close to  $\varphi_{\text{opt}}$  as possible. This can be achieved by letting the modulation frequency,  $\omega$  automatically vary with the measured lifetime according to the following equation:

$$\omega = \frac{\tan\varphi_{\text{opt}}}{\tau} = \frac{1}{\tau\sqrt{2}} \quad (3-11)$$

By doing so,  $\varphi$ , the phase shift of the fluorescence response is kept constant and it is the modulation frequency,  $\omega$  that follows the change of the measured lifetime  $\tau$ . Consequently the value of  $\tau$  could easily be deduced from the measurement of the modulation frequency or period, a parameter which is easier to measure with high precision and to transfer, e.g. using Eq.(3-11). This is essentially how the PLD category of signal processing schemes operates. The following discussion is of a variety of schemes, in several categories illustrating some main design considerations.

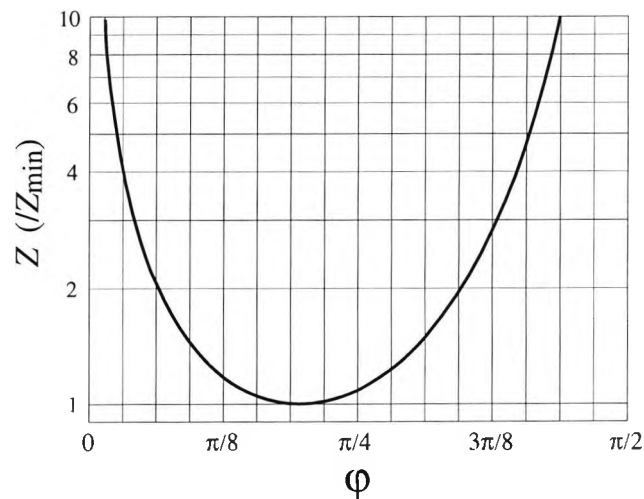


**Figure 3.2:**  $z$  v.s.  $\varphi$  where  $z$  is normalised to its minimum.

### 3.3. PLD with analog modulation of excitation source and single reference signal (PLD-AMSR)

Figure 3.3 is a schematic of a Phase-locked Detection system. The excitation light source is intensity-modulated at a frequency,  $\nu_m$ , a sinusoidal signal generated from a voltage controlled oscillator (VCO). As the result,  $\nu_f$ , the DC-decoupled fluorescence response signal is given by:

$$\nu_f = V_A \sin(\omega t - \varphi) = \frac{V_{A0}}{(1 + \tan^2 \varphi)^{1/2}} \sin(\omega t - \varphi) \quad (3-12)$$

where  $\varphi$  is expressed as in Eq.(3-2). As depicted in Figure 3.3, the reference signal for the Phase Sensitive Detector (PSD),  $\nu_r$  stems from the modulation signal  $\nu_m$  but lags behind it by a phase shift of  $2\pi\alpha$ . So the output of the PSD, designated as  $y$ , is given by the following:

$$y = \frac{2}{\pi} k V_A \cos(2\pi\alpha - \varphi) = \frac{2kV_{A0}}{\pi(1 + \tan^2 \varphi)^{1/2}} \cos(2\pi\alpha - \varphi)$$

$$= \frac{2kV_{A0}}{\pi[1 + (2\pi/x)^2]^{1/2}} \cos[2\pi\alpha - \arctan(2\pi/x)] = f(x, \alpha) \quad (3-13)$$

where  $x$  is the ratio of  $\tilde{T}$ , the period of the modulation signal to the lifetime,  $\tau$ , given by:

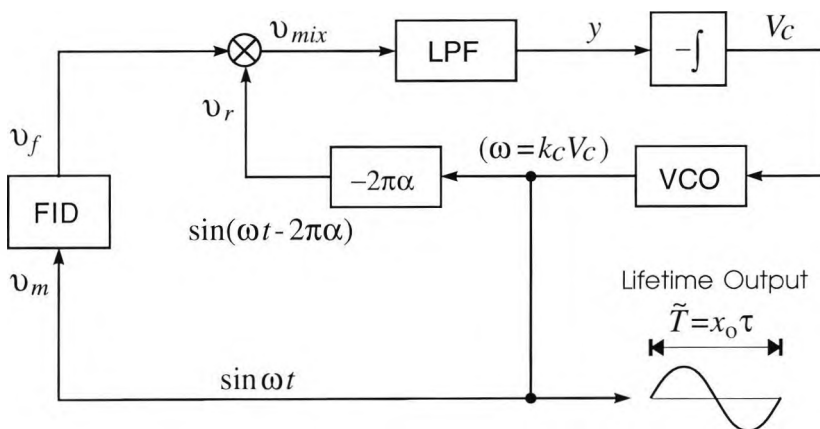


**Figure 3.3:** A PLD-AMSR system. VCO: Voltage Controlled Oscillator.

$$x = T/\tau \quad (3-14)$$

and  $k$  is the gain of the PSD. As shown in Figure 3.3,  $y$  is forwarded to an integrator, and then  $V_c$ , the time integration of  $-y$  is fed back to control  $\omega$ , the radian frequency of the VCO output. It is obvious that  $\omega$  will keep varying unless it can be stabilised to the value  $\omega_0$ , where:

$$\omega_0 = \frac{\tan(2\pi\alpha - \pi/2)}{\tau} \quad (3-15)$$

which results in  $y = 0$ , that is the 'locked' state for a Phase-locked Detection system, and this means keeping the modulation period to lifetime ratio at the value given by:

$$x_0 = x \Big|_{f(x,\alpha)=0} = \frac{2\pi}{\tan(2\pi\alpha - \pi/2)} \quad (3-16)$$

For this system, at the locked state,  $\phi$  is given by:

$$\phi = 2\pi\alpha - \pi/2 \quad (3-17)$$

It can be shown that by choosing  $\alpha$  within the region  $(1/4, 1/2)$  so that  $\pi/2 < 2\pi\alpha < \pi$ , then when  $\omega < \omega_0$ ,  $y < 0$  and  $\omega$  will be increased from the integration of  $-y$ ; and vice versa, when  $\omega > \omega_0$ ,  $y > 0$  and  $\omega$  will be decreased accordingly. That shows that the change of  $\omega$  in the system is always in the direction of approaching  $\omega_0$ , the value given in Eq.(3-15). Consequently, it can be expected that no matter what the initial state is, after a finite period of time, the system will be able to reach the locked state,  $y = 0$ , and keep itself in such a state by letting its modulation frequency trace the change of  $\omega_0$  introduced by the variation of the measured lifetime, as shown in Eq.(3-15). Thereby, the measurement of the fluorescence lifetime can be made from the measurement of the modulation frequency using Eq.(3-15) or its period using the following formula:

$$T = x_0 \tau, \quad (3-18)$$

where  $x_0$  is as expressed in Eq.(3-16), and is referred to as the gain of the lifetime-to-period conversion of the system.

As the measurement is made when the phase difference between the intensity-modulated excitation signal and the fluorescence response signal is being kept constant, as

indicated in Eq.(3-17), the term Phase-Locked Detection of fluorescence lifetime (PLD) is appropriate to describe it. The system presented in Figure 3.3 may be further classified as that using analog modulation and one single reference, which is abbreviated to PLD-AMSR.

### 3.4. PLD with pulse modulation and single reference signal (PLD-PMSR)

The PLD-AMSR scheme shown in Figure 3.3 can be directly adopted to a scheme using a pulse modulated excitation source, called PLD-PMSR, by replacing the sinusoidal output VCO with an ordinary VCO which generates a periodical rectangular pulse with a 50% duty cycle. There are at least two reasons which favour the use of rectangular pulse modulation in the PLD scheme. First, the rectangular pulse can carry more excitation power from the light source than the sinusoidal one, therefore a higher signal-to-noise ratio can be achieved from the corresponding fluorescence response. Secondly, the rectangular pulse modulation of the excitation light source is simpler and much easier to be realised.

An illustration of a PLD-PMSR scheme is depicted in Figure 3.4, and the waveforms of some signals designated in the figure are presented in Figure 3.5. As the excitation source is pulse modulated by a rectangular wave signal, the DC-decoupled fluorescence response,  $v_f$  is given by:

$$v_f = v_f(t) = \begin{cases} V_{A0} - \frac{2V_{A0} \cdot e^{-t/\tau}}{1 + e^{-\tilde{T}/2\tau}}, & 0 \leq t < \tilde{T}/2 \\ -V_{A0} + \frac{2V_{A0} \cdot e^{-(t-\tilde{T}/2)/\tau}}{1 + e^{-\tilde{T}/2\tau}}, & \tilde{T}/2 \leq t < \tilde{T} \end{cases} \quad (3-19)$$

and

$$v_f(t) = -v_f(t + \tilde{T}/2), \quad (3-20)$$

$$v_f(t) = v_f(t + n\tilde{T}), \quad n=1,2,3 \dots \quad (3-21)$$

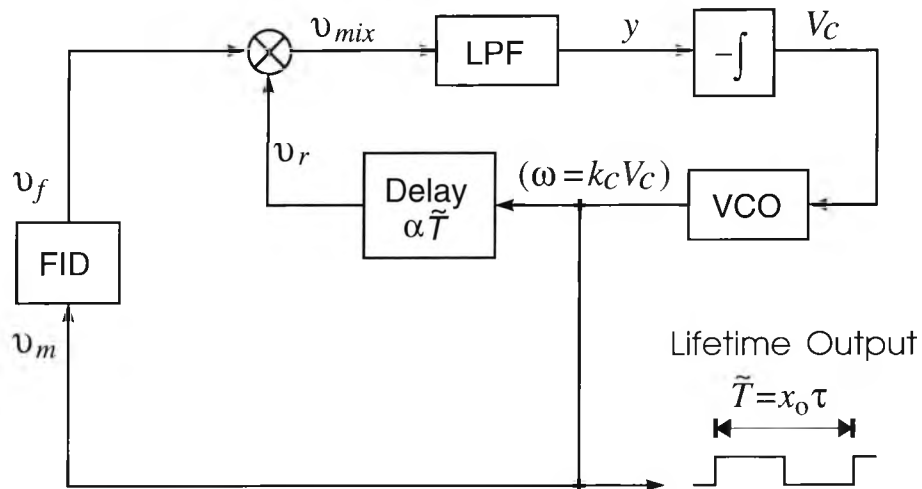


**Figure 3.4:** A PLD-PMSR system. (Components as Figure 3.1)

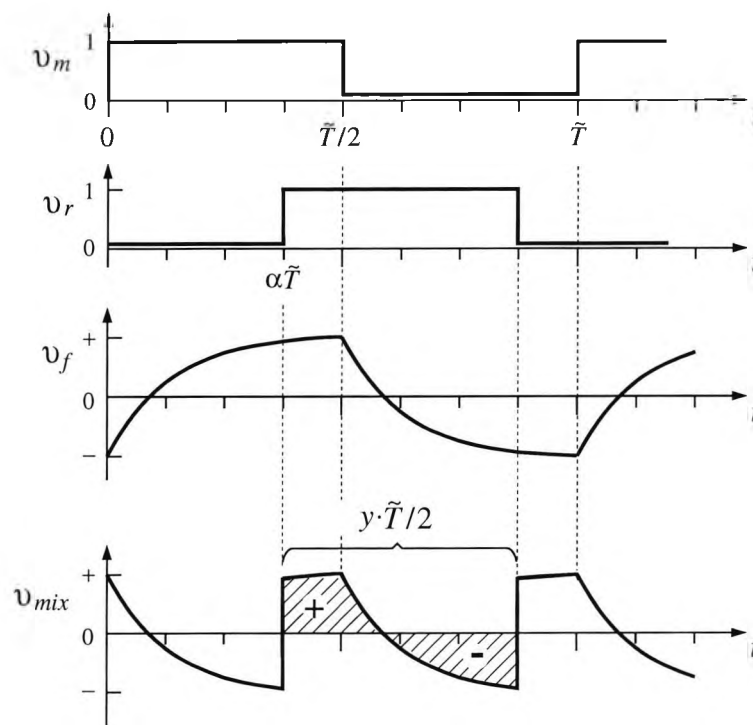


**Figure 3.5:** Waveforms of signals designated in Figure 3.4.

$v_r$ , the reference signal is obtained by delaying the modulation signal  $v_m$  by a time  $\alpha\tilde{T}$ . Thus the output of the PSD may be expressed as:

$$y = \frac{1}{\tilde{T}} \int_0^{\tilde{T}} v_{mix} dt = \frac{1}{\tilde{T}} \left\{ -\int_0^{\alpha\tilde{T}} v_f(t) dt + \int_{\alpha\tilde{T}}^{\alpha\tilde{T} + \tilde{T}/2} v_f(t) dt - \int_{\alpha\tilde{T} + \tilde{T}/2}^{\tilde{T}} v_f(t) dt \right\}$$

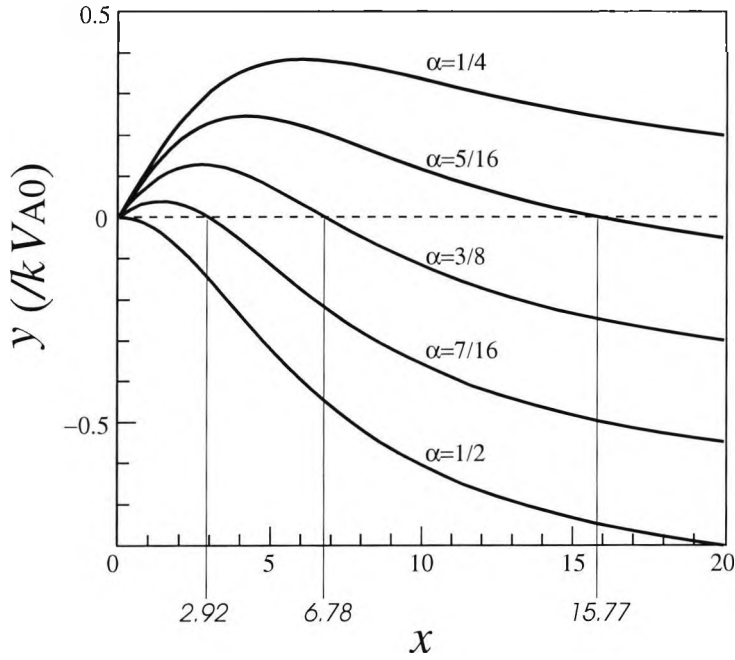


**Figure 3.6:**  $y$  v.s.  $x$  for PLD-PMSR.

$$\begin{aligned}
 &= \frac{2}{T} \int_{\alpha T}^{\alpha T + T/2} v_f(t) dt = k \cdot V_{A0} \left[ 1 - 4\alpha + \frac{4\tau}{T} \left( 1 - \frac{2e^{-\alpha T/\tau}}{1 + e^{-T/2\tau}} \right) \right] \\
 &= k \cdot V_{A0} \left[ 1 - 4\alpha + \frac{4}{x} \left( 1 - \frac{2e^{-\alpha x}}{1 + e^{-x/2}} \right) \right] \\
 &= f(\alpha, x), \quad (1 \leq \alpha \leq 1/2, x > 0) \tag{3-22}
 \end{aligned}$$

where  $x$  as defined in Eq.(3-14).  $y$  is plotted as a function of  $x$  with respect to different values of  $\alpha$  in Figure 3.6, normalised to the product of  $k$  and  $V_{A0}$ .

$x_0$ , the gain of the lifetime-to-period conversion of the system is given by:

$$x_0 = x \Big|_{f(x,\alpha)=0} = f_1(\alpha) \tag{3-23}$$

and is depicted as a function of  $\alpha$  in Figure 3.7 in solid line. It is rather close to that of the PLD-AMSR scheme, presented as a dashed line in the same figure.

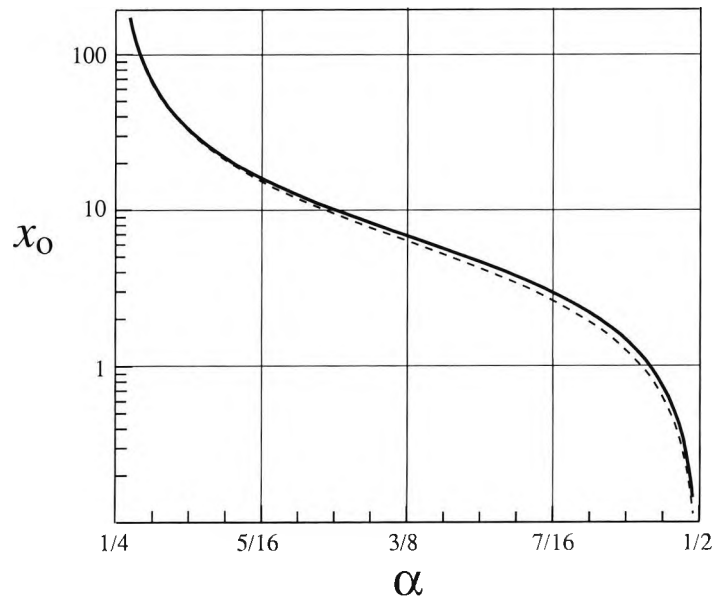


**Figure 3.7:**  $x_0$  v.s.  $\alpha$ . **Solid line:** for PLD-PMSR; **dashed line:** for PLD-AMSR.

### 3.5. The selection of the phase shift ratio, $\alpha$

A PLD system can have a very high noise suppression ability, as with other phase sensitive detection systems. The tracking performance, the way in which the system monitors the measured lifetime, is described by its noise bandwidth and transient response. These are mainly determined by the parameters of the PSD and the VCO used. The configuration of a PLD system bears a distinct resemblance to a linear PLL; thus the existing theory of a linear Phase Locked Loop<sup>[65]</sup> can be adapted to analyse the system, and to select the parameters of the PSD and the VCO to obtain the desired tracking performance.

In designing a PLD system, apart from the consideration of its tracking performance which can be referred to the PLL, the importance of choosing an appropriate value for  $\alpha$ , which sets the phase lag between the modulation and reference signals, is unique to a PLD system. It can have a significant impact on the performance of the system, in particular in aspects of measurement resolution and accuracy, as shown below by the error analysis of the measurement made by the PLD system.

According to Eq.(3-18), the relative error of the measurement made by the PLD system is given by:

$$\frac{\Delta\tau}{\tau} \approx \frac{\Delta\tilde{T}}{\tilde{T}} - \frac{\Delta x_o}{x_o} \quad (3-24)$$

The first term at the right of the equation is the departure of the system output,  $\tilde{T}$  from the expected value,  $x_o\tau$ . As  $\tilde{T}$  is controlled by the PSD output,  $y$ , this term could be expressed as:

$$\frac{\Delta\tilde{T}}{\tilde{T}} \approx \Delta y + \left( \tau \frac{dy}{d\tau} \right)_{y=0} \quad (3-25)$$

where  $\Delta y$  can be regarded as the equivalent *total amplitude noise* of the whole system.

The second term on the right of Eq.(3-24) is the relative variance of the gain of the lifetime-to-period conversion,  $x_o$ . It is caused by  $\Delta\alpha$ , the drift of the phase shift ratio  $\alpha$ , and it can be expressed as:

$$\frac{\Delta x_o}{x_o} \approx \left( \frac{1}{x_o} \frac{dx_o}{d\alpha} \right) \Delta\alpha \quad (3-26)$$

Thus, it can be shown that the standard deviation of the relative measurement expressed in Eq.(3-24) is given as:

$$\sigma_{\Delta\tau/\tau} \approx \left( \frac{\sigma_y^2}{s_y^2} + s_x^2 \sigma_\alpha^2 \right)^{1/2} \quad (3-27)$$

where  $\sigma_y$ ,  $\sigma_\alpha$  are standard deviations of  $y$  and  $\alpha$  respectively; and

$$s_y = \left| \tau \frac{dy}{d\tau} \right|_{y=0} = \left| x \frac{dy}{dx} \right|_{x=x_o} \quad (3-28)$$

and

$$s_x = \left| \frac{1}{x_o} \frac{dx_o}{d\alpha} \right|, \text{ where} \quad (3-29)$$

$s_y$  is the sensitivity of the PSD output to the relative change of the measured lifetime, and  $s_x$ , the relative sensitivity of the gain of the lifetime to period conversion,  $x_0$  to  $\alpha$ .

It is clearly shown in Eq.(3-27), that the measurement error of a PLD system arises primarily from two sources, the *amplitude noise*  $\Delta y$  and the *phase shift drift*  $\Delta\alpha$ . The contributions from these two source are scaled by  $1/s_y$  and  $s_x$  respectively. As will be shown later,  $s_y$  and  $s_x$  are functions of  $\alpha$ . Therefore, in designing a PLD system, the optimal value of  $\alpha$  should be chosen so that the values of  $1/s_y$  and  $s_x$  are as low as possible, in order that the error contributions from both  $\Delta y$  and  $\Delta\alpha$  could be minimised. These two error sources are independent of each other, and, initially, the choice of optimal value of  $\alpha$  will be analysed with respect to  $\Delta y$  and  $\Delta\alpha$  separately, in the following discussions.

Firstly, to minimise the error contribution from the amplitude noise,  $\Delta y$ , the optimal value of  $\alpha$  is that which makes  $s_y$  have be as high a value as possible. For the PLD-AMSR scheme,  $s_y$  is given by:

$$s_y = \frac{2kV_{A0}}{\pi} \cdot \frac{\tan(2\pi\alpha - \pi/2)}{[1 + \tan^2(2\pi\alpha - \pi/2)]^{3/2}}, \quad (3-30)$$

and for the PLD-PMSR scheme,

$$s_y = kV_{A0} \cdot \left| \frac{1 - 4\alpha + \left[ \left(1 - \frac{x_0}{2}\right) \cdot (1 - 4\alpha) - 2 \right] \cdot e^{-x_0/2} + 8\alpha \cdot e^{-\alpha x_0}}{1 + e^{-x_0/2}} \right| \quad (3-31)$$

where  $1/4 < \alpha < 1/2$ .

As shown in Eqs.(3-30) and (3-31), both values of  $s_y$  are functions of  $\alpha$  and are plotted against  $\alpha$  in Figure 3.8 accordingly, with their values normalised to the product of  $k$  and  $V_{A0}$ . As illustrated in Figure 3.8,  $s_y$  can vary rather dramatically with  $\alpha$ . For example, in both cases, at  $\alpha = 7/16$ ,  $s_y$  drops down to nearly a third of its maximum value, which occurs at the value of  $\alpha$  given by:

$$\alpha_{opt} \Big|_{AMSR} = \frac{1}{4} + \frac{\arctan(1/\sqrt{2})}{2\pi}, \approx 0.348 \quad (3-32)$$

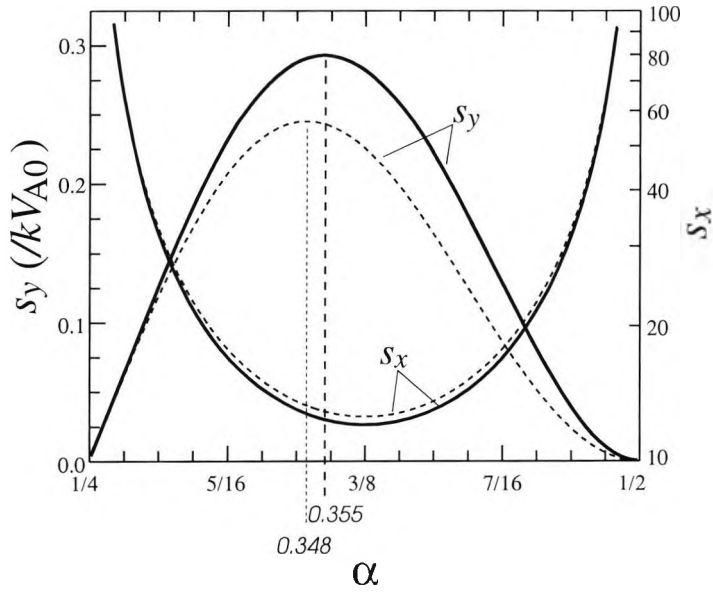


**Figure 3.8:**  $s_y$  &  $s_x$  v.s.  $\alpha$ . **Solid lines:** for PLD-PMSR; **dashed lines:** for PLD-AMSRS.

for PLD-AMSRS, and

$$\alpha_{opt} |_{PMSR} \approx 0.355, \quad (3-33)$$

for PLD-PMSR respectively.

Thus, by considering  $s_y$  only, the optimum values for  $\alpha$  are given in Eqs.(3-32) and (3-33) for the designing of the PLD-AMSRS and PLD-PMSR systems respectively. The maximum value of  $s_y$  for the PLD-PMSR system is about 20% higher than that for the PLD-AMSRS system. It is interesting to note that in the case of PLD-AMSRS, by setting  $\alpha$  to the value given in Eq.(3-32), the measurement of fluorescence lifetime is taken with the phase lag between the excitation and response signals fixed to a value which is the same as the optimum phase shift expressed in Eq. (3-10) for the two-phase lock-in discussed before.

Secondly, to minimise the error contribution from the phase shift drift  $\Delta\alpha$ ,  $s_x$ , the relative sensitivity of the gain of lifetime-to-period conversion to  $\Delta\alpha$ , should be minimised as shown in Eq.(3-27). For the PLD-AMSRS scheme, it is given by:

$$s_x = \left| \frac{1}{x_o} \frac{dx_o}{d\alpha} \right| = \left| \frac{4\pi}{\sin(4\pi\alpha)} \right|, \quad (3-34)$$

and for PLD-PMSR:

$$s_x = \left| \frac{1}{x_0} \frac{dx_0}{d\alpha} \right| = \left| \frac{1}{x_0} \frac{\partial f / \partial \alpha}{\partial f / \partial x_0} \right|_{f(x_0, \alpha)=0}$$

$$= \left| \frac{4(1 + e^{-x_0/2} - 2e^{-\alpha x_0})}{1 - 4\alpha + [(1 - \frac{x_0}{2})(1 - 4\alpha) - 2]e^{-x_0/2} + 8\alpha e^{-\alpha x_0}} \right| \quad (3-35)$$

Both values of  $s_x$  are also depicted in Figure 3.8 as functions of  $\alpha$ , and their minima occur at the same value of  $\alpha$  given by:

$$\alpha = \alpha'_{opt} = \frac{3}{8} = 0.375 \quad (3-36)$$

So, with respect to minimising the error resulting from the drift of  $\alpha$ ,  $\alpha'_{opt}$  is the optimal value to choose in designing both PLD systems. It can be noticed that the minimum value of  $s_x$  for the PLD-PMSR is a little less than that for the PLD-AMSR.

In summary, the choice of the optimal value of  $\alpha$  for a single reference PLD system lies between  $\alpha_{opt}|_{AMSR} \approx 0.348$  and  $\alpha'_{opt} = 0.375$ . In fact, both values of  $s_y$  and  $s_x$  do not vary very much with  $\alpha$  in the above region for PLD-AMSR and PLD-PMSR, as illustrated in Figure 3.8, and  $\alpha$  can be chosen within this range taking into account the convenience of the design of the electronic circuit. In addition, with reference to the values of  $s_y$  and  $s_x$ , the overall performance of the pulse modulated scheme is better than that using analog modulation. Moreover, apart from the ease of implementation, the use of pulse modulation can greatly simplify the design of the system by allowing the use of digital components for the signal generating and timing circuits and further increase the stability of the system.

A circuit design example of the PLD-PMSR scheme is presented in Appendix A (page 174). In this example, the phase shift ratio  $\alpha$  is chosen at the value of  $3/8$ , which is within the optimal region mentioned above. In addition, the signal generator circuit uses least number of electronic components to generate the required modulation and reference signal,  $v_m$  and  $v_r$  when the phase shift ratio between them is set at  $3/8$ . In this design, no special or expensive components are used, and the minimum value of fluorescence lifetime

measurable is set at 10 $\mu$ s. By changing the timing components of the VCO, the system could measure a fluorescence lifetime down to  $\sim$ 1 $\mu$ s, a limit set by the high performance of AD630, the switch-type mixer used here.

### 3.6. The impact of excitation leakage on single reference PLD schemes

A departure from the theoretically ideal set-up of the fluorescence inducing and detecting devices (the FID in Figures 3.3&3.4) will result in a substantial component of the excitation light being received by the photo-detecting device, where only the detection of the fluorescence in the system is required, and the excess radiation from the source, pouring to the detector is termed the excitation leakage. In the case of the PLD-AMSR shown in Figure 3.3, when the fluorescence signal,  $v_f$ , is additionally contaminated by the excitation leakage, the actual output of the FID is designated as  $v_{f+l}$  and may be expressed as:

$$v_{f+l} = v_f(t) + v_l(t) \quad (3-37)$$

where  $v_f(t)$  is as defined in Eq. (3-12); and

$$v_l(t) = V_{lo} \sin\omega t \quad (3-38)$$

is the excitation leakage which is in phase with the modulation signal,  $v_m$  with its maximum amplitude as  $V_{lo}$ . As the result, the output of the PSD will be given by:

$$y = \frac{2}{\pi} kV_A [\cos(2\pi\alpha - \varphi) + \eta] \quad (3-39)$$

where  $\eta$  is the excitation leakage-to-fluorescence ratio, given by:

$$\eta = V_{lo} / V_A \quad (3-40)$$

Then, in the presence of the excitation leakage, the gain of the lifetime-to-period conversion can be rewritten as:

$$x_o' = \frac{2\pi}{\tan[2\pi(\alpha - 1/4) - \arcsin\eta]} \quad (3-41)$$

In Figure 3.9, the relative change of the conversion gain in the case of  $\alpha=3/8$ , is plotted as a function of the fluorescence-to-excitation leakage ratio, according to the following expression:

$$\frac{\Delta x_0}{x_0} = \frac{x_0' - x_0}{x_0} = \frac{\tan[2\pi(\alpha - 1/4)]}{\tan[2\pi(\alpha - 1/4) - \arcsin\eta]} - 1 \quad (3-42)$$

It is obvious that the value of  $x_0'$  can vary dramatically with the presence of excitation leakage. A higher percentage of  $\eta$  can even cause the operation of the system to fail. It can be shown that when:

$$\eta \geq \sin[2\pi(\alpha - 1/4)] \quad (3-43)$$

the system will have no locked state. For instance, in the case of  $\alpha=3/8$ , when  $\eta \geq \sin(\pi/4) \approx 0.707$ , the system will not reach the locked state.

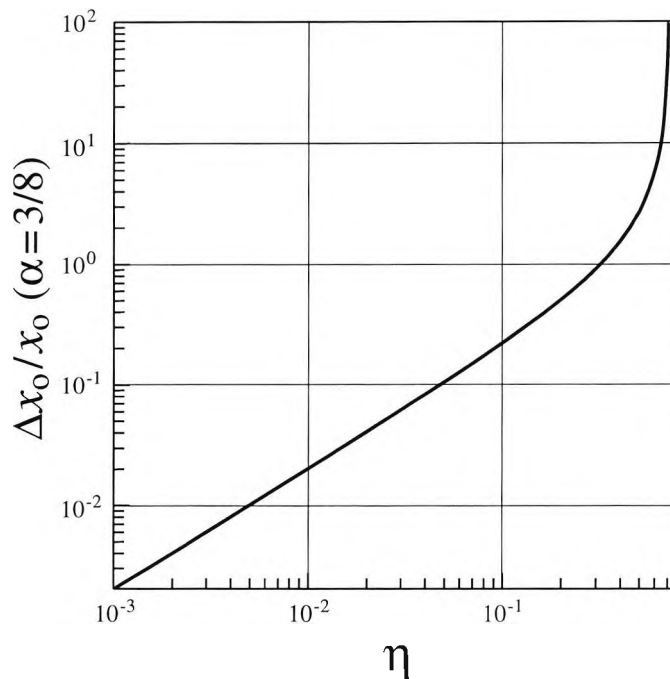


**Figure 3.9:** The impact of the excitation leakage (in the case of AMSR with  $\alpha=3/8$ ).

### 3.7. Pulse modulated PLD with two reference signals (PLD-PMTR)

To tackle the excitation leakage problem, another pulse modulated PLD scheme has been developed which uses two switch-type mixers with different reference signals [49], as presented schematically in Figure 3.10. The waveforms of the signals designated in Figure 3.10 are drawn in Figure 3.11. On the assumption of the presence of the excitation leakage, the output of the FID (in Figure 3.10),  $v_{f+l}$  is given as:

$$v_{f+l} = v_f(t) + v_l(t), \tag{3-44}$$

where  $v_f(t)$  is the true fluorescence response, defined in Eq.(3-19), and  $v_l(t)$ , is the excitation leakage. Therefore, the outputs of the mixers M1 and M2 shown in Figure 3.10,  $v_{mix1}$  and  $v_{mix2}$  could also be expressed as the sums of their fluorescence and excitation leakage component respectively, as depicted in Figure 3.11, where the upper traces of  $v_{mix1}$  and  $v_{mix2}$  are components corresponding to the fluorescence response and the lower traces are those corresponding to the excitation leakage. The leakage signal  $v_l(t)$  is in phase with the modulation signal  $v_m$  and is rectangularly profiled, and thus  $v_{f+l}$  could be written as:

$$v_{f+l} = v_{f+l}(t) = \begin{cases} v_f(t) + V_{lo}, & 0 \leq t < \tilde{T}/2 \\ v_f(t) - V_{lo}, & \tilde{T}/2 \leq t < \tilde{T} \end{cases} \tag{3-45}$$

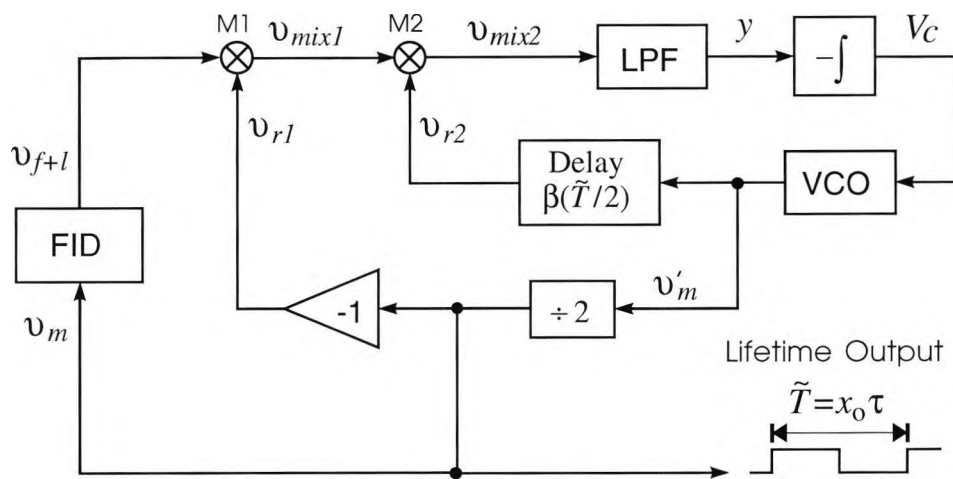
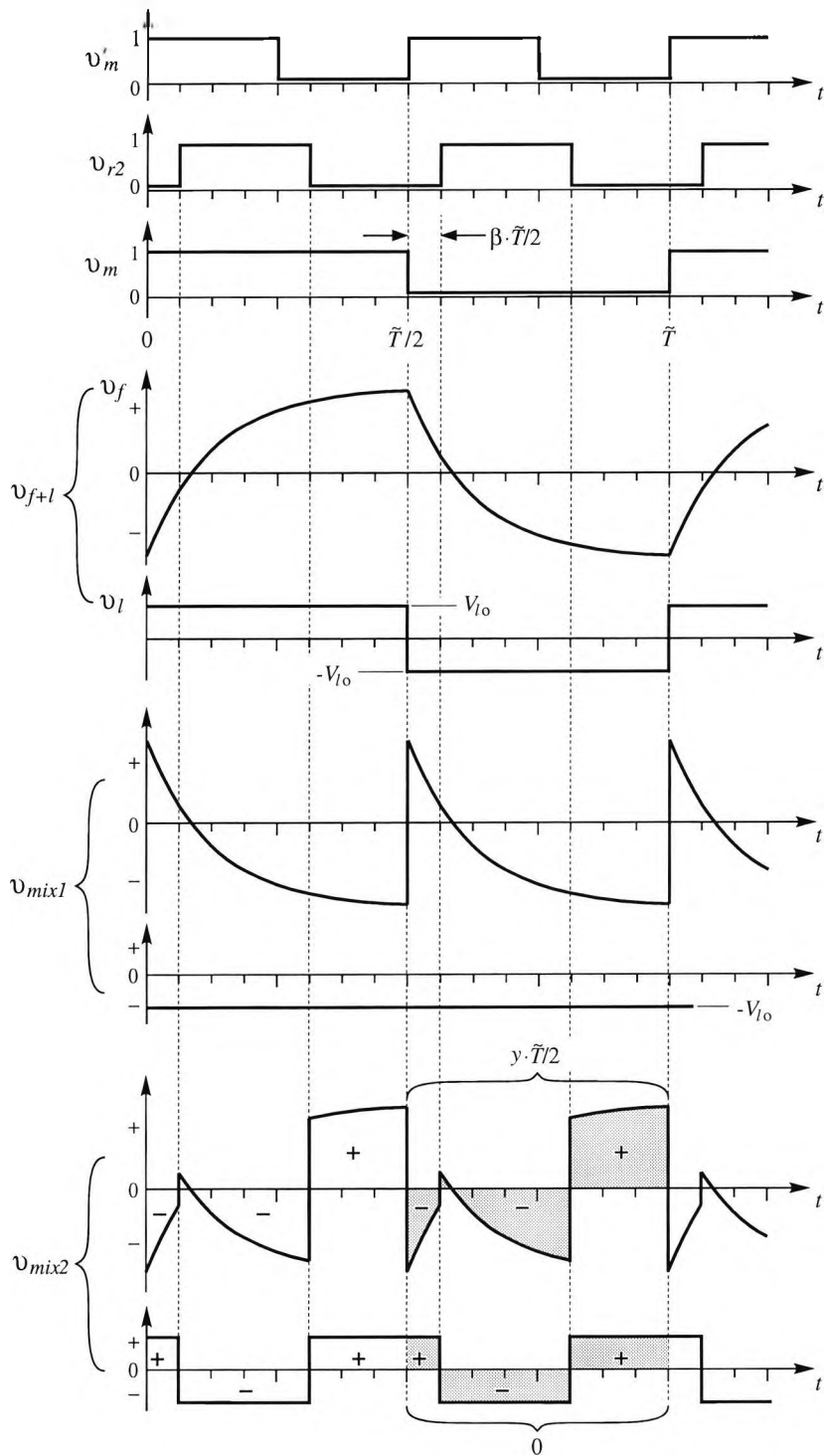


Figure 3.10: A PLD-PMTR system. (Components as Figure 3.1)



**Figure 3.11:** Waveforms of signals designated in Figure 3.10.

where  $V_{l0}$  is the amplitude of the excitation leakage.

Then as illustrated in Figure 3.11, the output of the first mixer is given as:

$$v_{mix1} = -v_f(t) - V_{l0}, \quad 0 \leq t \leq \tilde{T}/2, \quad (3-46)$$

and

$$v_{mix1}(t + T/2) = v_{mix1}(t). \quad (3-47)$$

Thus,  $y$  is given as:

$$\begin{aligned} y &= \frac{1}{T} \int_0^T v_{mix2}(t) dt = \frac{2}{T} \int_0^{T/2} v_{mix2}(t) dt \\ &= \frac{2}{T} \cdot \left[ \int_0^{\beta T/2} v_f(t) dt - \int_{\beta T/2}^{(\beta+1/2)T/2} v_f(t) dt + \int_{(\beta+1/2)T/2}^{T/2} v_f(t) dt \right] \\ &+ \frac{2}{T} \cdot \left[ \int_0^{\beta T/2} V_{lo} dt - \int_{\beta T/2}^{(\beta+1/2)T/2} V_{lo} dt + \int_{(\beta+1/2)T/2}^{T/2} V_{lo} dt \right] \end{aligned} \quad (3-48)$$

where the last part of the above expression equals zero,  $y$  is determined only by the true fluorescence response as illustrated graphically in Figure 3.11. It can be shown that:

$$y = f(x, \beta) = \frac{4kV_{A0} (1 - e^{-x/4})(1 - 2e^{-\beta x/2} + e^{-x/4})}{x \cdot (1 + e^{-x/2})} \quad (3-49)$$

This integral value is independent of the excitation leakage. Hence the gain of lifetime-to-period conversion of this PLD system, which is expressed as:

$$x_0 = x \Big|_{f(x, \beta)=0} \quad (3-50)$$

is also independent of the excitation leakage. Therefore the system is theoretically immune to the effect of excitation leakage.

In Figure 3.12,  $x_0$  is depicted as a function of  $\beta$ , as a solid line, together with that for the PLD-PMSR scheme as a dashed line for comparison. Also the values of  $x_0$  against some typical values of  $\beta$  are listed in Table 3.1, along with their counterparts in other PLD schemes.

The relative sensitivity of  $x_0$  to  $\beta$  is expressed as the following:

$$s_x = \left| \frac{1}{x_0} \frac{dx_0}{d\beta} \right| = \frac{1}{x_0} \left| \frac{\partial f / \partial \beta}{\partial f / \partial x_0} \right|_{f(x_0, \beta)=0} = \frac{e^{-\beta x/2}}{\beta e^{-\beta x/2} - e^{-x/4} / 4} \quad (3-51)$$

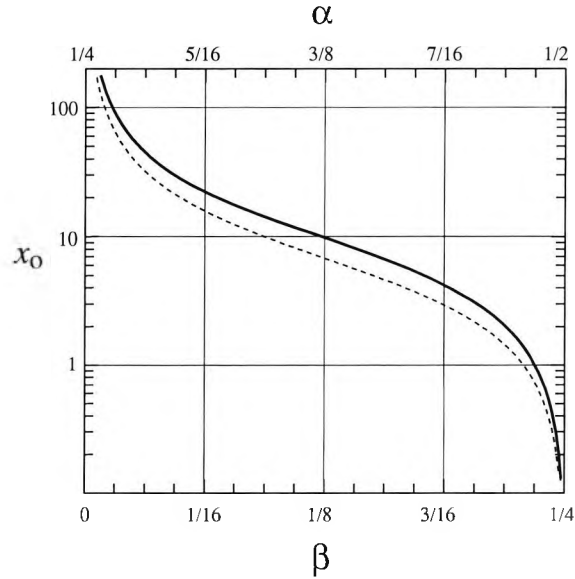


**Figure 3.12:**  $x_0$  vs.  $\beta$  for PMTR in solid line;  $x_0$  v.s.  $\alpha$  for PMSR in dashed line.

**Table 3.1:** Values of  $x_0$  against some typical values of the phase shift ratio  $\alpha$  or  $\beta$  in various PLD schemes.

$\alpha =$	$5/16$	$3/8$	$7/16$
AMSR	15.169	$2\pi$	2.603
PMSR	15.768	6.784	2.923
PMTR	22.052	9.75	4.178
$\beta =$	$1/16$	$1/8$	$3/16$

and is depicted as a function of  $\beta$  on a logarithmic scale as curve 1 in Figure 3.13. The minimum value of  $s_x$  occurring at  $\beta=0.12$ , is very close to that for PLD-PMSR.

The relative sensitivity of  $y$  is given by:

$$s_y = \left| x \frac{dy}{dx} \right|_{y=0} = \frac{4kV_{A0}(1-e^{-x_0/4})}{1+e^{-x_0/2}} \times \left| \beta e^{-\beta x_0/2} - \frac{e^{-x_0/4}}{4} \right| \quad (3-52)$$

It is also plotted as curve 2 in Figure 3.13, as a function of  $\beta$ , with its values normalised against the product of  $k$  and  $V_{A0}$ . Those for the PLD-AMSR and the PLD-PMSR are also presented in the same figure as curves 3 and 4 respectively. The maximum value of  $s_y$  occurs at  $\beta=0.117$  with the magnitude being  $\sim 60\%$  of that for PLD-PMSR.

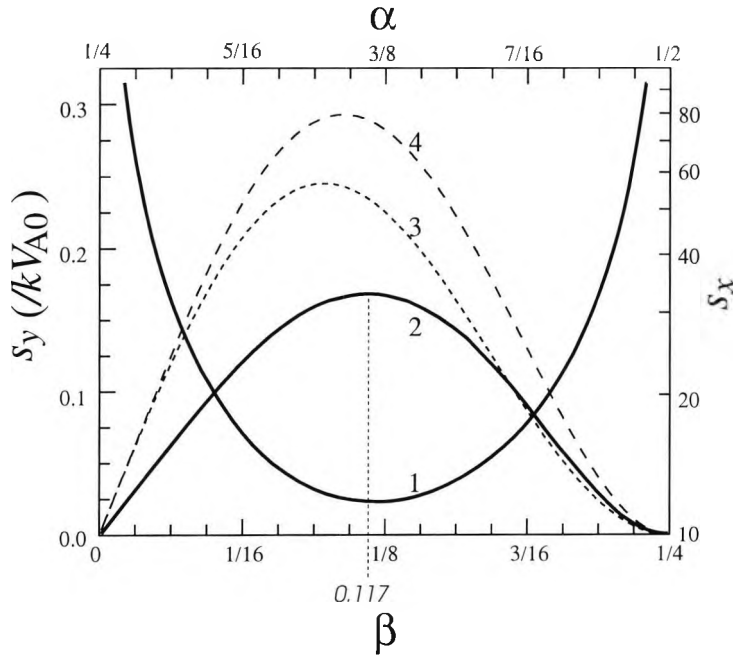


**Figure 3.13:** Curve 1:  $s_x$  vs.  $\beta$  for PMTR; curve 2:  $s_y$  vs.  $\beta$  for PMTR; curve 3:  $s_y$  vs.  $\alpha$  for AMSR; curve 4:  $s_y$  vs.  $\alpha$  for PMSR.

In some applications, it may be preferred that only the decay part of the fluorescence evolution be processed to give the measurement of its lifetime. The PLD-PMTR scheme presented in Figure 3.10 can be adapted to meet such a requirement by replacing the mixer designated as M1 in Figure 3.10, with an analog switch in the configuration as depicted in Figure 3.14. This will introduce some change of the waveforms of the output signals of the two mixers as shown in Figure 3.15. As the result,  $y$ , the output of the PSD is only determined by the decay process of the fluorescence response, as does the gain of the lifetime to period conversion,  $x_0$ . The above change will reduce  $s_y$ , the sensitivity of the PSD output to lifetime by 50%, but will not alter the lifetime conversion gain,  $x_0$ . This revision of the PLD-PMTR scheme is distinguished as the Single Sided PLD-PMTR.

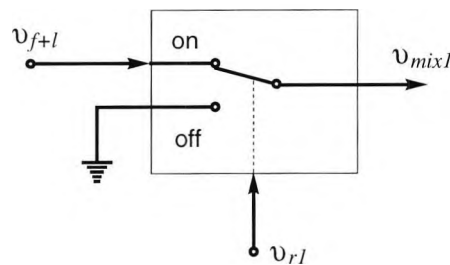


**Figure 3.14:** The configuration of the pre-mixer for single sided PLD-PMTR.

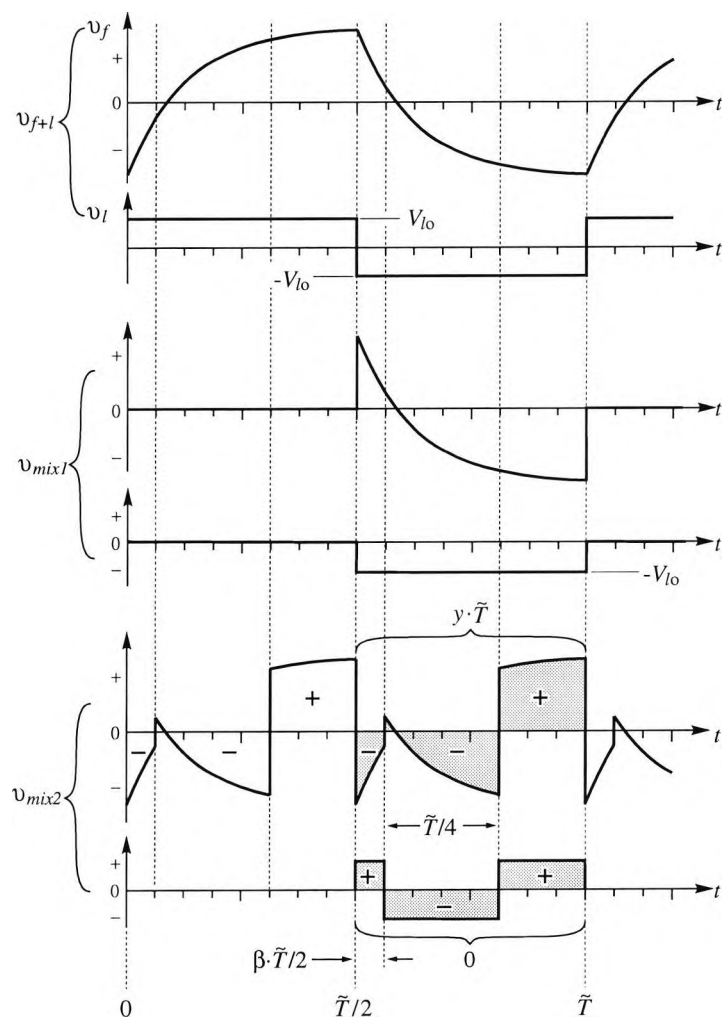


Figure 3.15: Waveforms of signals designated in Figure 3.14.

### 3.8. Discussion

In motoring the fluorescence response signal,  $v_f$ , it is not necessary to use DC-decoupling before the input of a PLD system, for theoretically the DC component of the response signal will be filtered out by the PSD in the system. The assumption that  $v_f$  is DC-decoupled is made partially for the ease of illustration. In practice, DC-decoupling of the response signal is also desirable to increase the dynamic input range of the PSD or its pre-mixer.

Though the use of the PLD-PMTR schemes results in a 60% reduction of the PSD output sensitivity for the two-sided scheme shown in Figure 3.10, it is greatly compensated by the advantage of being theoretically immune to the excitation leakage. This advantage

is critical for a fibre optic sensor scheme where the level of the excitation leakage could be quite significant due the lack of flexibility of the geometrical arrangement of the fluorescence sample. The single sided PLD-PMTR scheme will further reduce the PSD output sensitivity by 50%; however, with this scheme, the temporal waveform of the excitation pulse need not be strictly rectangular. This feature gave the latter a better measurement reproducibility compared to the other PLD scheme.

After all, based on the lock-in techniques, the whole category of the PLD schemes is featured with a high noise-suppression ability. With the measurand being converted to a repetitive signal of which the the period is directly proportional to the measurand, the measurement output of a PLD system can be transferred faithfully for a long distance and is easy to interface with computer; and moreover further high measurement resolution (better than 0.1%) is achievable over wide consecutive measurement range (1:1000). The electronics of a PLD system is inexpensive and compact, and the minimum of measurable fluorescence lifetime is  $\sim 1 \mu\text{s}$ , a limit set by the electronic components used. All these features make the PLD schemes highly suitable for fluorescence thermometer applications.

### 3.9. Impact of this work

Though the primitive form of the PLD-PMSR scheme was initiated in the work of Bosselmann *et al* [46, 20], the detail description of this scheme, with theoretical analysis and design considerations, is first published as a result of the work [47] carried out independently in this thesis study. The novelty and originality of the PLD-PMTR schemes developed in this study [49, 31], are obvious. These schemes overcome the vital shortcoming of the PLD-PMSR scheme and other phase modulation schemes, that is the vulnerability to the excitation light leakage, while retain all the advantages which the latter has. The advantages of the PLD techniques, as listed before, are well illustrated in their applications in various thermometer schemes which are to be discussed in the following Chapters. It is believed that this category of technology should be much preferred in the development of cost-effective fluorescence-based fibre optic thermometers.

# Cr<sup>3+</sup> Fluorescence Thermometers and Applications of PLD Techniques

---

### 4.0. Abstract

In this chapter, the general optical arrangement of several fluorescence thermometers are briefly reviewed first. Then three Cr<sup>3+</sup> fluorescence lifetime based fibre optic thermometer schemes, developed in the course of this study, are presented, either for wide range temperature measurement, or for biomedical applications. The Phase-Locked Detection technique (PLD) techniques are employed in these thermometer schemes, and their advantageous features are demonstrated by the use of a wide consecutive measurement range and the sensor resolution achieved. Some considerations in relation to specific applications, e.g. in high temperature sensing or in medical RF hyperthermia treatment, are discussed. Finally, the development of a metal-coated high temperature fibre probe will be described in the discussion of a related thermometer scheme, and results on its use provided.

## 4.1. Introduction

As discussed in Chapter 2,  $\text{Cr}^{3+}$  ions in ionic crystals interact strongly with the crystal-field strength and the lattice vibrations. Thus  $\text{Cr}^{3+}$  activated materials are characterised by a wide optical absorption spectrum, and a significant variety in temperature dependences of fluorescence lifetime is found in such materials, which can cater for differing thermometric needs over various temperature regions. Though a great diversity of such temperature dependences could be observed from one host material to another, the profile of such a dependence could be predicted, based on one of the two configurational coordinate models proposed in Chapter 2, according to the crystal-field strength of the host. This is of advantage in the selection of most suitable sensing materials for any required thermometric application.

In addition, compared with the use of the rare-earth activated materials, the use  $\text{Cr}^{3+}$  activated materials as sensors also show some significant advantages in relation to the optics of the sensor instrument itself. Firstly, as mentioned before, the wide optical absorption spectrum of  $\text{Cr}^{3+}$  activated materials, which spans from the ultra violet (UV) to the red portion of the visible spectrum, allows a great variety in the choosing of excitation light sources, and this makes it possible to use cheaper and more compact light sources for excitation, e.g. high power light-emitting diodes (LEDs) and visible laser diodes. These diode light sources are also rather convenient to modulate electronically. This convenience allows them to be directly incorporated with the circuits based on various effective signal processing schemes, e.g. the PLD techniques, without additional light modulation apparatus, such as a mechanical or electrical shutter, acousto-optic modulator, or the high-voltage-controlled Pockels cell such as that used by Augousti *et al*<sup>[66]</sup> in an alexandrite fluorescence decay based temperature sensor scheme which employs a He-Ne laser as the excitation light source.

Secondly, due to the wide absorption spectrum, a small level of wavelength drift in an LED or laser diode will not cause significant change, either increasing or reducing in the intensity of the resulting fluorescence. This frees the excitation schemes from the strict control of the spectrum of the excitation light, and gives a substantial tolerance on the peak emitting wavelength of the excitation source.

Thirdly, the fluorescence of most  $\text{Cr}^{3+}$  activated materials consists of either the red *R*-lines or a broadband red-infrared emission with the peak wavelength ranging from  $\sim 750\text{nm}$  to  $\sim 1000\text{nm}$ , or both. This can be very effectively detected by the use of stable, compact and inexpensive silicon PIN photodiodes. All the above features are highly favoured in the terms of compact and convenient instrumentation.

## 4.2. Optical arrangement of fluorescence lifetime thermometers

The optical arrangement of a typical fluorescence lifetime thermometer is one of the simplest among those of various fibre optic sensor schemes discussed. Examples of a typical optical arrangement used in several  $\text{Cr}^{3+}$  based fibre optic thermometer schemes are illustrated in Figure 4.1. In Figure 4.1(a) the optical arrangement which has been used by Bosselmann *et al* [20] in a scheme based on a chromium activated material,  $\text{Lu}(\text{Cr}_x\text{Al}_{1-x})_3(\text{BO}_3)_4$  is shown. The arrangement used by Grattan *et al* [29] in a ruby fluorescence based thermometer is depicted in Figure 4.1(b), which was aimed to be simple and of low cost, at the expense of a relatively low signal-to-noise ratio. That shown in Figure 4.1(c) is the apparatus employed in this work in a  $\text{Cr}:\text{LiSAF}$  based thermometer for biomedical applications [30]. As is seen in these examples, the optical arrangement of a  $\text{Cr}^{3+}$  fluorescence lifetime based thermometer consists, in general, of the following three parts:

- a. **An excitation light source** with an appropriate emission spectrum to induce a significant fluorescence response from the sensing materials, and with some accessories to facilitate the modulation of the output light intensity. Although it is possible to supply high-energy excitation over the absorption band of the material with UV light sources, like the flash lamp used by Wickersheim and Alves [19], it is much simpler to use a visible laser diode or LED, or a He-Ne laser, to pump into the lowest energy absorption band from the green to the red portion of visible spectrum, which exists in almost all of  $\text{Cr}^{3+}$  activated fluorescent materials. LED sources can be electronically modulated and now offer as high power output as many He-Ne lasers which must, however, be acousto-optically or electro-optically modulated. With both the advantages of LED and He-Ne laser sources, laser diodes are the most promising excitation light sources, and it is an ideal light source for the excitation of  $\text{Cr}^{3+}$  fluorescence in

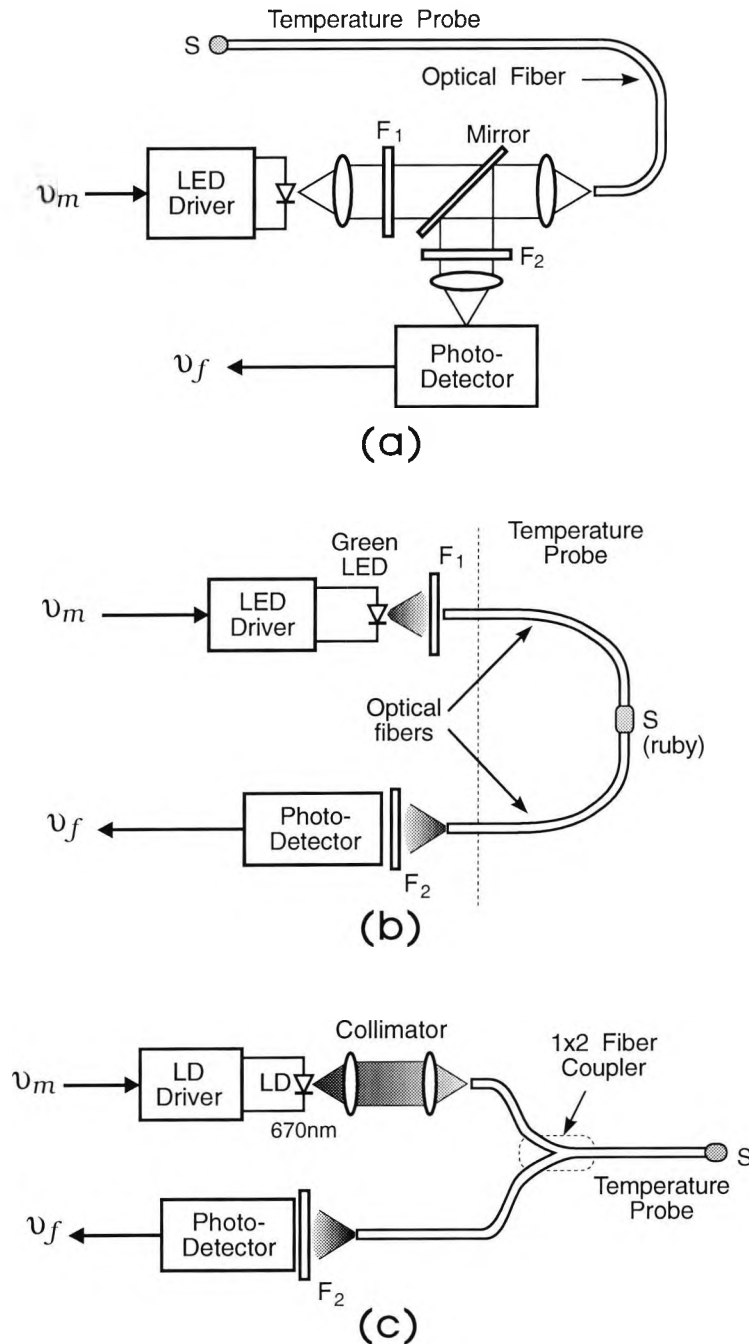


**Figure 4.1:** Schematics of the optical arrangement and temperature probes for the  $\text{Cr}^{3+}$  fluorescence lifetime based fibre optic thermometers.  $S$ : the fluorescence material used as sensing element;  $\nu_m$ : signal to modulate the output intensity of the excitation light source;  $\nu_f$ : the detected fluorescence response from the sensing element; **LED**: light emitting diode;  $F_1$ : short-pass optical filter;  $F_2$ : band-pass or long-pass optical filter; **LD**: laser diode.

a sensor system. Rapid advances in laser diode technology and a steady reduction in its price has been seen in recent years. Thus it is not supposing to see the ultimate use of laser diodes in fibre optic sensor systems;

- b. **A photodetector** with suitable response spectrum for the detection of the fluorescence emission. As mentioned before, the fluorescence of most  $\text{Cr}^{3+}$  activated materials consists of either the red *R*-lines or broadband infrared emission with the peak wavelength ranging from  $\sim 750\text{nm}$  to  $1000\text{nm}$ , or both. Thus, the widely available compact and inexpensive silicon PIN photodiodes are the most suitable photodetectors for the application discussed herein. In some particular circumstances where high speed and high sensitivity detection is required, a silicon based avalanche diode could be the best alternative for the PIN photodiode;
- c. **Variety of optical alignment accessories** for the launch of the excitation light into the fibre optic temperature probe, the collection of the fluorescence response, and optical filters used to isolate the excitation and fluorescence emission at the detector and in some cases at the excitation source, as well.

Fibre optic fluorescence thermometry can provide quite several flexible approaches to access the required measurement areas. The temperature probes can be configured for remote measurement, as shown in Figure 4.2, where the sensing material is detached from the optical fibre and coated onto the surface of the object. An unique application of this approach has been demonstrated by Noel *et al*<sup>[67]</sup> in the measurement of temperatures on the blades and vans of an operating turbine-engine, an extremely difficult measurement task for the conventional thermometry technologies.

For general thermometric applications, the probes are constructed for actual contact measurement, with the sensing materials directly attached to the optical fibres, as shown in Figure 4.3. In the contact measurement configuration, temperature probes could be of either the reflection-type, as that in Figure 4.3(a) shows, or the transmission-type as is that in Figure 4.3(b). The use of transmission-type probes can avoid the need for the optical accessories for the coupling of the excitation light and the fluorescence into the sensor system, as illustrated in Figure 4.1, where the transmission-type probe may be used in the arrangement depicted in Figure 4.1(b) while the reflection-type probes are also used in the other arrangements shown in the same figure. Thus, the application of transmission-type probes can simplify the design of the optical arrangement and consequently reduce the cost of the device. However, this could cause inconvenience for users in planting the probe in

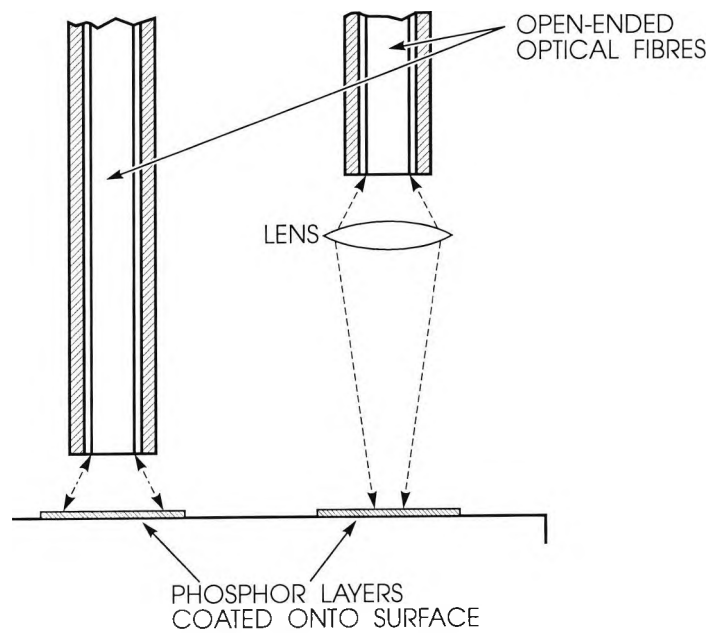


**Figure 4.2:** Remote measurement probes [68].

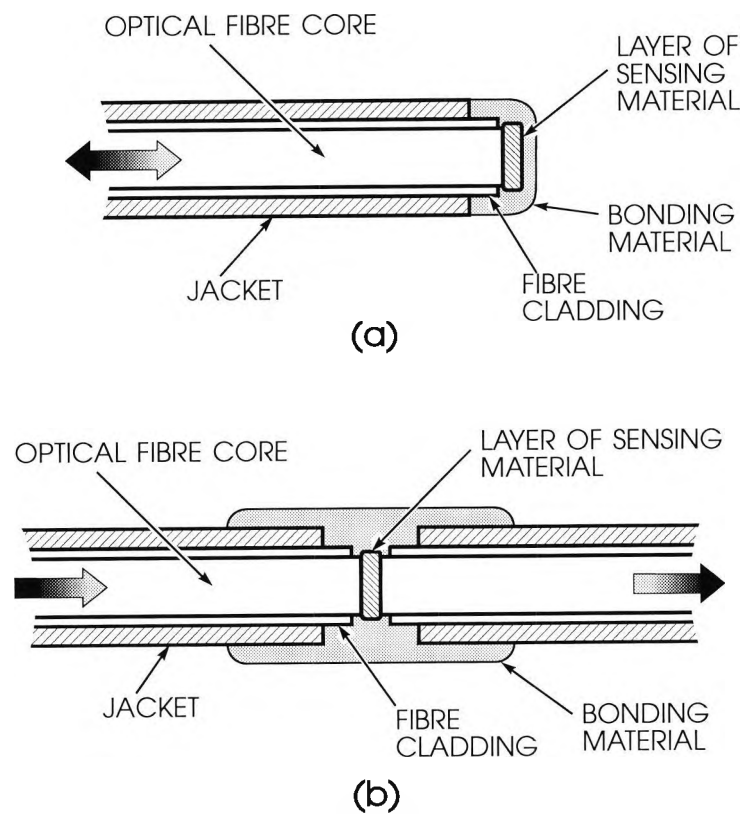


**Figure 4.3:** Temperature probes for contact measurement. (a). The reflection-type probe; (b). the transmission-type probe.

the region where the measurement is to be made. Therefore the reflection configuration of temperature probes is more widely used in the development of commercial devices.

Of course, the temperature probes could be further classified according to specific applications, e.g. biomedical temperature measurement, high temperature sensing up to  $>500^{\circ}\text{C}$ , etc. The development of the temperature probes for the applications cited is among the objectives of this work, and it will be discussed in the following sections, where the specific application is concerned.

### 4.3. Ruby based thermometer using PLD-PMSR technique with potential range 20 to 600°C

Apart from being a precious gem stone, ruby is well-known as the laser crystal used in the world's first successful laser operation. It is also among those earliest materials of which the fluorescence lifetime properties were proposed for thermometric applications [18]. The actual use of ruby as the sensor element in a fibre optic fluorescence lifetime thermometer was perhaps first reported by Grattan *et al* [29]. In this thermometer system, an LED was used as the excitation light source and a silicon PIN diode was employed for the detection of the fluorescence signal. The temperature measurement has been achieved over the region from room temperature to 170°C. The thermometer system described in this section was devised in an effort to extend the measurement range of this compact and low-cost system and further improve and conveniently extend its performance.

#### 4.3.1. Experimental setup

The experimental system setup of the ruby fluorescence thermometer developed in this work is schematically depicted in Figure 4.4. A green LED, Type TLMP 7513 manufactured by III-V semiconductors with a typical luminosity of 300 mcd, was used as the excitation source, which can pump into the strong absorption band centred at ~550nm, as shown in the absorption spectrum of ruby in Figure 4.5. As the radiation of the green

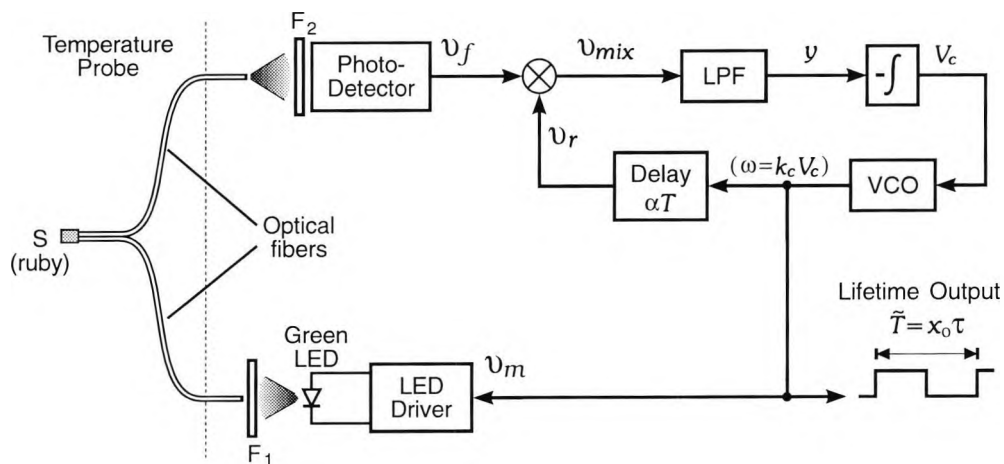


**Figure 4.4:** The ruby fluorescence lifetime based fibre optic thermometer system. **F1**: short-pass optical filter; **F2**: R-line band-pass optical filter.

LED contains weak emission band in the red portion of visible spectrum, which overlaps part of the fluorescence emission spectrum, a short-pass optical filter,  $F_1$  shown in Figure 4.4, with the cut-off wavelength at 630nm is used to eliminate this red "tail" of the LED emission. The fluorescence emission spectrum is obvious at longer wavelengths, as shown in Figure 4.6, with the strongest emission on the  $R$ -lines (around 694 nm). Thus, a long-pass Schott glass filter, e.g. RG695, could be used as the  $F_2$  in Figure 4.4, to isolate the excitation light from the fluorescence emission at the detector stage. However, in order to achieve better isolation, a band-pass interference filter with the pass-band centred at 694.3

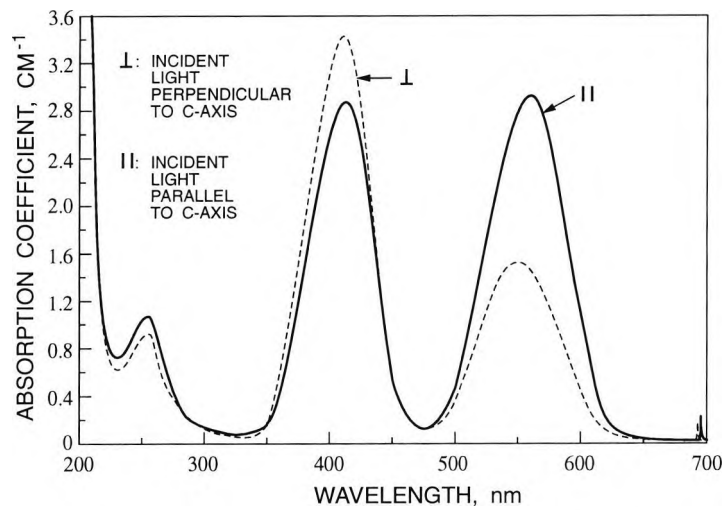


**Figure 4.5:** The absorption spectrum of ruby. From Evtuhov and Neeland [69].

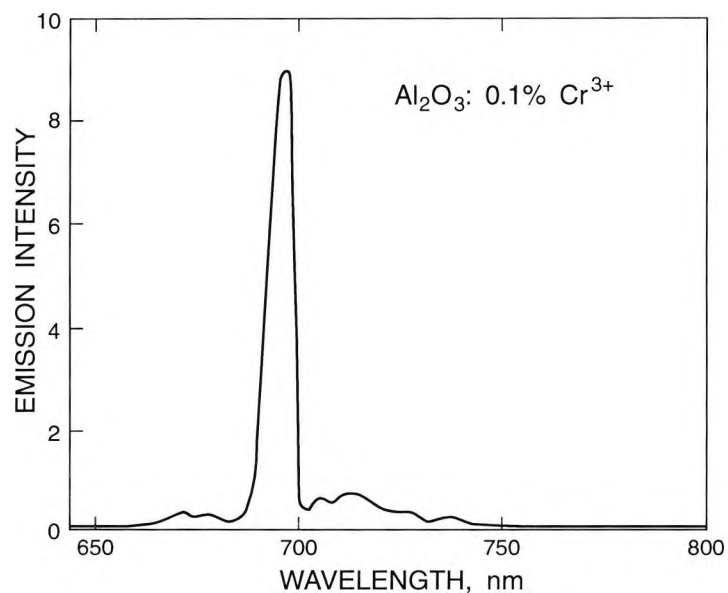


**Figure 4.6:** The emission spectrum of ruby. From Fonger and Struck [52].

nm and a bandwidth of 12 nm, Ealing Type 35-4100, is used as the filter  $F_2$  in Figure 4.4 instead.

In this system, gold-coated silica fibres were first used to fabricate the probe for temperature measurement up to  $\sim 600^\circ\text{C}$ . The core diameter of the fibre used is  $400\mu\text{m}$ . The probe is configured in the reflection-type configuration, similar to that shown in Figure 4.3(a). Due to the lack of a large diameter fibre coupler and the corresponding fibre slicing device in the laboratory when the system was set up, the probe had to be made of a bundle of the gold-coated fibres, so that at the sensor end, the transmission of the excitation light and the collection of the fluorescence response are via separated fibres. The detail of the construction of this special gold-coated fibre probe will be presented in the latter section.

Due to the low emission intensity of the LED light source, the intensity of the induced fluorescence response which could be detected at the photodetector stage, is only in the order of several nanowatts. Thus a poor signal-to-noise ratio of the detected fluorescence response is observed, as illustrated in Figure 4.7 by the temporal profile of the photodetector output recorded by a digital oscilloscope when the sensor is exposed at room temperature. An even less favourable signal-to-noise ratio is expected at higher temperatures due to the decrease in the fluorescence intensity with the increasing temperature.

To tackle the poor signal-to-noise ratio problem, the "phase and modulation method" reviewed in Chapter 1 was used by Grattan *et al*<sup>[29]</sup> to measure the fluorescence lifetime,

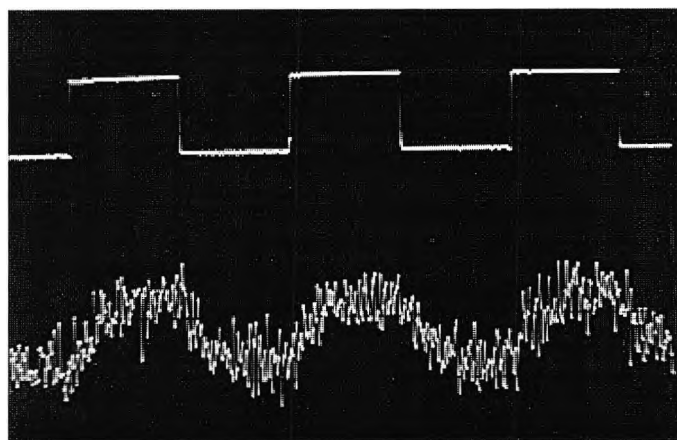


**Figure 4.7:** Temporal profiles of excitation light and fluorescence emission at room temperature. **Upper trace:** modulation signal applied to the LED with a frequency of  $\sim 40\text{Hz}$ . **Lower trace:** fluorescence response signal output by the photodetector shown in Figure 4.4.

with the employment of a high Q-value bandpass electronic filter to the wideband noise in the fluorescence signal. Though the effectiveness of this scheme was well demonstrated, its measurement range is limited by the fixed single modulation frequency, and a slight drift in the parameters of the high Q-value bandpass filter could introduce error in the phase measurement. The latter would impair long term measurement stability of the system.

To solve the above problems, the PLD-PMSR technique described in Chapter 3 was devised in this work and was applied to this ruby based thermometer system, as shown in Figure 4.4. Here, the phase shift ratio,  $\alpha$ , is chosen to be  $3/8$ , an optimum value according to the discussion in Chapter 3, and thus the gain of the lifetime to period conversion,  $x_0$ , is given as 6.78.

#### **4.3.2. Development of the high-temperature fibre probe**

The novel part of the temperature probe in this thermometer system is the use of gold-coated fibres, which are well suited to the specific application to allow high temperature to be reached, as they have more favourable characteristics than the plastic-clad silica (PCS) fibres used earlier<sup>[29]</sup> for such a high temperature region. The fluorescent material, ruby, is sealed in a small metal enclosure, which is soldered using gold working techniques developed in the course of the work to secure it to the end of the optical fibres. This would enable a strong and secure join to be made and produce a probe which could be totally immersed in the hot region, where the measurement is to be made. As the fibre was small as was the gold and crystal of small mass, and so on, the thermal response of the device could be relatively rapid and the cost of expensive material kept low. The aim was to measure continuously over the range from room temperature (and potentially below) to 600°C.

##### **4.3.2.1. Characteristics of the metal-coated fibres used**

The feasibility of developing this particular high-temperature fibre optic probe was based on the availability of fibres with a high-temperature capability. Normal PCS fibre is limited to a maximum operating temperature of ~150°C but in order to exploit the much higher temperature capability of sapphire-based materials such as ruby, another type of fibre is needed. A range of such fibre is fabricated by Fibreguide Industries<sup>[70]</sup> and of these

the type with the highest temperature capability has an upper temperature limit of 750°C. This considerable improvement is achieved through the use of a thin gold coating on the silica material. The probe was constructed using four 400- $\mu\text{m}$  fibres using two of them to carry the excitation light and two to receive the fluorescence. These fibres are considerably less expensive than the next largest available size, 800- $\mu\text{m}$ , which would offer a greater emitting and receiving area. However, there is some considerable loss of probe flexibility with the use of these larger fibres. They are of fused silica core and doped silica cladding. The numerical aperture is 0.22 and the clad-to-core ratio of diameter used was 1:1.1. The specified temperature range of their operation is from sub-room temperature, -190 °C, to +750 °C. A particular advantage was that the metal coating offered the additional possibility of a direct metal-to-metal seal between this fibre coating and the metal capsule containing the ruby material. The thinness of the fibre coating meant that considerable research was needed to develop optimum techniques for achieving this joint, avoiding stripping the coating from the fibres and overheating the joint.

#### **4.3.2.2. Probe fabrication**

A number of probe-fabrication techniques were tried before a successful and reproducible technique was established. Gold solders and fluxes<sup>[71]</sup> were investigated experimentally and a low temperature flux was finally chosen as the most suitable. It proved impossible, as expected, to use a conventional soldering iron and a soldering iron/bunsen burner combination for jointing as this crude approach merely resulted in the stripping of the gold from the fibre.

The application of a microburner gas torch was investigated and the fine flame from this was used in a series of jointing experiments with the solder. This is similar to the type of flame used in fine gold jewellery repair and it was hoped that a successful probe could be produced. However, although a few good joints between the fibres and the thin gold sheet used to enrobe the crystals were made, it was impossible to make a reproducible joint and more often than not the fibre was stripped of its gold. Thus, it was decided to adopt a new approach, using a modified vacuum-deposition plant. The method is as described below, and copper was used, both for cheapness and because of its similar thermal properties to gold, for the crystal enclosure. The probe fabrication process is discussed in detail below and a schematic of the device is shown in Figure 4.8.

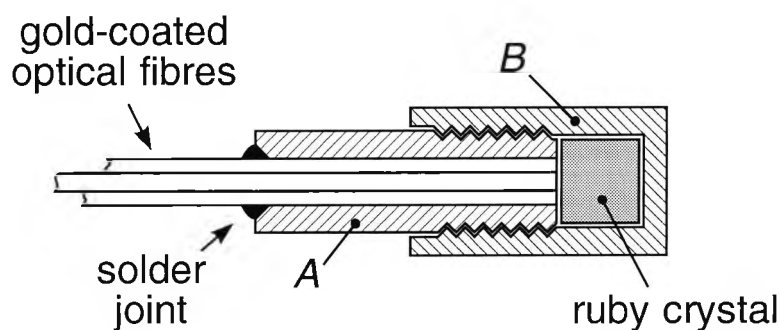


**Figure 4.8:** Schematic of the fibre-optic probe used with the ruby fluorescence lifetime based thermometer described in this thesis work.

. The threaded copper cylinder, *A*, was drilled to  $\sim 125\mu\text{m}$  over the maximum dimension of the diameter of the fibre bundle, and this cylinder was chamfered at the input end to an angle of  $45^\circ$ . The fibre ends and the copper cylinder *A* were cleaned in a solution of sodium hydroxide at  $60^\circ\text{C}$  for about 5 minutes. The alloy solder used (Easiflo 102) was reduced to a thickness of  $\sim 300\mu\text{m}$  using hydraulic rollers. In this form, the strip produced was sufficiently flexible for the required purpose.

The soldering process was undertaken in a modified vacuum coating unit to achieve closely defined and repeatable conditions, and it was found necessary to support both the probe head and the gold fibres, which can be brittle if bent excessively. The probe head, *A*, was supported vertically by screwing its base into a plate fixed in the evaporation unit. The fibres were then tied to a frame vertically above this plate. The heating element used to melt the solder was a simple ring made from a single length of tungsten wire secured between two electrodes. This ring surrounded the copper probe and care was taken to ensure that this tungsten element did not touch the probe.

The fibre bundle was pushed into the copper cylinder, *A*, until about 2 mm protruded through the threaded end. The fibres were required to be supported vertically about 50 mm away from the probe to maintain them straight and in their correct order. This support ensured that there was no strain on the bundle during the soldering process.

A short length of alloy solder was wrapped around the fibre bundle and this solder rested on the chamfered surface but did not touch the gold coating. This point has been

found critical. Failure to ensure that the alloy did not touch the metal jacket resulted in gold being torn away from the fibre and microcracks being formed. A small quantity of easy flow flux was mixed and was dropped onto the solder end. A thermocouple was positioned next to the copper head and a vacuum better than  $10^{-5}$  Torr was developed in the plant.

The heating element current was slowly increased (manually) in stages until the alloy solder finally melted and began to run. This heating process was extended over a period of approximately an hour. The current was then switched off and after the plant and probe had cooled the probe was removed, cleaned, and the threaded end with the short length of protruding fibres was polished. The probe was assembled by screwing the mating end into the copper assembly *B* which contained the ruby crystal. Calibration tests were then carried out as described below.

#### 4.3.3. The calibration of the thermometer system

The optical fibre probe was assembled with the ruby sample and placed in a small electrically-heated oven, which was insulated from the environment, and a conventional thermocouple was placed in intimate contact with it. The temperature of the oven was raised up to a maximum of  $600^{\circ}\text{C}$ , in stages of approximately  $20^{\circ}\text{C}$ , and the fluorescence lifetime output was monitored via the period of the modulation frequency as indicated in Figure 4.4. The characteristic calibration curve is shown in Figure 4.9 on a logarithmic scale, over a range from  $30^{\circ}\text{C}$  to  $\sim 550^{\circ}\text{C}$ . The calibration process was repeated several times and a similar characteristic was obtained on each occasion. In the region between  $150^{\circ}\text{C}$  and  $450^{\circ}\text{C}$ , the maximum sensitivity is seen. Beyond  $500^{\circ}\text{C}$ , the calibration curve tends to "flatten out" quite dramatically, and the sensitivity of measurement achievable in this region is limited, as shown by the dashed line in Figure 4.9, which represents the relative temperature sensitivity of the observed fluorescence lifetime,  $s_{\Delta\tau/\tau}$  defined as:

$$s_{\Delta\tau/\tau} = \left| \frac{(\Delta\tau/\tau)}{\Delta T} \right| \quad (4-1)$$

where  $\tau$  is the observed lifetime;  $\Delta\tau$  and  $\Delta T$  are the increments of the lifetime and temperature.

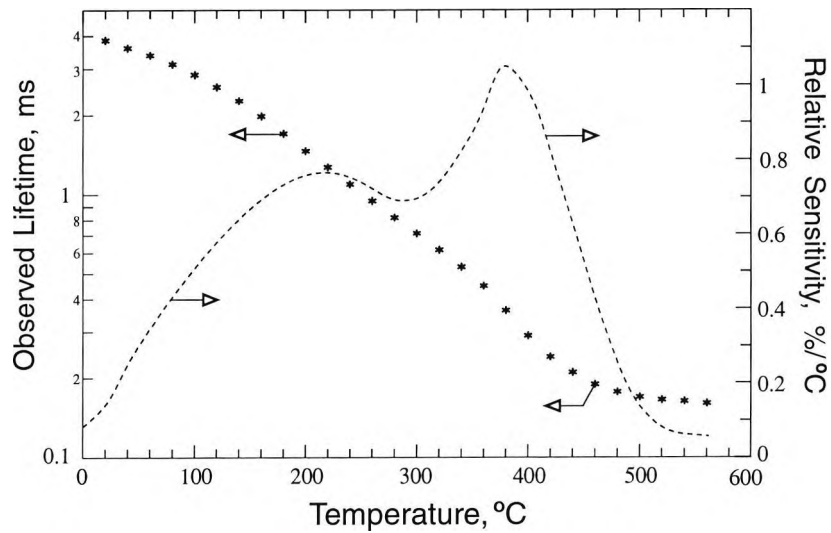


**Figure 4.9:** Characteristic calibration curve for the ruby fluorescence based thermometer in the region from room temperature to ~550°C.

The intensity of the fluorescence emission detected at the photodetector stage was plotted as a function of temperature over the same range, and this is shown in Figure 4.10. It falls off rapidly with temperature increase over the whole temperature region. This does not contradict the experimental evidence of Burns and Nathan<sup>[72]</sup> who showed that the fluorescence quantum efficiency of the ruby fluorescence integrated over the entire band from 620nm to 770nm is independent of temperature (to ~5%) in the region from -196°C to 240°C, for the emission detected here is only the R-line part of the total fluorescence

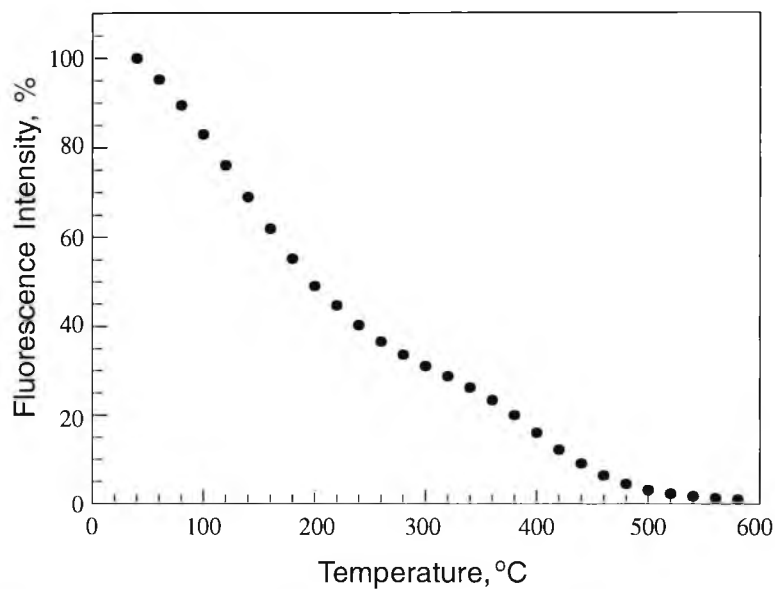


**Figure 4.10:** The ruby fluorescence intensity recorded in the experiment.

emission. The reduction in R-line emission intensity with temperature increase from room temperature to 240°C, is mainly due to the increasing thermal elevation of the excited Cr<sup>3+</sup> ions from the <sup>2</sup>E state to the <sup>4</sup>T<sub>2</sub> state, which results in a higher portion of fluorescence emission being initiated from the <sup>4</sup>T<sub>2</sub> state. This is supported by the research on the temperature dependence of ruby fluorescence showing an increase in broad band emission with temperature increase over the above region (Chapter 2, Figure 2.7).

The assessment of the measurement performance of this system was made through two procedures. The first procedure was to determine the measurement reproducibility of the system. This was based on the observation of the measurements at several temperature fixed points carried out under the laboratory conditions. The test results are listed in Table 4.1, where the control resolution of the temperature of the calibration oven were, as indicated in Table 4.1, ± 1 °C.

**Table 4.1:** Reproducibilities of the measurements made by the ruby based thermometer system.

temperature	40 ± 1 °C	180 ± 1 °C	300 ± 1 °C	500 ± 1 °C
reproducibility	3 °C	2 °C	3 °C	5 °C

The second procedure was the evaluation of the temperature measurement deviations to determine a measurement range within which the errors are under certain defined criteria for reproducibility. According to the investigation on errors and their sources in exponential-parameter estimation by Dowell and Gillies<sup>[44]</sup>, the lifetime-estimation error is proportional to the amplitude of the noise presented in the exponential signal, and thus the lifetime measurement deviation is inversely proportional to the signal-to-noise ratio of the fluorescence signal, that is given by:

$$\sigma_{\Delta\tau/\tau} \propto \frac{\sigma_N}{I} \quad (4-2)$$

where  $\sigma_{\Delta\tau/\tau}$  is the relative lifetime measurement deviation;  $\sigma_N$  the noise amplitude and  $I$  the fluorescence intensity as presented in Figure 4.10. Therefore, the estimation of the temperature measurement deviation,  $\sigma_T$  could be given by

$$\sigma_T \propto \frac{\sigma_{\Delta\tau/\tau}}{s_{\Delta\tau/\tau}} = \frac{\sigma_N}{I \times s_{\Delta\tau/\tau}} \quad (4-3)$$

where  $s_{\Delta\tau/\tau}$  is the temperature sensitivity of the observed lifetime as defined in Eq.(4-1) and as depicted in Figure 4.9 for this ruby based system; other parameters as defined in Eq.(4-2). For this system,  $\sigma_T$  is depicted as a function of temperature in Figure 4.11, where the values are normalised to its minimum at  $\sim 130^\circ\text{C}$  and,  $\sigma_N$  is treated as a constant over the entire temperature region, as  $\sigma_N$  is related to the temperature of the environment not to that of the sensor point.

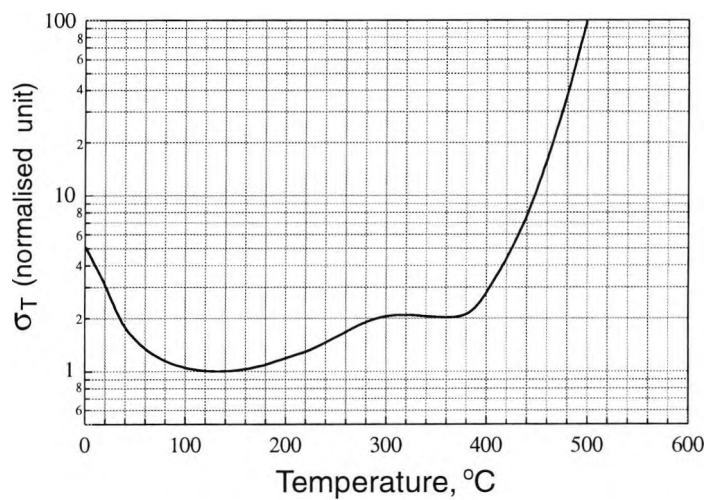


**Figure 4.11:** The calculated temperature measurement deviation of the ruby fluorescence thermometer system.

The deviation of consecutive temperature measurements at  $450^\circ\text{C}$ ,  $\sigma_{450^\circ\text{C}}$  is observed to be  $0.3^\circ\text{C}$  in the system. Thus, with reference to the  $\sigma_T$  v.s.  $T$  curve in Figure 4.11, a measurement resolution, defined by  $3\sigma_T$ , of  $1^\circ\text{C}$  or better could be expected over the region from room temperature to  $450^\circ\text{C}$  and of  $0.1^\circ\text{C}$  in the vicinity of  $130^\circ\text{C}$ .

#### 4.3.4. Further improvement

The calibration curve shown in Figure 4.9, is not inherent to the characteristic temperature dependence of the ruby fluorescence lifetime, especially over the temperature region beyond  $420^\circ\text{C}$ . As will be shown later, instead of "flattening out", the rapid

reduction in the fluorescence lifetime continues beyond 420°C and extends even to 600°C. The loss of temperature sensitivity beyond 420°C in this system is due to the long response-time of the photodetector (~120µs) which becomes longer than the ruby fluorescence lifetime beyond 420°C. Such a long response-time is an inevitable feature of a silicon PIN photodiode configured with excess high-gain for the detection of the weak fluorescence signal. Thus, the performance of the system could be improved with the use of more efficient laser source to excite stronger fluorescence emission from the ruby sample and the consequent use of a fast photodetector with enough gain for the detection of the fluorescence. The recent development of short wavelength, diode laser has now made this possible with physically convenient sources.

An experiment has been carried out in this work, which used a 3mW, 632nm He-Ne laser together with a acousto-optic modulator to replace the LED light source in the system shown in Figure 4.4 and allowed the employment of a fast photodetector. Due to the monochromaticity of the laser source, a long-pass glass filter, RG695 was used which effectively isolated the excitation light and also allowed both the R-line and broadband fluorescence emissions be received by the photodetector, giving an additional advantage in the signal-to-noise ratio condition. The corresponding experimental results are presented in Figure 4.12.

As illustrated in Figure 4.12, the temperature sensitivity of the observed lifetime is greatly enhanced over the higher temperature region by the use of a fast-response photodetector, now used due to the much higher level of fluorescence emission induced by a He-Ne laser. As both the R-line and broadband emissions are received by the photodetector, the decrease in the intensity of the observed emission only occurs beyond ~340°C. The increase in such an intensity with temperature increase from 20°C to ~340°C, is mainly due to the thermal elevated broadband emission as discussed in Chapter 2, and the higher transmittance of the long-pass glass filter (RG695) at the peak wavelength of the broadband emission, than that at the R-lines.

The configurational coordinate model for Cr<sup>3+</sup> fluorescence in a in a high field crystal, described in Chapter 2, has been used to fit the data of the observed lifetime presented in Figure 4.12. The corresponding least squares fitting curve is depicted in solid line in the

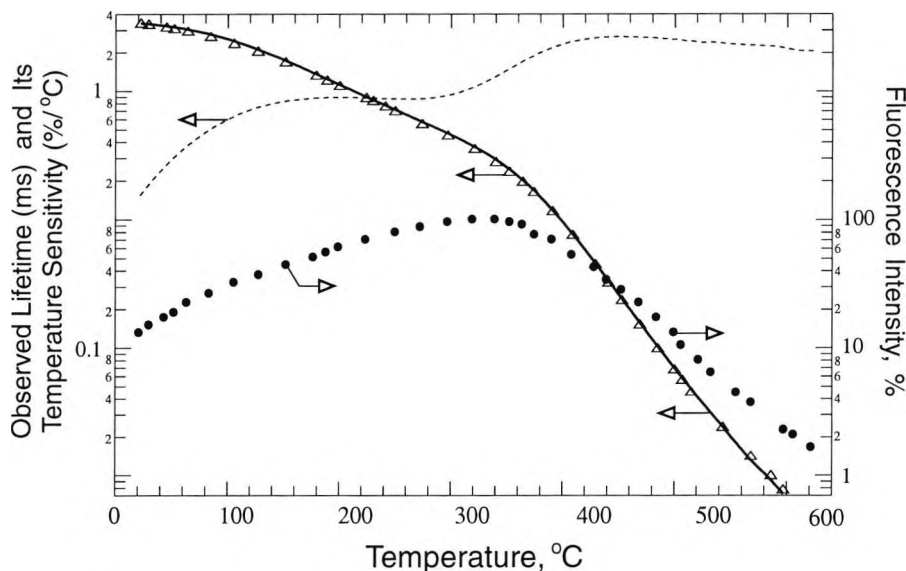


**Figure 4.12:** Thermal characteristics of ruby fluorescence observed by the improved system.  $\Delta \Delta \Delta$ : data for the observed lifetime. **Solid line:** the least squares curve fitted to the lifetime data using the configurational coordinate model for  $\text{Cr}^{3+}$  fluorescence in a high field crystal, presented in Chapter 2. **Dashed line:** the relative temperature sensitivity of the observed lifetime.  $\bullet \bullet \bullet$ : the observed fluorescence emission intensity.

same figure. The deviation of such fitting is 1%. Though such a low deviation is quite enough to support the validity of the model, it is not adequate for the model to be used directly for calibration purposes, for it can only result in a 4°C precision. The discrepancy between the results of the model to the experimental data is mainly due to exclusion of the impact of the phonon-induced transitions which are significant at the lower temperature region, as discussed in Chapter 2. To include the impact of the most prominent phonon energy,  $h\nu = 280\text{cm}^{-1}$  identified in ruby, the expression of the configurational coordinate model given in Eq.(2-10) is rewritten as:

$$\tau = \tau_s \frac{1 + 3 e^{-\Delta E/kT}}{\coth(h\nu/2kT) + \alpha e^{-\Delta E/kT} + \beta e^{-(\Delta E_s + \Delta E)/kT}} \quad (4-4)$$

The deviation of the fitting of the experimental data over the entire temperature is 0.15%, by using Eq.(4-4). This could give a precision of 1.5°C for Eq.(4-4) to be used as calibration formula.

The  $\sigma_T$  vs  $T$  curve of the improved system, calculated by Eq.(4-3) and normalised to its minimum at  $\sim 380^\circ\text{C}$ , is depicted in Figure 4.13. The measurement resolution of the system, defined by  $3\sigma_T$ , is observed to be 0.3°C at 90°C and 1°C at 600°C. Thus, according

to the  $\sigma_T$  vs  $T$  curve in Figure 4.13, over the region from 90 to 530°C the measurement resolution achievable is 0.3 °C and from 60 °C to 600°C it is 1 °C. As a comparison, the  $\sigma_T$  vs  $T$  curve for the previous system is also drawn in Figure 4.13 in dashed line with its values normalised with respect to that for this improved system. It graphically shows that the measurement range of a ruby fluorescence based thermometer system could be greatly extended into higher temperatures by using a much more powerful excitation source.

Intrinsically, the ruby fluorescence lifetime is not suitable for the sensing of temperature below water freezing point (0 °C), for its temperature sensitivity is quite low over this low temperature region. Low sensitivity also limited the performance of the ruby based thermometer system up to ~50 °C. That is why poor measurement reproducibility was found at 40 °C in the system shown in Figure 4.4, where the long-term drift in the time-constant of the entire electronic system, especially that of the high-gain photodetector, could be much higher than the resolvable change in the fluorescence lifetime.

As with all other thermometer systems based on the fluorescence of refractory materials, the highest temperature which could be measured, is limited by the difficulty in the detection of the extremely short lifetime under excessively poor signal-to-noise conditions, caused by low fluorescence efficiency at high temperature. According to the

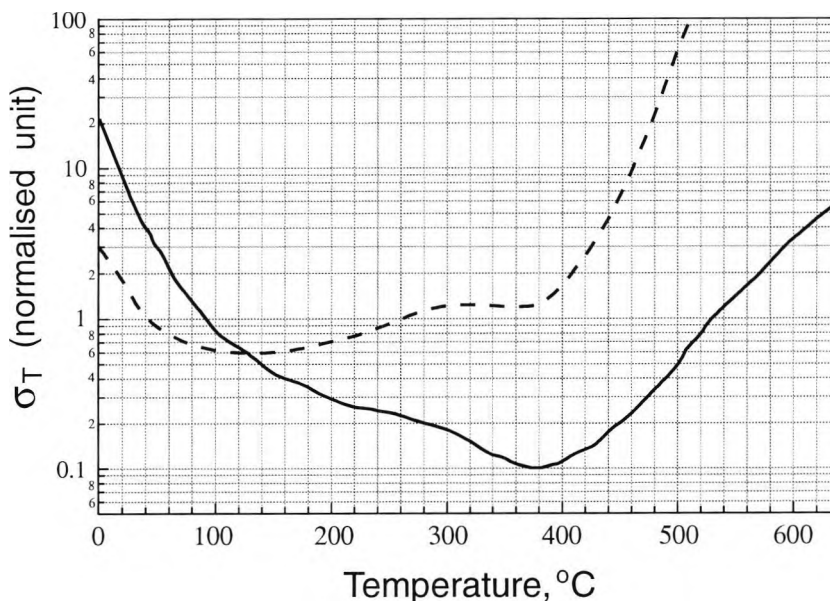


**Figure 4.13:** The calculated temperature measurement deviation of the improved ruby fluorescence thermometer system, in **solid line**. **Dashed line:** that of the previous system presented in Figure 4.11.

data presented in Figure 4.12, at 600°C, the fluorescence intensity is reduced to 0.7% of its maximum value occurring at ~340°C, and the fluorescence lifetime is 1μs, reaching the shortest lifetime which could be detected according to the operational bandwidth of the electronic components employed. A cost-effective solution of further extending the high temperature measurement limit of a fluorescence based thermometer might be found from the use of other fluorescent materials, as demonstrated by the example giving in the following section, which uses alexandrite as the sensing material.

#### 4.4. Alexandrite based thermometer using PLD-PMTR technique with potential range -100 to 700°C

The successful operation of chromium-doped chrysoberyl or alexandrite ( $\text{BeAl}_2\text{O}_4:\text{Cr}^{3+}$ ) by Walling *et al* [51, 73, 74] at room temperature as a tunable laser led to the introduction of the first commercial solid-state laser with wide tunability [75]. Their work also revealed experimentally that the intrinsic fluorescence lifetime of  $\text{Cr}^{3+}$  in chrysoberyl decreases monotonically with temperature from -120 to 220 °C and this can be explained using a two-level kinetic model [51], as mentioned in Chapter 2. This change in the fluorescence characteristics with temperature indicated the possibility of using the fluorescence decay of alexandrite for temperature sensing applications, over the region mentioned above. Many of physical and chemical properties that crystalline alexandrite possesses, making it a good laser host, e.g., hardness, strength, chemical stability, and high thermal conductivity (two-thirds of that of ruby and twice that of YAG), also make it favourable as a temperature transducer material.

The use of fluorescence from alexandrite for temperature sensing was first reported by Augousti *et al* [66, 45]. It had previously been the subject of that low-temperature study, using a low-power LED or a He-Ne laser with rather inefficient modulation accessory made of bulky, high-voltage controlled Pockels cell, as excitation source. This greatly limited the practical utility of the scheme and a comparatively poor signal-to-noise ratio was obtained. The lifetime measurement technique used also imposed a limit on the consecutive measurement range. Using this limited optical system, an accuracy of  $\pm 1$  °C over a range 20-150°C was achieved.

The subsequent development of laser diode sources at low cost, and improved electronic detection, coupled with new probe fabrication techniques have now opened up this field to a study aimed also at high-temperature measurement. In this section, an alexandrite fluorescence lifetime based fibre optic thermometer system, with a visible laser diode as the excitation source is presented, which has achieved a measurement repeatability of  $\pm 1$  °C over the region from room temperature to 700 °C, using the lifetime measurement technique, termed the pulse modulated phase-locked detection with two references (PLD-PMTR) and described in detail in Chapter 3.

#### 4.4.1. Absorption and fluorescence spectra

Figure 4.14 shows the absorption spectrum of alexandrite at room temperature. The main absorption features consist of two broad bands centred at about 420 and 580 nm, three sets of sharp lines centred near 680, 650 and 470 nm, and the band edge appearing below 300 nm (not shown in the figure). The two bands are associated with transitions from the  $^4A_2$  ground state to the  $^4T_2$  and  $^4T_1$  excited states. These transitions involve changes in the crystal-field orbitals of the electrons and thus are highly sensitive to the crystal-field environment of the ion. Vibrational modulation of the field strength produces the broad-bands. The three sets of sharp lines are associated with transitions from the ground state to the split components of the  $^2E$  (R lines),  $^2T_1$  (S lines), and  $^2T_2$  (B lines) levels. These involve spin-flips of the electron wave functions without changes in the crystal-field states. Thus they are insensitive to vibrational modulation of the crystal field and therefore appear as sharp lines<sup>[76]</sup>.

The crystal field strength index,  $D_q/B$  used in Tanabe-Sugano diagram (Figure 2.1), is determined from spectroscopic data<sup>[50, 77]</sup>. The peak of the  $^4A_2 \rightarrow ^4T_2$  absorption band is given by  $10D_q$ , whereas the Racah parameter  $B$  (the inter-electron energy) is obtained from the energy separation between  $^4A_2 \rightarrow ^4T_2$  and  $^4A_2 \rightarrow ^4T_1$  absorption bands. Thus from the absorption spectrum shown in Figure 4.14, the magnitude of  $D_q/B$  in alexandrite is

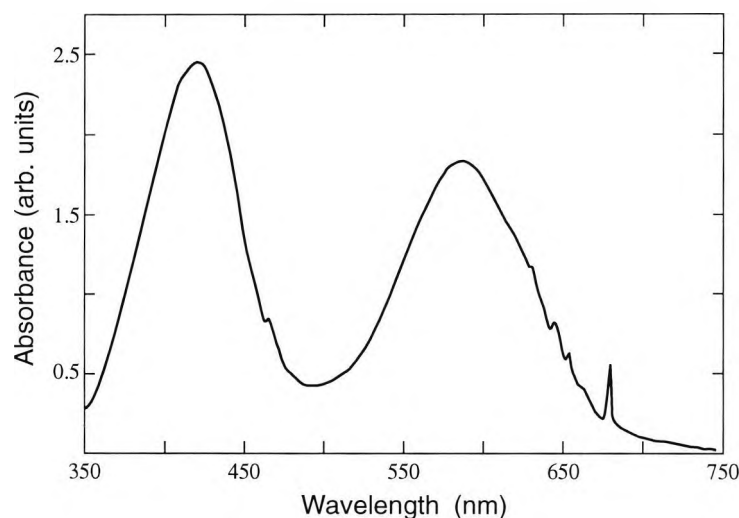


**Figure 4.14:** Absorption spectrum of alexandrite at room temperature.

estimated to be  $\sim 2.6$ . This shows that the crystal-field strength in alexandrite is significantly lower than that of  $D_q/B (=2.8)$  in ruby<sup>[77]</sup>. As quoted in Chapter 2, the energy split between  ${}^4T_2$  and  ${}^2E$  is  $807.5\text{ cm}^{-1}$  in alexandrite and  $2350\text{ cm}^{-1}$  in ruby.

The fluorescence emission from alexandrite at room temperature is shown in Figure 4.15. The major features of the spectrum are the two sharp lines  $R_1$  and  $R_2$  and the broad, structured band peaking at lower energies. The latter is due to the superimposition of low-energy vibronic emission transitions from the components of the  ${}^2E$  level and emission from the relaxed excited state of the  ${}^4T_2$  level which is Stokes-shifted to lower energy compared to the absorption transition involving this level. The structure in this sideband is a mixture of specific one-phonon vibronic peaks, and zero-phonon lines associated with transitions from the  ${}^4T_2$  and  ${}^2T_1$  levels. By comparison to the fluorescence emission spectrum of ruby at room temperature shown in Figure 4.6, the broadband vibronic emission at lower energies is much stronger in alexandrite at the same temperature. This is consistent with the observation that the energy split between  ${}^4T_2$  and  ${}^2E$  in alexandrite is much less than that in ruby as shown by figures quoted above.

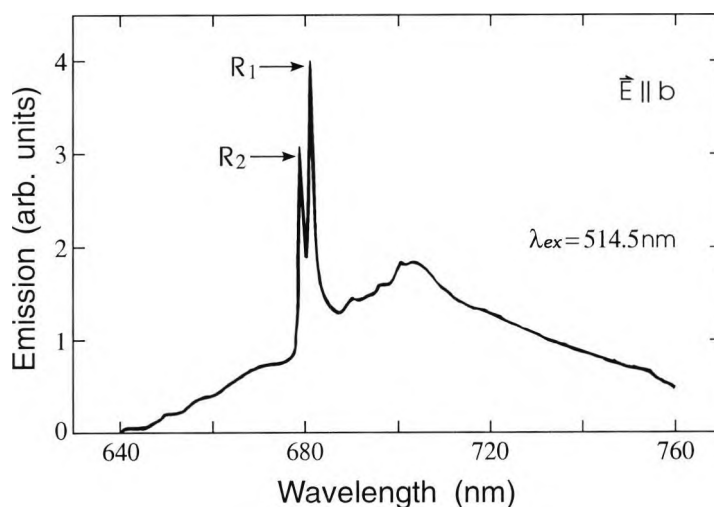


**Figure 4.15:** Fluorescence spectrum of alexandrite at room temperature.  $\lambda_{ex}$ : excitation wavelength. From Powell *et al*<sup>[76]</sup>.

#### 4.4.2. Experimental setup

A schematic representation of the experimental system is shown in Figure 4.16. The modules composing of this system are described below.

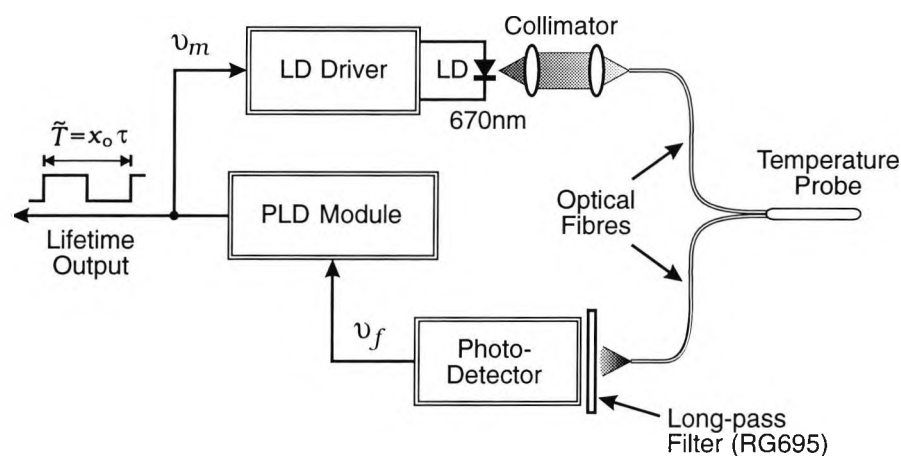


**Figure 4.16:** Schematic of the optoelectronic setup of the alexandrite fluorescence based thermometer. LD: laser diode.

##### 4.4.2.1. Temperature probe

As the probe is expected to be tested and requiring several excursions to temperatures up to 800 °C and higher, the probe fabrication technique illustrated in Figure 4.8 could not be used, for the specified upper operation temperature for the gold-coated fibre is 750 °C. Even if the gold coating of the fibre could tolerate a temperature higher than the specified limit, the severe oxidation would not allow the copper-made assembly *B* and cylinder *A* designed for holding the fibre bundle and sensing material together, as shown in Figure 4.8, to sustain a few excursions to 700 °C. Therefore, the probe used herein has to be fabricated using bare silica fibres at the high temperature part and non-metal refractory material to hold the alexandrite sample, as described in the following.

The configuration of the probe is as shown in Figure 4.17. The sensor element itself, a small (approximately) rectangular-shaped (2×2×1 mm) piece of synthetic crystal alexandrite, is held in a ceramic enclosure at the end of two fused silica fibres. The first fibre, that with a 0.4 mm core diameter, is used to transmit light from the excitation source to the sensor element. The second fibre, with 1.0 mm core diameter, is used to receive the

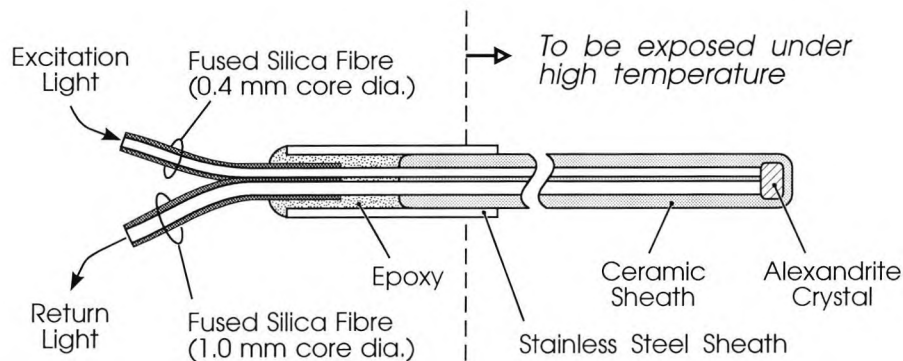


**Figure 4.17:** Schematic of the optical fibre probe.

fluorescence response emitted from the sensor element. This geometrical arrangement allows the collection of a sufficient level of fluorescence signal from the sensing material to allow processing to be undertaken. To allow for operation at temperatures higher than 150 °C, parts of the optical fibres, which are to be exposed under high temperatures, have to be stripped of their outer jacketing and encased with the crystal in a ceramic sheath. The stainless sheath, shown in Figure 4.17, is used with epoxy to strengthen fibres at the joint of the fibre jacket and the ceramic sheath, which is extremely fragile to bending.

#### 4.4.2.2. Excitation source and fluorescence detection

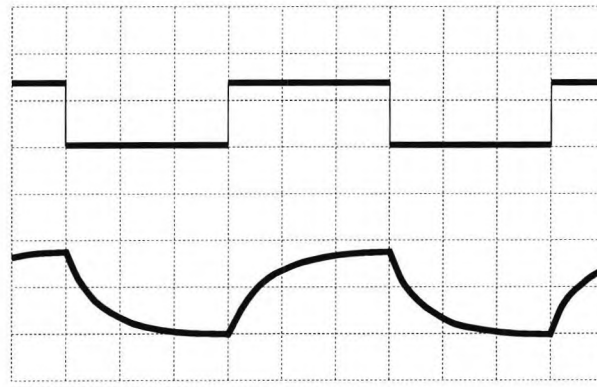
A 3 mW laser diode with peak emission wavelength at 670 nm was used as a pumping source in this work. As seen from Figure 4.16, a PLD technique is used for the measurement of the fluorescence lifetime and, hence the output light intensity of the laser diode is electrically, modulated in a square wave fashion. The output of the laser diode is coupled into the first fibre mentioned above using collimating lens, giving a coupling efficiency of more than 50%. Though the alexandrite absorption spectrum spans the wavelength region from about 380 to 680 nm, as shown in Figure 4.14, the absorption coefficient at 670 nm is rather low compared to that at 633 nm, the He-Ne laser wavelength used in the work of Augousti *et al*<sup>[66]</sup> (1987). However, due to the high coupling efficiency and no external modulation accessory used, which could introduce additional loss in light intensity, the intensity of the excitation light being finally delivered to the alexandrite sample is much higher than in that previous work. It ensures the detected fluorescence signal-to-noise ratio is high enough to be measurable, when the temperature is raised 750 °C.

At the fluorescence detection stage, the return light from the second fibre mentioned above (Figure 4.17) consists of not only the induced fluorescence response, but also some reflected excitation light at 670 nm. As illustrated in Figure 4.16, a long-pass glass filter (RG695), with a cut-off wavelength at 695 nm, is used to prevent the reflected excitation light from entering the photodetector (BPX65), a silicon PIN photodiode with 1mm<sup>2</sup> active area. In this arrangement, the strong *R*-line emission observed at room temperature, as shown in the alexandrite fluorescence spectrum in Figure 4.15, has to be excluded from the input light to the photodetector, for the wavelengths of these emissions are too closely located to that of the excitation light; and only the broadband emission centred at lower energy is to be detected, for the sake of good isolation of the excitation light. As shown in Figure 4.15, the intensity of the integrated low energy broadband emission at room temperature already matches that of the *R*-lines, and it is expected to be elevated with temperature increase. Therefore the loss in the fluorescence intensity due to the exclusion of the *R*-lines emission, will not cause serious reduction in the signal-to-noise ratio in the final output of the detected fluorescence signal at room temperature and beyond.

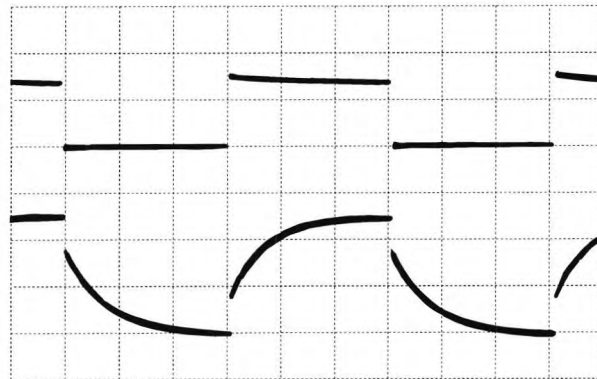
However, as the glass filter has a transmittance of about 0.01 % at 670 nm, there is still some excitation light which leaks through. Such an excitation leakage is clearly revealed from the illustration of the waveform of the photodetector output, the lower trace in Figure 4.18(b). Compared with that in Figure 4.18(a), this waveform shows that a small fraction of excitation light is superimposed on the fluorescence response. However, the excitation light leakage is low enough to allow the fluorescence signal to be sufficiently amplified without causing a saturation problem.

#### 4.4.2.3. Signal processing

The significant presence of excitation leakage in the received fluorescence signal, shown in Figure 4.18, prevents the use of the PLD-PMSR technique, which has been successfully applied to the ruby based system described before, in the application discussed here, for it will severely impair the performance of the system, according to the discussion in Chapter 3. So the "anti-leakage" PLD-PMTR scheme is the best choice for this application. Moreover, the pulse profile of the laser diode output is not an ideal rectangular one, as shown by the upper trace of Figure 4.18(b); thus the use of the rising part of the fluorescence emission, shown by the lower trace of Figure 4.18(b), should be avoided in



(a)



(b)

**Figure 4.18:** (a) Ideal temporal profiles of excitation light and fluorescence emission. **Upper trace:** modulation signal applied to the laser diode. **Lower trace:** fluorescence emission signal. (b) Actual temporal profiles of excitation light and fluorescence emission received with leakage of excitation light. **Upper trace:** the intensity of the square wave modulated light output of the laser diode. **Lower trace:** fluorescence emission signal received showing leakage of excitation light.

producing the lifetime measurement. Therefore the single sided PLD-PMTR technique presented in Chapter 3 was used in the production of the PLD module shown in Figure 4.16. Indeed, the PLD-PMTR scheme was first proposed with the application to this alexandrite fluorescence based thermometer system.

#### 4.4.3. Experimental results

The output of the system is calibrated against a conventional type K thermocouple by placing the probe in a well-insulated electric oven with thermostatic control to a 0.5 °C resolution. A calibration curve, resulting from using a laser diode with 670 nm lasing wavelength as the excitation source, is depicted in Figure 4.19, drawn with the ordinate having a logarithmic scale. The relative temperature sensitivity of the fluorescence lifetime

is calculated using Eq.(4-1) based on these observed lifetime data, and is depicted as a function of temperature as the dashed line in Figure 4.19.

For comparison with the case with a possible higher degree of excitation leakage, the data taken with the use of a 655 nm laser diode, are also presented in Figure 4.19. In this case, the excitation light leakage to the detector stage is only tenth of that when a 670 nm laser diode is used. It shows that with the use of the anti-leakage PLD-PMTR signal processing scheme, such a great difference in excitation leakage does not introduce a significant difference in the fluorescence lifetime measured.

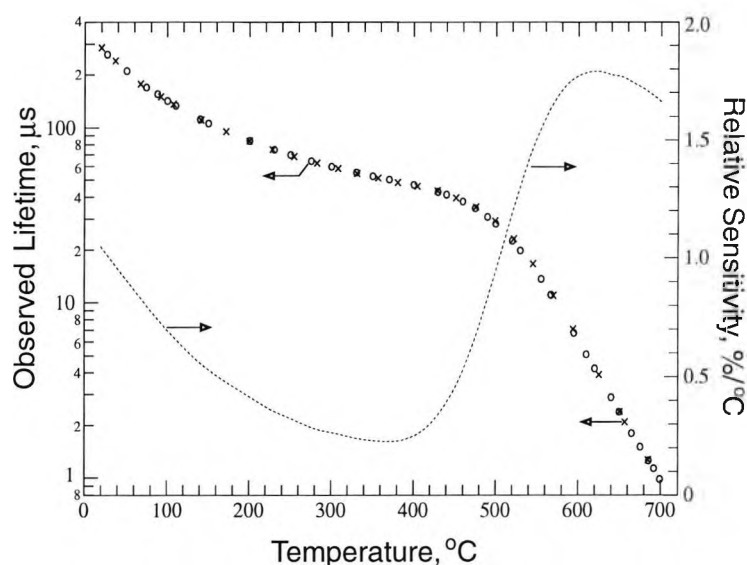


**Figure 4.19:** Observed alexandrite fluorescence lifetime vs.. temperature. o o o: data taken in the case of using 670 nm laser diode. x x x: data taken in the case of using 655 nm laser diode. ----: relative temperature sensitivity of the observed lifetime.

The intensities of the fluorescence signal received in the system using a 670 nm laser diode as excitation source are also recorded during the calibration process. The data are graphically presented in Figure 4.20 against the temperature. This show that the fluorescence intensity increases dramatically with temperature increase from room temperature or below to 400 °C and reaches its maximum at ~430 °C. Thus, though the temperature sensitivity of the lifetime decreases with temperature increase over this temperature region quite sharply, the measurement error would not be expected to increase correspondingly in an inverse method. This is illustrated explicitly by the calculated measurement deviation vs. temperature curve depicted in Figure 4.21, which is normalised to its minimum value

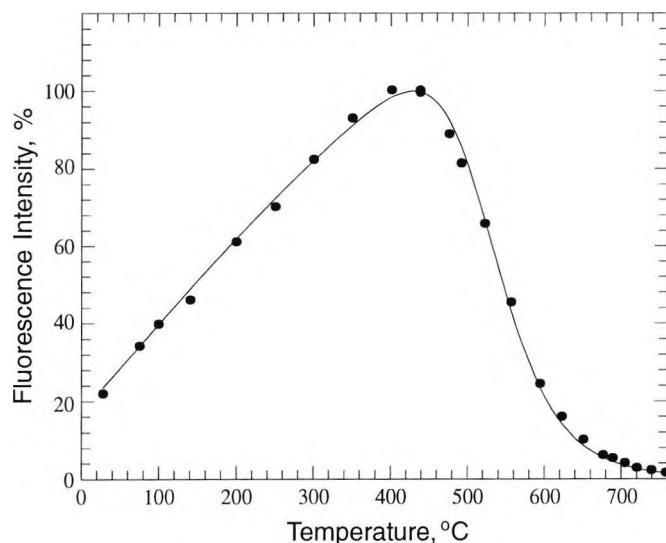


**Figure 4.20:** Alexandrite fluorescence intensity vs.. temperature. •••: data for fluorescence emission at low energy broadband ( $\lambda > 695\text{nm}$ ) induced by 670nm laser diode.

at  $\sim 520\text{ }^\circ\text{C}$  and shows that the measurement deviation does not change significantly over the region  $20 - 400\text{ }^\circ\text{C}$ . As shown in Figure 4.21, the system could have optimum performance over the measurement regions around  $100\text{ }^\circ\text{C}$  and  $520\text{ }^\circ\text{C}$ . This is consistent with the observation of the systems in the region  $20 - 725\text{ }^\circ\text{C}$ , which shows the measurement deviations at  $\sim 100\text{ }^\circ\text{C}$  and  $\sim 500\text{ }^\circ\text{C}$  are better than  $0.2\text{ }^\circ\text{C}$  and that at  $725\text{ }^\circ\text{C}$  is  $1\text{ }^\circ\text{C}$ .

As mentioned in Chapter 2, the configurational coordinate model for  $\text{Cr}^{3+}$  fluorescence in high fields, described in Section 2.3.2, was used to fit to the alexandrite fluorescence lifetime data ranging from  $20$  to  $\sim 650\text{ }^\circ\text{C}$ . The standard deviation of the fitting errors of the lifetime is  $0.3\%$ . This is equivalent to a temperature fitting error of  $1\text{ }^\circ\text{C}$  and matches the resolution of the calibration equipment used quite well. Therefore, a precision of such an order could be expected should this model be used as calibration formula over the above region.

The probe has sustained several temperature excursions to  $800\text{ }^\circ\text{C}$  and no significant changes in its characteristics were observed. However, due to the extremely poor signal-to-noise ratio condition and the short medium lifetime, no meaningful measurement of the fluorescence lifetime could be made at temperatures beyond  $760\text{ }^\circ\text{C}$  using the system with the present setup, shown in Figure 4.16. As illustrated in Figure 4.21, the measurement error at  $700\text{ }^\circ\text{C}$  is estimated to be already 10 times higher the minimum value, and so it is

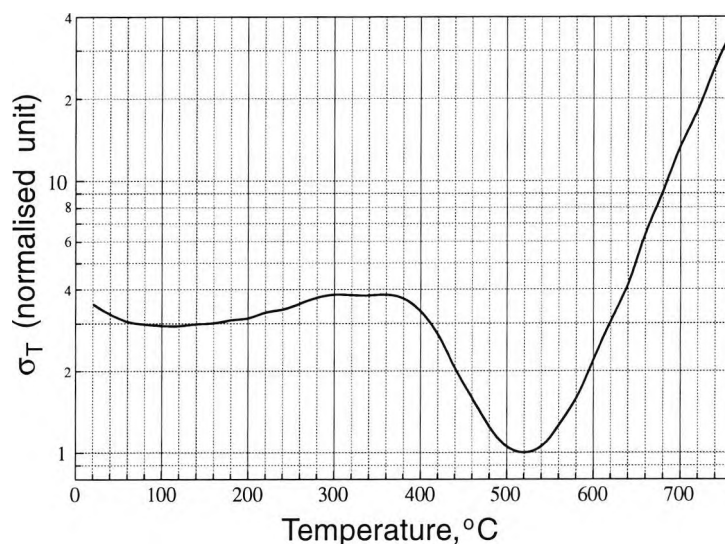


**Figure 4.21:** Calculated temperature measurement deviation of the alexandrite based thermometer system, depicted as a function temperature.

considered proper to specify the upper limit of the measurement range of the system as 700 °C.

#### 4.4.4. Potential for applications down to -100°C

As illustrated by the experimental data of Walling *et al*<sup>[51]</sup>, the decrease in the alexandrite fluorescence lifetime with increasing temperature starts from the temperature lower than -120 °C. Since the calculation shows the extrapolated temperature sensitivity of the lifetime is still as high as 0.8 %/°C at -100 °C, the measurement range of the alexandrite based sensor system could be extended to the lower-temperature region, to reach -100 °C. However, the difficulty is that the intensity of the total fluorescence, including that of the *R*-line emission induced by a 670 nm diode laser, will be reduced to only ~4 % of its peak value at ~400 °C on the basis of the extrapolation from the experimental data presented in Figure 4.20. This would have a consequent reduction in the signal-to-noise ratio which would undermine the useful performance of the sensor.

Using a typical He-Ne laser source, the extrapolated intensity of the total fluorescence that can be obtained at -100 °C is still higher than 30 % of the peak value, and the corresponding absorbance of alexandrite at 632.8 nm is estimated to be ~ 45 times higher at that wavelength than at 670 nm. Therefore, in temperature sensing applications down to

-100 °C, a better alternative is to substitute a 635 nm laser diode as source, which is now commercially available at a reasonable cost, for the 670 nm diode used. This will also involve a minor change of the long-pass optical filter (Figure 4.16) to substitute one with a shorter cut-off (e.g., RG665 Schott glass) instead of the RG695 (Schott glass), so that the strong R-line emissions occurring at lower temperature can also be detected by the photodetector and the signal intensity can be greatly enhanced.

## 4.5. Cr:LiSAF based thermometer for biomedical applications

### 4.5.1. Application background

Benign Prostatic Hyperplasia (BPH) is a common condition amongst the ageing male population. It is estimated that 75 % of men over the age of 50 years have symptoms arising from BPH, the most prominent of which is urethral obstruction. In the past, treatment of the condition has required surgical intervention; but during the 1980s local hyperthermia was tried as a candidate solution for more conservative therapy. The effect of heat treatment (normally at 43 to 45 °C for one hour duration) is to cause the prostate gland to shrink, which eventually produces a reduction in urethral pressure. As this pressure reduces, the obstruction is cleared and urine can flow freely once more.

The heat source for the above treatment stems from an externally applied radio frequency (RF) field (434 MHz). It is extremely important to monitor the effective internal temperature during treatment, as there are physiological structures which surround the prostate and are prone to heat damage, e.g. the sphincter muscles. Current technology uses thermocouples mounted in an indwelling catheter as the temperature sensing element. A disadvantage of this measurement system is that the RF field interferes with the monitored signal from the thermocouple, so it must be switched off during the measurement period (once every 15 seconds). An advantage of replacing the thermocouples with an optical thermometer is that it is inert to applied RF fields. This allows for continuous monitoring of temperature, together with the application of an un-pulsed external RF field as the heat source. As a consequence of this change in measurement technology, a further feature of the system is that it enhances patient safety.

For the convenience of planting the temperature sensing element with the RF applicator for heat treatment for BPH, an optical temperature probe with a fibre optic configuration is required. As reviewed in Chapter 1, there exists a variety of such temperature sensing schemes. Among them, the scheme based on the detection of fluorescence lifetime which this thesis work concerns, is most applicable to clinical applications. First of all, the monitoring of temperature using the fluorescence lifetime of appropriate materials has a significant advantage in that it is independent of the accurate measurement

of light intensity. Therefore, the corresponding fibre optic probe can be free of the impact of fibre sterilising processes and fibre bending as well as reconnecting, and be potentially robust enough for harsh day-to-day usage. Second, there are a number of chemically stable fluorescent materials, of which the fluorescence lifetimes are highly sensitive to temperature variance over the biomedical temperature region and which could have the potential for such a thermometric application. The temperature dependence of the alexandrite fluorescence lifetime over the region 20 - 80 °C illustrated in Figure 4.19, shows alexandrite could be used for this application. However, in this thesis work, it is that the trivalent-chromium ion doped material, LiSrAlF<sub>6</sub> (Cr:LiSAF) which is more favourite for this application, due to both the temperature sensitivity of its fluorescence lifetime over the biomedical application region and its other optical properties which give advantages in the design of the thermometer system. This will be illustrated by the following discussion, which describes a fibre optic thermometer based on the Cr:LiSAF fluorescence lifetime developed in this thesis work, and the corresponding test undertaken in the clinical RF heat treatment environment.

#### 4.5.2. Absorption and emission spectra of Cr:LiSAF

The crystal structure of LiSrAlF<sub>6</sub> (LiSAF) is related to that of the colquiriite mineral LiCaAlF<sub>6</sub><sup>[37]</sup> (Payne et al, 1989a). The host is uniaxial and contains a single type of Al site. The  $\pi$  (E || c) and  $\sigma$  (E  $\perp$  c) absorption and emission spectra of Cr<sup>3+</sup> in LiSAF are shown in Figure 4.22. The basic features in the absorption spectra involve three broad bands. From longer to shorter wavelengths, they are assigned as the  $^4A_2 \rightarrow ^4T_2$ ,  $^4T_{1a}$  and  $^4T_{1b}$  transitions. The sharp features superimposed on the  $^4T_2$  band arise from the  $^2E$  and  $^2T_1$ .

The fluorescence emission spans the wavelength region from 700 nm to 1100 nm with the peak at 825 nm, as shown by the emission spectra drawn in Figure 4.22. It is within the most effective detection region of an ordinary silicon PIN photodiode. Such a broadband emission is due to the  $^4T_2 \rightarrow ^4A_2$  transition, or the inverse of the transition which gives rise to the first absorption band.

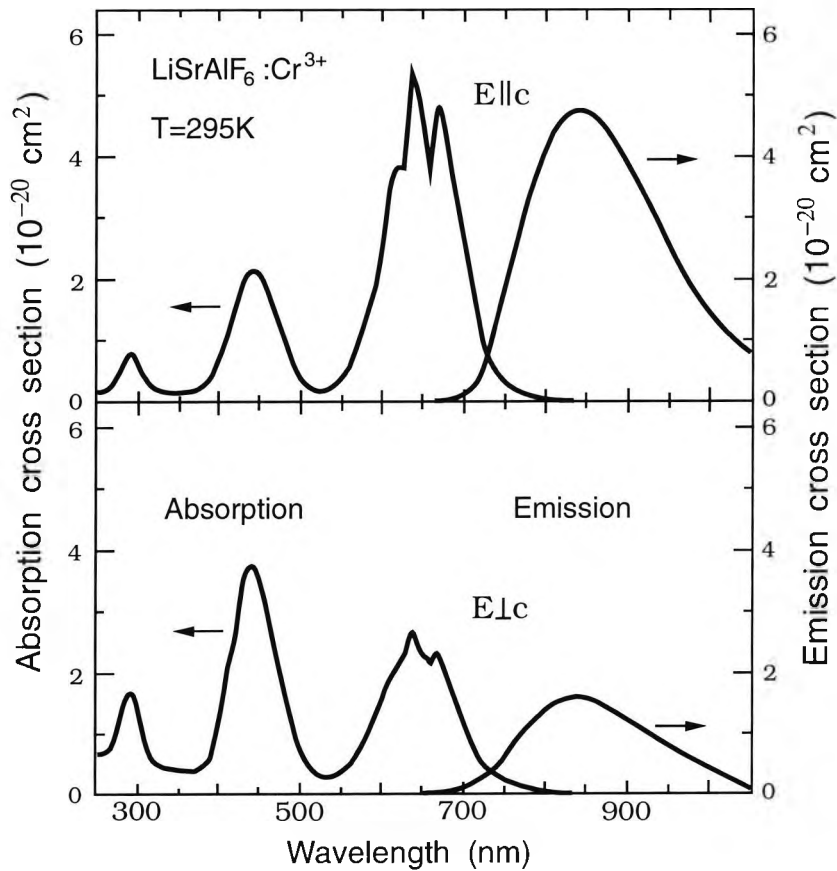


**Figure 4.22:** Polarised absorption and emission spectra of  $\text{LiSrAlF}_6:\text{Cr}^{3+}$  from Payne *et al* [37].

From the absorption spectra shown in Figure 4.22, the magnitude of the crystal field strength  $D_q/B$  in LiSAF is estimated to be  $\sim 2.0$ . It indicates that LiSAF is of low crystal field strength. This is verified by the sharp feature appearing at  $\sim 670$  nm ( $14925$   $\text{cm}^{-1}$ ) in the absorption spectra and corresponding to the  ${}^2E$  state, and the zero-phonon line of  ${}^4T_2 \rightarrow {}^4A_2$  with an energy of  $14296$   $\text{cm}^{-1}$  identified by Payne *et al* [53] in the emission spectrum at 28K.

### 4.5.3. Experimental set-up for clinical test

Figure 4.23 is a schematic representation of the Cr:LiSAF fluorescence lifetime-based thermometer. The absorption spectrum of Cr:LiSAF spans the wavelength region from the ultra violet (UV) to near 750 nm with a peak falling between 600 nm and 700 nm, as depicted in Figure 4.22, and thus a visible laser diode with a lasing wavelength at 670 nm (and 1 mW of optical power output) can efficiently excite or ‘pump’ the Cr:LiSAF sample used as sensor element, to induce a fluorescence response from it with a sufficiently high signal-to-noise ratio to be detected. As shown in Figure 4.23, the isolation of

excitation light at the fluorescence detection stage is provided by a glass filter, type BG3. The BG3 glass filter has a long-pass band starting at  $\sim 720$  nm, and this well matches the Cr:LiSAF emission spectrum shown in Figure 4.22. Indeed, due to the clear separation between the excitation light and fluorescence emission in wavelength terms, little compromise has been made between efficient transmission of fluorescence and good isolation of excitation light at the detector stage. This is a near perfect optical arrangement and a much higher signal-to-noise ratio is obtained, compared to those in the cases of the ruby and alexandrite based systems discussed before.

Though no significant excitation light leakage was present in the received fluorescence signal, the pulse profile of the laser diode output is not ideally rectangular as in the case of the alexandrite based scheme. Thus the single-sided PLD-PMTR technique is employed to form the PLD module in this thermometer system, so that the lifetime measurement is produced only using the decay part of the fluorescence signal. To make comparisons, the PLD-PMSR technique used in the ruby based scheme and the PLD-PMTR technique using both the rising and decaying parts of the fluorescence signal were also tried in this system. It shows that much better measurement repeatability could be achieved from the use of the single-sided PLD-PMTR technique.

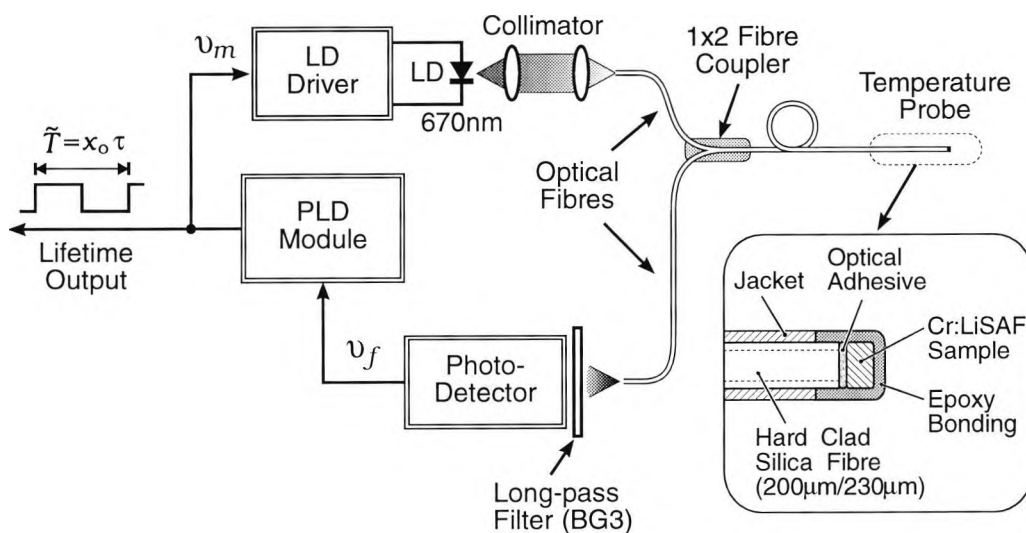


**Figure 4.23:** Schematic of the Cr:LiSAF fluorescence based thermometer.

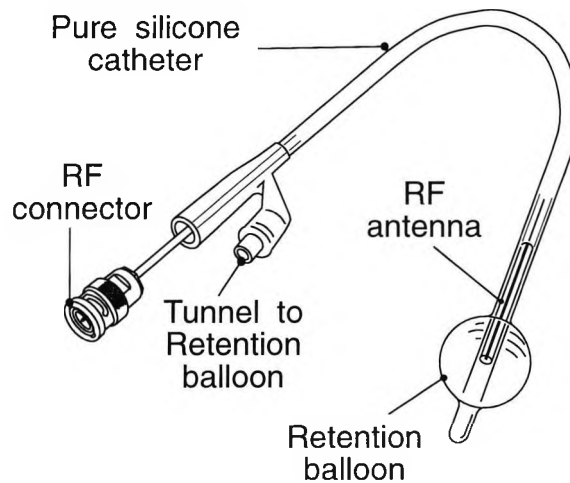


**Figure 4.24:** The configuration of the RF applicator.

The construction of the temperature probe is also depicted in Figure 4.23. The size of the Cr:LiSAF sample is about  $0.4 \times 0.3 \times 0.4 \text{ mm}^3$ , although this is not critical. It is housed, using optical adhesive, on the sensor port of a 1x2 bi-directional fibre coupler made from  $200 \mu\text{m}$  hard-clad silica fibre. With the outer plastic coating, the total diameter of the fibre used is about 0.6 mm.

The configuration of the clinical RF applicator is depicted in Figure 4.24. The RF antenna is placed in a pure silicone catheter which is to be planted at the location of the prostate. The retention balloon near the end of the catheter is used to help secure the position of the RF antenna. Its inflation or deflation is controlled through an air tunnel in the wall of the catheter, of which the entrance is indicated in Figure 4.24. To monitor the temperature of the tissue under RF treatment, the temperature probe is placed in the catheter along with the RF transmission cable and with the position of the sensor tip at the point with maximum RF power output.

#### 4.5.4. Experimental results

The calibration of the thermometer was undertaken in a water bath over the region 0 -  $100 \text{ }^\circ\text{C}$ . The data for the fluorescence lifetime are plotted against temperatures in Figure 4.25, together with its relative temperature sensitivities calculated using Eq.(4-1). It shows that the Cr:LiSAF fluorescence lifetime decreases monotonically with the temperature

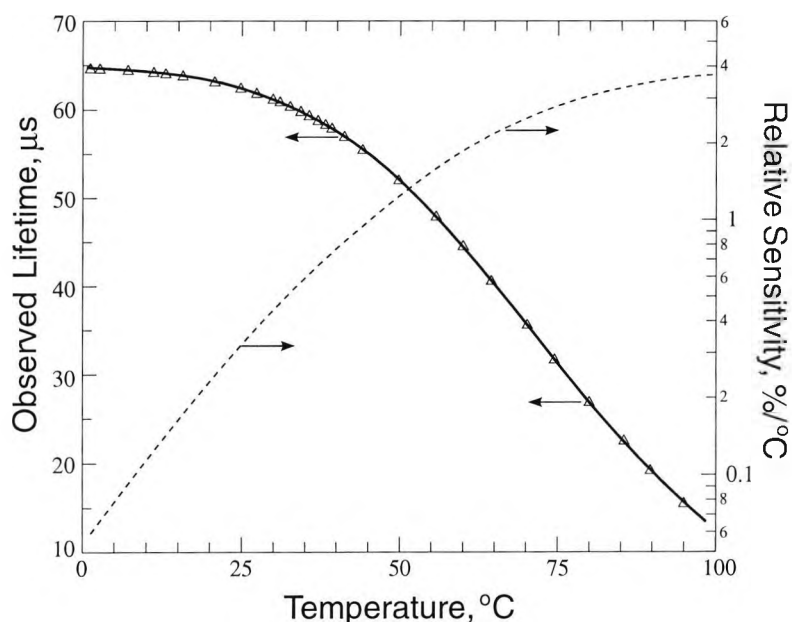


**Figure 4.25:** The observed lifetime of the Cr:LiSAF fluorescence decay and its temperature sensitivity.  $\Delta\Delta\Delta$ : data for the observed lifetime. **Solid line:** curve fitting to the data. **Dashed line:** the relative temperature sensitivity of the observed lifetime.

increase, although it is rather insensitive to temperature variance around 0 °C or below. From about 5 °C, the fluorescence lifetime drops more and more sharply with temperature increase. This is seen explicitly from the rapid increase in its temperature sensitivity with temperature increase. It reaches 0.60 %/°C at 35 °C, and the significance of such a sensitivity increase is clear from a comparison to the case of ruby, which has once been proposed for biomedical thermometric uses<sup>[18]</sup>, and its temperature sensitivity is only ~0.26 %/°C at the same temperature. The fluorescence intensity recorded also decreases with the temperature increase as shown in Figure 4.26, and this would be expected according to the configurational coordinate model for the Cr<sup>3+</sup> fluorescence in low strength fields described in Chapter 2.

The standard deviations of consecutive measurements at some typical temperature points, the values of the corresponding lifetimes and as well as the temperature sensitivities are listed in Table 4.2. The normalised deviation curve calculated using Eq.(4-3) is drawn in Figure 4.27 and is close to the profile of the data in Table 4.2. The measurement repeatability of the system is observed to be better than 0.1 °C at 20 °C. Therefore with

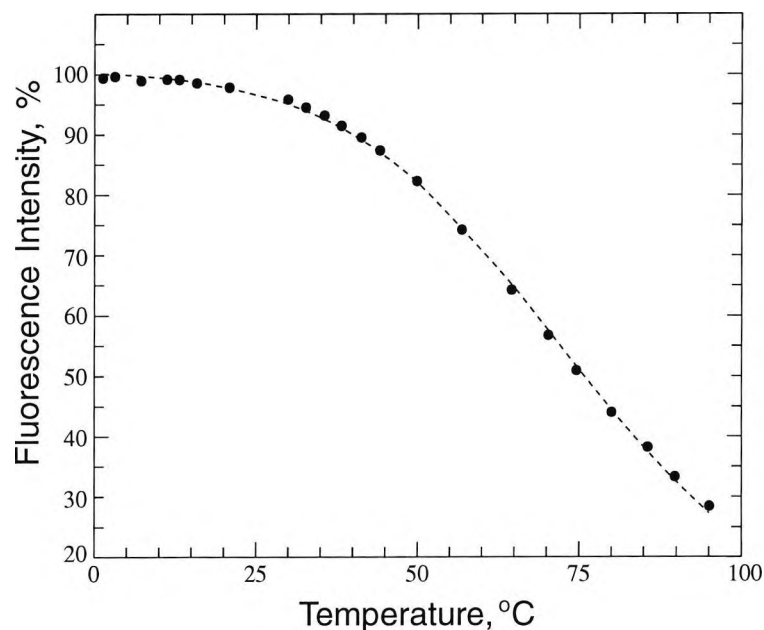


**Figure 4.26:** The Cr:LiSAF fluorescence intensity recorded in this system. ●●●: data for the fluorescence intensity. Dashed line: curve fitting to the data.

**Table 4.2:** The observations of the consecutive measurements made in the laboratory.

Temperature °C	Observed Lifetime, $\mu\text{s}$	Sensitivity %/°C	$\sigma_{n-1}$
20	63.24	0.24	0.05 °C
35	59.63	0.60	0.02 °C
40	57.62	0.75	0.015 °C
50	52.00	1.25	0.01 °C
60	44.64	1.87	0.008 °C

reference to the error vs temperature curve in Figure 4.27, a precision in such an order could be achieved over the region from 20 to ~135 °C by this thermometer system.

As mentioned in Chapter 2, the configurational coordinate model for  $\text{Cr}^{3+}$  fluorescence in low strength fields has been applied to fit the Cr:LiSAF fluorescence lifetime over the region 27 - 80 °C (300 - 353 K), and the deviation of the fitting errors is 0.12 %. Such

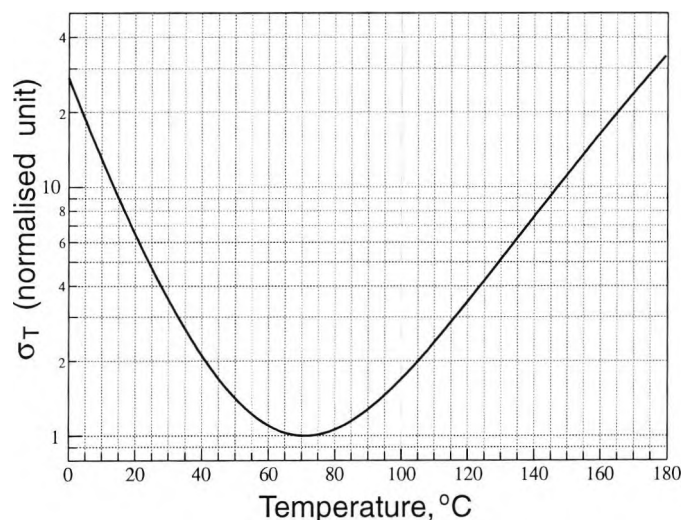


**Figure 4.27:** Calculated temperature measurement deviation of the Cr:LiSAF based thermometer system. The part beyond 100 °C is extrapolated using the configurational coordinate model for Cr<sup>3+</sup> fluorescence in low strength fields.

a close agreement indicates that a precision of 0.2 °C could be provided by the use of this model in the calibration of the corresponding thermometers. A precision like this is more than adequate for the applications discussed here where temperature need to be resolved to ~ 1 °C.

The intrinsic response time of the thermometer is less than 1 second. However when in use, as the temperature probe is separated from the treated tissue by the catheter wall, of which the thickness is ~1mm, and so the temperature indicated by the probe is expected to lag behind the tissue temperature change during the heating up process. To monitor the effect of such lag, an experiment was carried out to measure the total response time of the probe inside the catheter, by applying a step change of temperature outside the catheter from 25 °C to 45 °C. The thermometer indicated 43 °C (corresponding to 90 % of the change) 10 seconds after the step change and this is taken as an indication of the value of the total response time of the **whole** system.

#### 4.5.5. Further considerations in the application

For safety reason, the output power of the RF applicator is reduced so that the heating up from 37 °C to 45 °C takes about 3 minutes, that is the average heating rate is ~1 °C in 20 seconds. With the 10 seconds total response time discussed, the thermometer in the

catheter can follow the temperature change to less than 0.5 °C. This difference is quite insignificant in this application. If for some reason the temperature need be monitored more closely, the temperature probe could be placed outside the catheter so that the sensor part can be directly in contact with the treated tissue. To do so, further measures should be undertaken to ensure the patient's safety. For instance, the material for the plastic coating of the sensor is not expected to have an irritating or toxic effect on human tissue, and it should also be robust enough to sustain clinical uses, even though no toxic effect has been reported or is expected in connection with Cr:LiSAF, an inert sapphire-like based material.

Although the optical temperature probe is immune to the effect of the RF field, the electronic system of the thermometer does pick up some RF interference. Without metal-plate shielding, a previous model of this kind of thermometer could still work properly in the environment of an 434 MHz RF field. It started to malfunction when the RF frequency was tuned beyond 2 GHz. Such an RF pick-up problem has been solved in a later model by shielding the electronics of the instrument in a iron box of ~2 mm thickness and using a RF de-coupling socket for the mains supply of the equipment, a series of easy-to-imple-ment precautions.

## 4.6. Discussion

Since Cr<sup>3+</sup> impurity is nearly always situated in octahedral sites, the absorption and emission spectra are similar in a large variety of materials, the main distinction being the strength of the octahedral field, rather than its exact nature<sup>[53]</sup>. This is well demonstrated by the absorption and emission spectra of ruby, alexandrite and Cr:LiSAF, the materials used here. The absorption spectra at lower energies are all characterised by two broadbands corresponding to the  $^4A_2 \rightarrow ^4T_1$  and  $^4A_2 \rightarrow ^4T_2$  transitions, with the positions of the peaks changing according to the field strength. The emission spectra are formed by broadband emissions in the infrared region mainly due to the  $^4T_2 \rightarrow ^4A_2$  transition, with or without the sharp R-line emission related to the  $^2E \rightarrow ^4A_2$ . The positions of the peak emissions and the presence of the R-lines are again determined by the field strength.

The existence of a strong absorption band, at low energy region that corresponds to the  ${}^4A_2 \rightarrow {}^4T_2$  transition, allows the use of a great variety of diode light sources, especially, the powerful visible laser diodes recently developed. This is one of the significant advantages of the use of  $\text{Cr}^{3+}$  activated materials in the development of fluorescence based thermometers.

An additional advantage could also be provided by the similarities in the absorption and emission spectra among the  $\text{Cr}^{3+}$  doped materials, that is the exchangeability of the optical arrangement of the thermometer system with different sensing materials in the  $\text{Cr}^{3+}$  doped family. For instance, an substantial absorption coefficient at around 635 nm could be seen in the absorption spectra of ruby, alexandrite and Cr:LiSAF. Therefore an optical arrangement, which uses an 635 nm visible laser diode as the excitation source and an RG665 long-pass schott glass filter for the isolation of the excitation light, could be employed effectively for all thermometer systems which use the sensing materials mentioned above.

As demonstrated by the examples presented in this chapter, the fluorescence lifetime of a  $\text{Cr}^{3+}$  doped high field strength materials, e.g., ruby and alexandrite, is substantially sensitive to temperature variance over a wide region, within which the lifetime is long enough to be detected by non-special electronic circuitry and the fluorescence intensity could maintain a satisfactory level of signal-to-noise ratio for such detection. The fluorescence lifetime of a low field strength material, e.g., Cr:LiSAF is highly sensitive to temperature change within a limited region, and is particularly useful for thermometric applications which requiring higher measurement sensitivity over a narrow temperature region. The mechanisms involved in such temperature dependences could be explained by the configurational coordinate models presented in Chapter 2.

The PLD techniques discussed not only have a powerful noise suppression ability as illustrated by the simulation experiment in the assessment of the ruby based system, but also can cover a wide consecutive measurement range. In the alexandrite based system, the dynamic range of lifetime measurement covered is 300:1 (from 300  $\mu\text{s}$  to 1  $\mu\text{s}$ ), while in the ruby based system, the dynamic range achieved is up to 3500:1 (from 3.5 ms to 1  $\mu\text{s}$ ).

Such a wide dynamic range is difficult to achieve by a conventional method which uses a fixed frequency for the modulation of the excitation light.

The excitation leakage, a former problem in the PLD schemes, is overcome by the introduction of the PLD-PMTR technique. This is illustrated by the experiment carried out in the case of alexandrite and showing two identical lifetime vs temperature curves obtained with the presence of excitation leakage at two rather different levels respectively. The measurement reproducibility is further enhanced by the use of the single-sided PLD-PMTR technique. This latter scheme would even allow the use of a high power, "delta shaped" pulse laser as the excitation source, provided that it can be modulated with a continuously varying frequency, from perhaps the newer generation of laser systems.

Apart from the physical properties of the materials of which the fibre probes are made, one of the major obstacles to the extension of the measurement range to higher temperatures is the shortening of the fluorescence lifetime. As shown in figure 4.28 for the  $\text{Cr}^{3+}$  doped cases, even though the intrinsic temperature sensitivity of the lifetime could be much higher, the actual sensitivity of the observed lifetime is greatly reduced at high temperatures where the magnitude of the intrinsic lifetime is close to that of the time-constant of

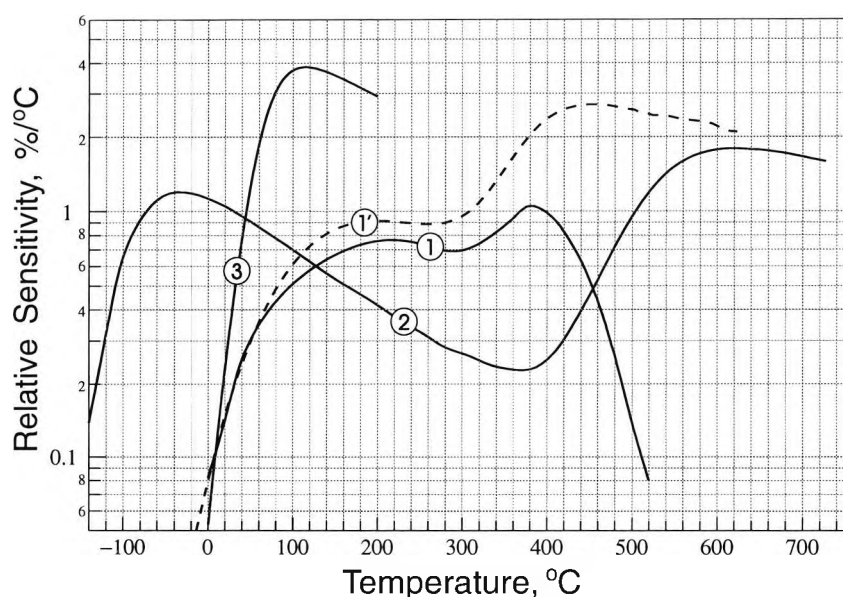


**Figure 4.28:** Relative temperature sensitivities of the observed fluorescence lifetimes of various materials. 1: for ruby observed by the system using a green LED as excitation source and characterised with long time-constant; 1': for ruby observed using He-Ne laser excitation; 2: for alexandrite; 3: for Cr:LiSAF.

the entire electronic system. However, this is not a problem inherent to the PLD schemes alone. The other major obstacle, obviously, is the poor signal-to-noise ratio condition due to the dramatic decrease in the fluorescence intensity.

The lowest temperature at which a fluorescent material could still have thermometric use may be determined by the temperature sensitivity of its fluorescence lifetime. However, the bandwidth of broad absorption bands in the absorption spectrum will contract with the peak wavelengths shifting towards shorter wavelengths, as observed by McClure<sup>[78]</sup> in the case of ruby. Consequently absorption coefficients at the wavelengths situated on the low energy edge of a strong absorption band, such as those corresponding to the lasing wavelengths of various laser diodes available nowadays, would decrease with the decrease in temperatures. Thus, though the quantum efficiencies of most Cr<sup>3+</sup> doped materials are near unity at low temperatures, the intensities of the fluorescence induced by using the above excitation sources would decrease with the temperature decrease, as illustrated in the case of alexandrite by Zhang *et al*<sup>[59]</sup>. As the result, the fluorescence intensity also plays a important role in the determining of the effective lower temperature limit of the measurement range of a specific thermometer system.

Therefore normalised measurement deviation vs temperature curves calculated based on the temperature sensitivity and fluorescence intensity data for various thermometer systems, could be used to estimate the corresponding measurement range of different systems. These curves are redrawn in Figure 4.29 and normalised to their minimum values respectively. The measurement ranges estimated using these curves are as listed in Table 4.3 together with the measurement resolutions observed at or near the boundaries of these regions. For instance, in the case of the alexandrite based system, if the maximum error is limited to 10 times the minimum value occurring at the corresponding deviation vs temperature curve, the estimated measurement range is from -60 to 680 °C. For the measurement resolution observed at 680 °C is 0.5 °C, a resolution of 0.5 °C or better could be expected to be achievable over the above region.

To explore the use of fluorescence to further, higher temperatures (>750 °C), a laser source with higher output power, or a high-speed and high-sensitive photodetector e.g. a photomultiplier or avalanche detector, has to be used. Thus a special design of the

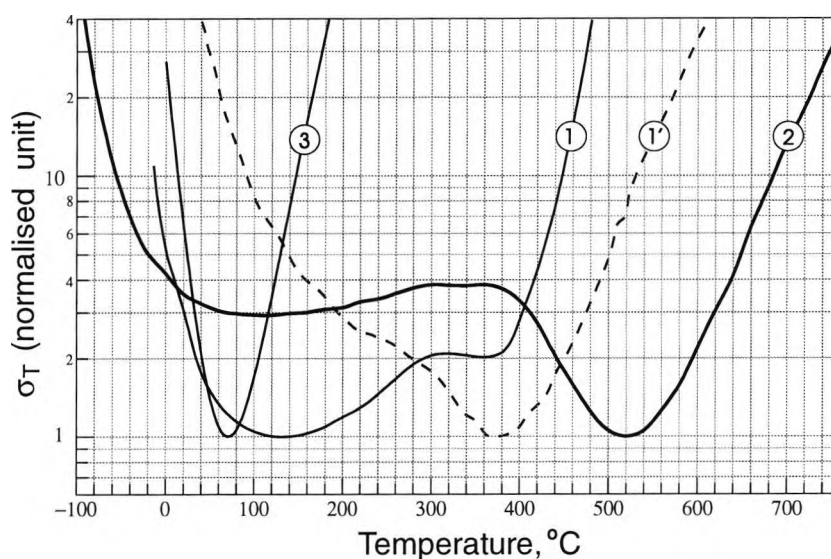


**Figure 4.29:** Error vs.. temperature curves. 1: for the ruby based system using green LED excitation; 1': for the improved ruby based system using He-Ne laser excitation; 2: for the alexandrite based system; 3: for the Cr:LiSAF based system.

**Table 4.3:** Measurement ranges and resolutions of the discussed thermometer systems

	Error limit: 10 × minimum error		Error limit: 20 × minimum error	
	Range	Resolution (response time)	Range	Resolution (response time)
Ruby based system using green LED	-15 to 450 °C	1 °C at 450 °C (2 seconds)	-30 to 470 °C	—
Ruby based system using He-Ne laser	90 to 530 °C	0.3 °C at 90 °C (2 seconds)	50 to 600 °C	1 °C at 600 °C (5 seconds)
Alexandrite based system using 670nm diode laser	-60 to 680 °C	0.5 °C at 680 °C (< 1 second)	-75 to 725 °C	1 °C at 725 °C (1 second)
Cr:LiSAF based system using 670nm diode laser	15 to 150 °C	0.06 °C at 15 °C (< 1 second)	—	—

electronic system for high speed operation has to be introduced. However, these measures could not prove feasible for the development of a practical or commercial fibre optic thermometer system. It is worthwhile to search for new fluorescent materials for higher temperature sensing uses, for example, for engine turbine or furnace measurements. However, taking into account the ultimate effectiveness of radiation thermometry for

temperature sensing beyond 500 °C, it was proposed in this work that a fibre optic sensor scheme with wide temperature sensing range from room temperature or below to >1000 °C could be devised as an effective measure by the cross referencing between the fluorescence lifetime and blackbody radiation. The related work will be discussed in the following chapter.

# Cross Referencing between Blackbody Radiation and Fluorescence Lifetime

---

### 5.0. Abstract

In this Chapter, a high-temperature fibre optic thermometer scheme, based on the cross referencing between a fluorescence lifetime measurement and a blackbody radiation measurement, is discussed. The device demonstrated has relative simplicity of the construction, where the fluorescent material used is Nd:YAG and the lifetime measurement is made by use of the PLD-PMSR scheme. By reference to the use of the fluorescence lifetime measurement, the problems, in pyrometry, of emissivity and sight path factor in the blackbody radiation measurement could be corrected in such a scheme having an internal "self-calibration."

## 5.1. Introduction

It has been shown by the discussions and experimental results presented in Chapter 2 & 4, that the temperature dependence of fluorescence lifetime is an intrinsic feature of the material itself. Hence, with the unique characteristic of being independent of the precise measurement of light intensity, fluorescence lifetime based thermometers are characterised with the feature of being able to be self-calibrated, if necessary, as a result. Such a feature is important in the exploration of the use of fluorescence in high temperature regions. Substantial progress has been made in this aspect. By using magnesium fluorogermanate as the sensing material, a lifetime based thermometer system made by Luxtron [28] is able to cover a measurement range from  $-200^{\circ}\text{C}$  to  $450^{\circ}\text{C}$  and it has been reported later that this sensing material could cover the temperature range up to  $650^{\circ}\text{C}$  [42]. In the work carried out by the author, alexandrite has been successfully demonstrated to be able to cover the entire temperature range from  $-100^{\circ}\text{C}$  to  $740^{\circ}\text{C}$ . However, the extending of the measurement range towards even higher temperature is severely hampered by difficulties of measuring the ever-shortening lifetimes under a worsening signal-to-noise condition experienced at high temperatures, even though the temperature sensitivities of the lifetimes might be still rather high, as shown in Chapter 4.

Some rare-earth activated materials do show strong fluorescence phenomena at temperatures even up to  $1000^{\circ}\text{C}$  with a lifetime long enough to be detected without particular difficulties, as demonstrated in the cases of Nd:YAG and  $\text{ScPO}_4:\text{Eu}^{3+}$  by Grattan *et al* [55] and Bugos *et al* [79] respectively. However, as shown in Figures 5.2 and 5.1, the use of the fluorescence lifetimes of these materials alone can only cover a very limited region of temperature. In both cases, the optimum region for the lifetime information to be used for temperature sensing purposes is from  $\sim 700^{\circ}\text{C}$  and beyond. From room temperature (or lower) to  $\sim 600^{\circ}\text{C}$ , there is some significant increase in the Nd:YAG fluorescence lifetime with temperature increase. This might be of thermometric use, but unless other means can be provided to cover the region from  $\sim 600^{\circ}\text{C}$  to  $\sim 700^{\circ}\text{C}$  (and beyond) and to distinguish the lifetime measurements at temperatures higher or lower than this region, a wide measurement region could not be achieved by using this material.

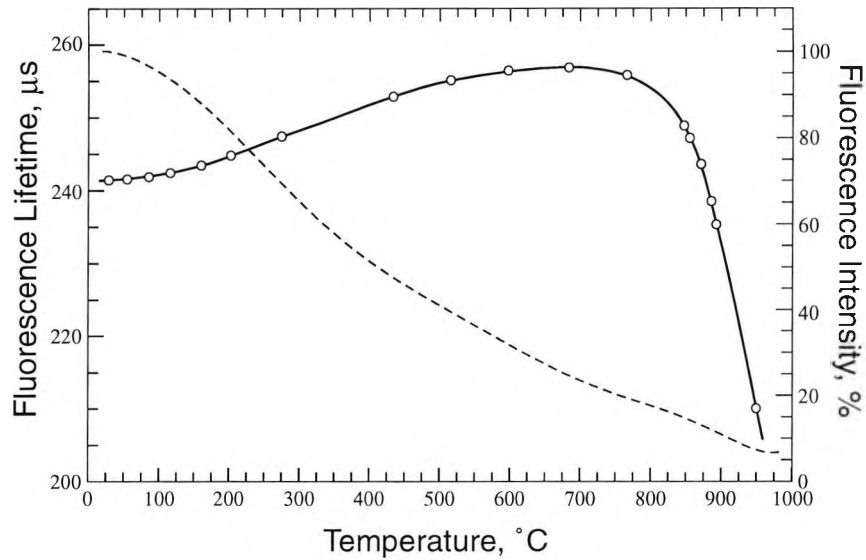


**Figure 5.2:** Temperature dependences of Nd:YAG fluorescence.  $\circ \circ \circ$ : data for the fluorescence lifetime; **solid line**: curve fitting to the fluorescence lifetime data; **dashed line**: curve fitting to the data for fluorescence intensity at 1064nm.

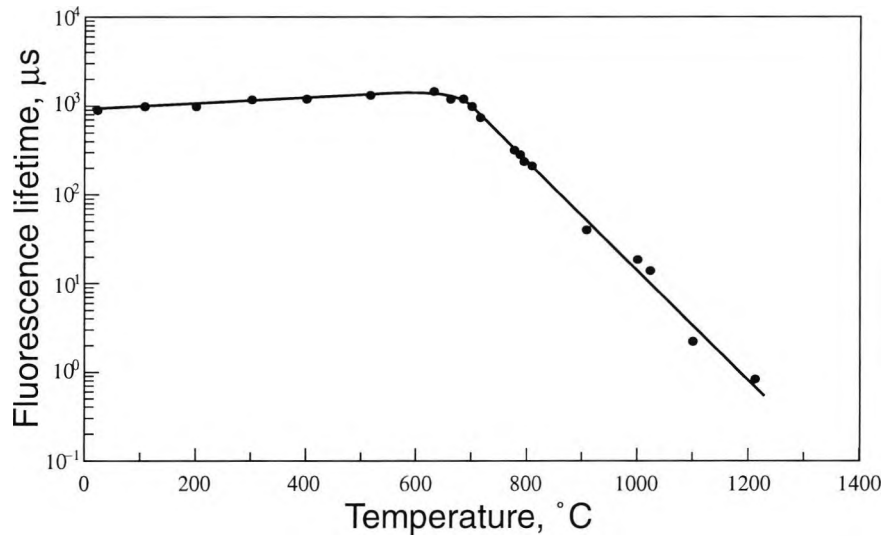


**Figure 5.1:** Fluorescence lifetime calibration curve for  $\text{ScPO}_4:\text{Eu}^{3+}$  from Bugos *et al* [79].

In summary, the use of fluorescence lifetime for temperature sensing at high temperatures is based on the phenomenon of thermal quenching of fluorescence, while this phenomenon is just the very obstacle that blocks the extending of the measurement further into higher temperatures. Therefore, the fluorescence thermometry is intrinsically more effective for measurement within moderate temperature regions, due to this fundamental nature of the fluorescence emission itself.

As a complementary to fluorescence thermometry technique, radiation thermometry is ultimately effective for high temperature ( $>500\text{ }^{\circ}\text{C}$ ) measurement. In fact, the only type of fibre optic system which can cover the range up to  $2000\text{ }^{\circ}\text{C}$  is based on this technique, such as the Accufiber model 100, mentioned in Chapter 1. Though it is claimed that the temperature range can be extended down to  $300\text{ }^{\circ}\text{C}$  [34], the fundamental nature of the measurement process is such that the system works more effectively in the higher temperature region and for many applications  $500\text{ }^{\circ}\text{C}$  is a realistic threshold. Thus, a single fibre optic sensor with extremely wide temperature range might be produced by the combination of above two thermometric techniques, and this is discussed in the work of this Chapter.

## 5.2. Theoretical background

The spectrum of blackbody radiation is described by Planck's radiation law. It is often written in terms of radiant power emitted per unit surface area, that is, in terms of irradiance,  $W_\lambda$ , as a function of wavelength<sup>[80]</sup>:

$$W_\lambda = \frac{C_1}{\lambda^5} \cdot \frac{1}{\exp(C_2/\lambda T) - 1} \quad (5-1)$$

where  $\lambda$  is the wavelength,  $T$  the absolute temperature, in Kelvin, K, and  $C_1$  and  $C_2$  are two radiation constants. The first radiation constant,  $C_1$ , is defined as,

$$C_1 = 2\pi h c^2, \quad (5-2)$$

and the second,  $C_2$ :

$$C_2 = hc/k, \quad (5-3)$$

where  $h$  is Planck's constant,  $c$  the velocity of light, and  $k$  Boltzmann's constant.

However, the above radiation law applies to pure blackbody radiation only. If the body is not a perfect radiator and absorber, as is seen in most practical cases and the case presented here, the amount of the thermally generated radiation is less by a factor  $\epsilon$  ( $\leq 1$ ), the emissivity of the surface. In the scheme to be discussed herein the radiation used for the measurement is observed over a narrow waveband,  $\Delta\lambda$ , centred at  $\lambda_0 = 1064\text{nm}$ , and therefore, the total radiated power detected, at a given temperature,  $T$ , is:

$$W_\lambda = \frac{C_1}{\lambda^5} \cdot \frac{1}{\exp(C_2/\lambda_0 T) - 1} \epsilon \delta S \Delta\lambda \quad (5-4)$$

where  $S$  is the area of the observed radiant surface, and  $\delta$  the sight path factor. The sight path here is mainly formed by an optical fibre, which is immune to the impact of the surrounding atmosphere observed in the open path pyrometer e.g. refractive index changes in the air and other interference effects. Thus the fibre bending and reconnecting would be one of the main reasons for any loss of transmission by the fibre and this gives the variance of  $\delta$ .

To correct the emissivity and sight path factor, a formula to calculate the measured temperature,  $T$ , may be used, which is based on the ratio of the radiation measured,  $W(T)$ , to that,  $W(T_r)$ , at an appropriate temperature  $T_r$  being recorded during a calibration process, as shown by the following

$$T = \frac{T_r}{1 - (\lambda_0 T_r / C_2) \ln[W(T)/W(T_r)]}, \quad (5-5)$$

where  $C_2 = 1.4388 \times 10^{-2} \text{ m K}^{[80]}$ . This equation is deduced from the ratio expression,

$$W(T)/W(T_r) = \frac{\exp(C_2/\lambda_0 T_r) - 1}{\exp(C_2/\lambda_0 T) - 1} \approx \exp\left[\frac{C_2}{\lambda_0} \left(\frac{1}{T_r} - \frac{1}{T}\right)\right], \quad (5-6)$$

where the approximation is made that for  $T < 3000 \text{ K}$ ,  $\exp(C_2/\lambda_0 T) \gg 1$ . Obviously, as long as  $\epsilon$  and  $\delta$  remain constant after calibration,  $W(T)/W(T_r)$  is independent of the emissivity and sight path factor.

If Planck's law is plotted for different temperatures, it can be seen that with increasing temperature, more energy is emitted and the peak emission shifts toward the shorter wavelengths<sup>[3]</sup>. The peak emission wavelength,  $\lambda_{\text{max}}$ , is given by Wien's displacement law, as following:

$$\lambda_{\text{max}} = \frac{2.898 \times 10^{-3}}{T} \text{ m}\cdot\text{K} \quad (5-7)$$

A typical inexpensive silicon photodiode, with its long wavelength spectral response cutting off at  $\sim 1.1 \mu\text{m}$ , is thus well suited to detect the radiation emitted from hot bodies at temperatures from  $450^\circ\text{C}$  to over  $2000^\circ\text{C}$ . The use of other detector materials such as germanium and lead sulphides can extend the measurement to longer wavelengths and thus potentially to lower temperatures, provided some special fibre is used which can efficiently transmit the longer wavelength radiation. However, generally radiation thermometry is more effective and simpler to implement for high temperature measurement. This results because for low temperature measurement, the impact of ambient temperature and sight path problems on the radiation thermometer, will be made worse by the low level of energy

emitted with consequent problems of detection efficiency. Fluorescence based thermometer schemes are more effective for these later applications.

As the measurement of fluorescence lifetime is independent of the precise measurement of light intensity, the fluorescence thermometer is intrinsically free of the impact of the sight path problems. With its effectiveness at low temperature, the fluorescence thermometer is essentially complementary to the radiation thermometer. So, a fibre optic thermometer, in which the fluorescence lifetime and the radiation techniques can be combined together, can be highly effective over a wide temperature range. The emissivity and sight path factors of the radiation can frequently be corrected by cross-referencing the lifetime and the radiation at an appropriate temperature,  $T_r$ .

In this work, with the use of fluorescent materials able to withstand high temperatures, a dual system with a single emitting source has been developed. Tests have been carried out on the use of fluorescent materials incorporated in glasses or crystals. The former tend to suffer irreversible decomposition of the active ingredient at  $> 400^\circ\text{C}$  but crystals can be used up to very high temperatures without adverse effect. This contrasts with the use of phosphor 'paints' which again will suffer decomposition at much lower temperatures, e.g.  $\sim 200^\circ\text{C}$  for that using silicone resins. Thus the scheme discussed involves the use of a single probe, with cross calibration to enable the positive features of the fluorescence scheme to be used at low temperature and those of pyrometry to be utilised at higher temperatures. The signals are highly separable in terms of the fluorescence signal being modulated at a known frequency and the pyrometer radiation being continuous. This makes for ease of detection and cross calibration, as discussed.

### 5.3. Construction of the temperature probe

The probe is made of a 1mm diameter silica fibre with a piece of Nd:YAG crystal cemented on its tip, as shown in Figure 5.3. This piece of Nd:YAG crystal is rectangularly shaped with an approximate size of  $1.5 \times 1.5 \times 1.5 \text{ mm}^3$ . It functions as a sensor element in the lower temperature range when the fluorescence technique is used. The optical characteristics of Nd:YAG as a fluorescent temperature sensor have been discussed in a previous paper by Grattan *et al*<sup>[55]</sup>.

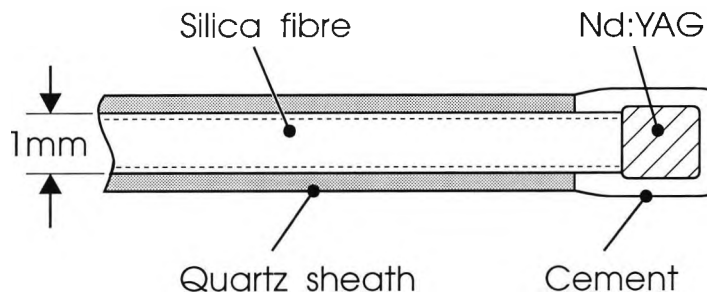


**Figure 5.3:** Schematic of the optical fibre sensor probe.

A rectangular cavity is formed with the cement which bonds the Nd:YAG crystal on the tip of the optical fibre, as depicted in Figure 5.3, for measurement of the thermally generated radiation at high temperatures over a narrow wavelength band centred at 1064 nm. For the Nd:YAG is transparent to the radiation at 1064 nm, the thermally generated radiation to be observed is mainly from the cement surface. The cement is alumina based refractory material. Though the alumina in pure crystallised form is sapphire which is transparent to near infrared radiation, in ceramic form it is opaque over the optical spectrum concerned here. The optically rough surface of the cement is also a poor reflector to this radiation. Therefore, its emissivity is sufficiently high for thermally generated radiation at 1064 nm to be detectable at temperatures down to  $\sim 400 \text{ }^\circ\text{C}$  in this work.

In addition, to strengthen the probe, a quartz tube is used to sheath the silica fibre. As the thermal expansivity of quartz matches that of silica very well, the thermal expansions of the silica fibre and the quartz sheath will not produce a shearing stress on the bonding between the fibre wall and the cement. As a result, the lifetime of the fibre probe would be prolonged.

## 5.4. Configuration of the thermometer

The configuration of the thermometer is presented schematically in Figure 5.4. A Sharp LT010MD0 laser diode, with 5mW peak emission power and the lasing wavelength at 810 nm, is used to excite the Nd:YAG fluorescence. This is a considerable more powerful source than the LED devices available a few years ago and used in previous work<sup>[81]</sup>, increasing the optical signals received. A 1×2 bidirectional fibre coupler is used to transmit the input light to the temperature probe, and to collect the resulting fluorescence response, which has a peak emission wavelength around 1064 nm, as well as the thermally generated radiation from the probe tip to the detection stage. In addition to the fluorescence response and the blackbody radiation, a fraction of the input light is reflected to the detection stage. So, a 1064 nm bandpass interference filter, with a bandwidth 15.2 nm, is placed before the photodetector, a simple inexpensive planar 1 mm silicon PIN photodiode (BPX65), to cut off the reflected input light unwanted at the detection stage.

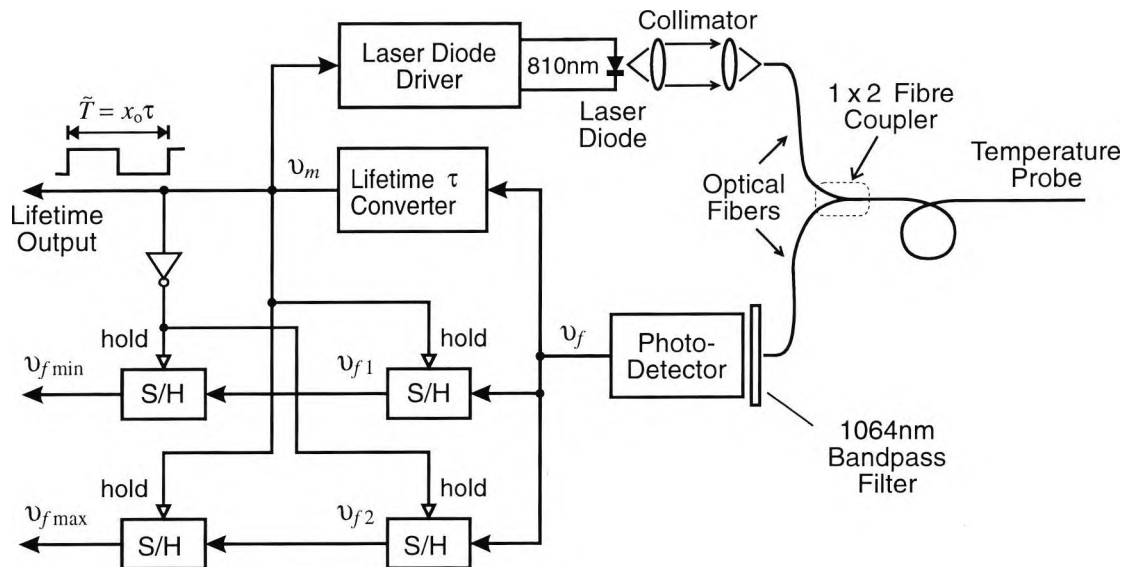


**Figure 5.4:** Schematic of the opto-electronic sensor scheme. (S/H) sample and hold devices.

The "lifetime  $\tau$  converter" is constructed, using the signal processing scheme termed PLD-PMSR in Chapter 3. It generates a square wave signal,  $v_m$ , as shown in Figure 5.5, to modulate the intensity of the input light emitted by the laser diode.  $\tilde{T}$ , the period of this modulation signal, is automatically adjusted by the feedback fluorescence response, to follow the change of the lifetime and keep the relationship  $\tilde{T} = x_0 \tau$  fulfilled. Here the

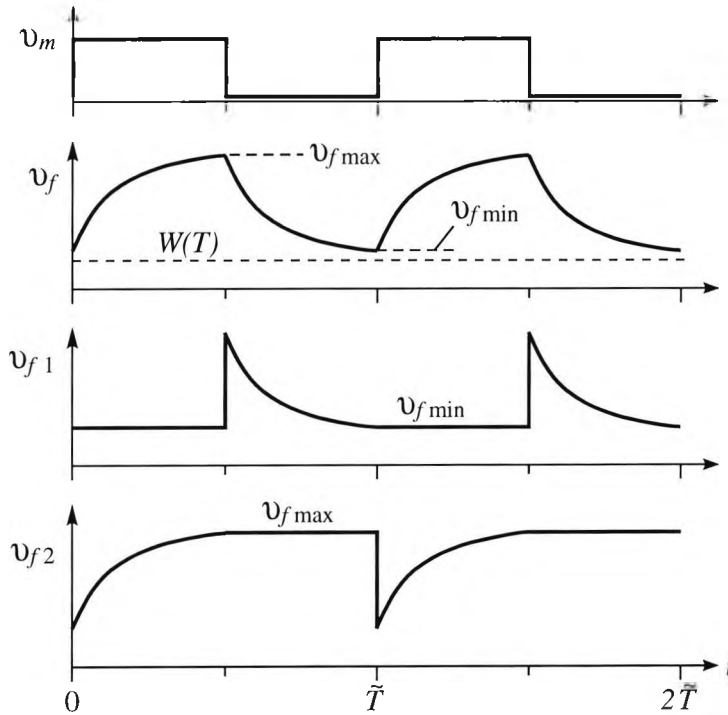


**Figure 5.5** Time dependence of the signals used in the processing scheme. ( $v_m$  vs  $t$ ) input light modulation signal; ( $v_f$  vs  $t$ ) total light signal detected by the photodetector; ( $W(T)$ ) the radiation background signal; ( $v_{f1}$  vs  $t$ ,  $v_{f2}$  vs  $t$ ) outputs of the first stage of S/H devices.

chosen value of the constant  $x_0$  is 6.784 which is the optimum  $x_0$  value for this fluorescence lifetime detection scheme, as was discussed in Chapter 3. The fluorescence response is shown schematically in the waveform representing the photodetector output,  $v_f$  in Figure 5.5, as the periodical, exponentially varying part superimposed on the radiation background signal.

To extract the thermally generated radiation signal,  $W(T)$ , from the photodetector output,  $v_f$ , two pairs of sample/hold (S/H) ICs are employed, operating alternatively as indicated in Figure 5.4. The final output of these S/H ICs are  $v_{f \max}$  and  $v_{f \min}$ , the maximum and the baseline value of the fluorescence emission plus the radiation,  $W(T)$ , respectively, as shown in Figure 5.5. As

$$\begin{aligned} v_{f \min} - W(T) &= [v_{f \max} - W(T)] \exp(-\tilde{T}/2\tau), \\ &= [V_{d \max} - W(T)] \exp(-x_0/2) \end{aligned} \quad (5-8)$$

thereby,  $W(T)$  is given by:

$$W(T) = \nu_{d\min} - (\nu_{d\max} - \nu_{d\min}) \cdot \frac{\exp(-x_0/2)}{1 - \exp(-x_0/2)}$$

$$\approx \nu_{f\min} - 0.0348(\nu_{f\max} - \nu_{f\min}) \quad (5-9)$$

## 5.5. Experimental results

The temperature probe is calibrated against a conventional type K thermocouple over a temperature range from 50°C to 900°C, in a thermostatically controlled oven. The calibration curves of the Nd:YAG fluorescence lifetime and the blackbody radiation at 1064 nm against temperature, are depicted, as the solid and dashed lines respectively, in Figure 5.6. As shown in Figure 5.6, the fluorescence lifetime of Nd:YAG increases with the increase of the temperature to ~ 680°C, and after ~ 700°C, it decreases more and more sharply with the temperature increase, thereby presenting an ambiguity in the output function of the fluorescence lifetime with temperature. The temperature resolution that could be achieved from the measurement of the fluorescence lifetime is  $\pm 3^\circ\text{C}$ , from 100 to 600°C and better than  $\pm 2^\circ\text{C}$ , from 750 to 900°C with, at best,  $\pm 1^\circ\text{C}$  resolution at 850°C. As can be seen, the temperature range from 600 to 750°C is an especially difficult region for the use of lifetime measurement alone. Therefore the radiation technique is best suited to measure the temperature over this region, and upwards as well, because it can achieve a higher measurement resolution at temperatures over 600°C. At a temperature lower than 600°C, the lifetime method is generally preferable.

The signals,  $\nu_{f\min}$  and  $\nu_{f\max}$  output from the system, as shown in Figure 5.4, were recorded from ~ 400 °C to 950 °C. Then based on these data, the magnitudes of the thermally generated radiation from the cavity formed by the cement surrounding the Nd:YAG crystal, shown in Figure 5.3, over a narrow band centred at 1064 nm were calculated using Eq.(5-9), and are logarithmically depicted against temperature, in Figure 5.6, with the normalised unit based on the intensity of the blackbody radiation at 850°C, that is, they are presented in the ratio  $W(T)/W(850^\circ\text{C})$ . These normalised radiation data, obtained by experiment, depicted in Figure 5.6 agrees with the theoretical curve calculated from Eq.(5-6) quite well.

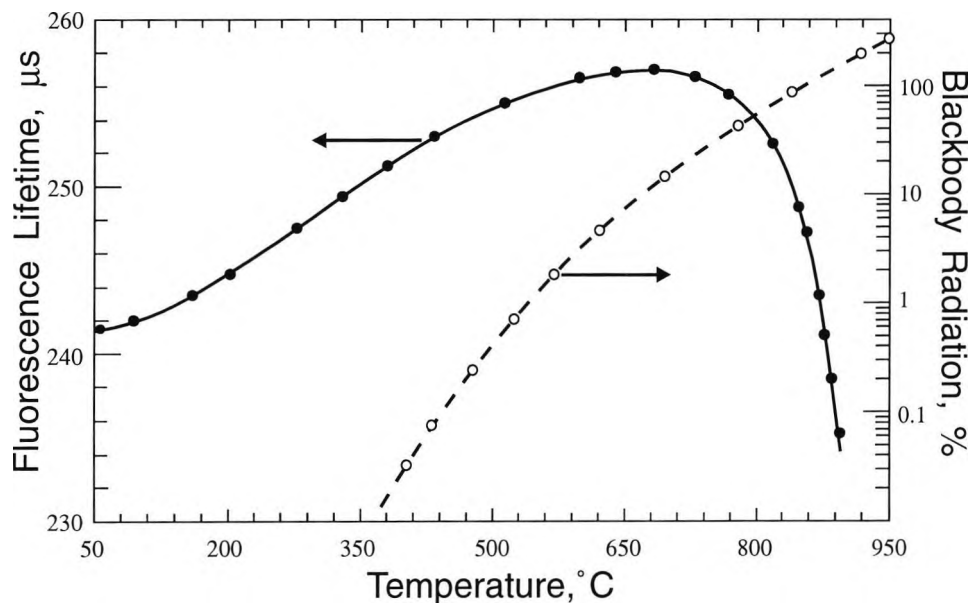


**Figure 5.6:** Calibration graph of the fluorescence lifetime and blackbody radiation vs temperature. ●●●: data for the Nd:YAG fluorescence lifetime; **solid line**: curve fitted to the fluorescence lifetime data. ○○: data for thermally generated radiation normalised to the value at 850 °C; **dashed line**: the corresponding theoretical curve of blackbody radiation.

In fact, Eq.(5-6) is deduced with the assumptions that the emissivity of the cavity surface,  $\epsilon$  is independent of the radiation wavelength and it is also independent of the surface temperature. These assumptions could not always be held in practical cases. However, in this experiment, due to the radiation is observed over a very narrow band of wavelengths, the wavelength dependence of the emissivity is negligible. Further, the other assumption that the emissivity is independent of the temperature, is also acceptable for the radiation cavity constructed in this experiment over the temperature region discussed. This is well illustrated by the agreement between the experimental data and the theoretical curve, as shown in Figure 5.6.

The resolution of the fluorescence lifetime measurement at 850°C is adequate (as discussed) and also the blackbody radiation observed at this temperature is of sufficient intensity, so 850°C is chosen as the reference temperature,  $T_r$ , at which the radiation measurement is referred to the fluorescence lifetime measurement, either to evaluate  $W(T_r)$  to correct the changes of the emissivity and sight path factor or to note when the mismatch between the present and the calibrated values of  $W(T_r)$  exceeds a given limit e.g. corresponding to  $\pm 2^\circ\text{C}$  and recalibration is needed. Also, the fluorescence lifetime value at this

temperature (indicated at  $T > 750^{\circ}\text{C}$ ) is unique and the ambiguity is avoided, thereby confirming this temperature a suitable choice.

It is recognised that, as with all blackbody radiation, some radiation can be obtained from regions other than from the probe tip. Here, the main concern is the radiation generated along the length of the silica fibre used to transmit the radiation from the probe tip, which is exposed at high temperature. This unwanted radiation is mostly generated from the fibre surface, for the fibre material is transparent and thus a poor radiator at the observed waveband over the applied temperature region. Due to the low emissivity of the fibre surface, such radiation is rather weak, compared to that from the wall of the blackbody cavity. Furthermore, only a small amount of such weak radiation can be coupled back into the fibre and transmitted along its transmission direction. As a result, in the work reported, significant impact of this radiation on the blackbody radiation measurement was not observed, under a test in which a portion of the transmission fibre was subjected to temperatures exceeding  $1000^{\circ}\text{C}$ .

## 5.6. Discussion

The feasibility of the thermometry based on the cross referencing between blackbody radiation and fluorescence lifetime is well demonstrated by the prototype scheme presented here. However the temperature sensitivity of the Nd:YAG fluorescence lifetime used is rather low over the region from room temperature to  $\sim 700^{\circ}\text{C}$ . This limits the performance of the thermometer over such a temperature region, for the blackbody radiation level is still quite low at  $600^{\circ}\text{C}$ . The performance of this thermometer scheme could be much improved by using other fluorescent materials which can work more effectively at least up to  $700^{\circ}\text{C}$ , such as alexandrite of which the temperature dependences of the fluorescence is shown in Chapter 2 and 3. The stability of the fluorescence properties when undergoing excursions to a high temperature up to  $1000^{\circ}\text{C}$  also allows alexandrite to be used in such high temperature sensor scheme.

Further, other detector materials, such as germanium, may be used to monitor the blackbody radiation down to the temperature lower than  $500^{\circ}\text{C}$ , so that the overlap of the temperature measurement ranges of the two techniques are wide enough to carry out the necessary cross referencing. By doing so, ruby, the other refractory fluorescent material used before could also be used in this kind of scheme. From the consideration of the stabilities and noise levels of the detector materials used, the use of alexandrite appears to be more favourable.

# Conclusions and Future Work

---

### 6.1. Assessment of fibre optic thermometers

As a result of the fact that temperature can fairly readily be monitored through a variety of transduction mechanisms, there has been a wide range of proposed fibre optic temperature sensor devices. Compared to the remarkable diversity in the ideas proposed for fibre optic sensors, the types of fibre optic thermometers which are commercially available now, are quite a few. Though several reports have been given by major manufacturer [9, 28, 82] reviewing various existing commercial systems, cross comparisons between the performances of these systems are not made or are carefully avoided.

An independent assessment of a few commercial systems, which has been published so far, is that carried out by Harmer [83] in 1986. It was undertaken to address the possible use of fibre optic instrumentation for process control in offshore oil rig installations. The report was concerned with investigating whether devices met the manufacturer's design specifications, and tests were performed to consider such characteristics as accuracy, reproducibility, sensitivity, linearity, effects of supply voltage, handling considerations, and ageing. In addition to a number of other devices, three prototype commercial temperature sensors were tested. Sensor A was a guide fibre bundle with a bimetallic strip and reflector varying the intensity of the backreflected light. Sensor B (manufactured by ASEA) used the temperature-dependent fluorescence intensity of a semiconductor crystal, and sensor C (manufactured by Luxtron) depended on the fluorescence lifetime of a phosphor. The comments may be summarised in that with sensor A, problems associated with intensity modulation were seen, due to connector and cable losses which could be

**Table 6.1:** Assessment of early commercialised fibre optic thermometer systems, by Harmer<sup>[83]</sup>.

	Sensor B	Sensor C
Principle	Fluorescence intensity	Fluorescence lifetime
Fibre type	100 $\mu\text{m}$	305/362 $\mu\text{m}$
Range	200 $^{\circ}\text{C}$	-35 $^{\circ}\text{C}$ to 250 $^{\circ}\text{C}$
Accuracy	$\pm 0.4$ $^{\circ}\text{C}$	3.5 $^{\circ}\text{C}$ (Manufacturer's specification: $\pm 0.2$ $^{\circ}\text{C}$ )
Effect of reconnection	0.7 $^{\circ}\text{C}$ (max)	1.5 $^{\circ}\text{C}$
Microbending effect error (5dB loss)	0.9 $^{\circ}\text{C}$	2.1 $^{\circ}\text{C}$

misconstrued to be a temperature error, but sensor B could achieve accuracy of better than  $\pm 0.4^{\circ}\text{C}$  with individual calibration of the probe. Consistent reading were seen over a period of testing of 2 weeks. For the fluorescence lifetime-type device, errors greater than the specifications were seen. The assessment results for sensors B and C are listed in Table 6.1.

In the test reported, the fluorescence-intensity based sensor did appear to perform very well when individually calibrated. On the contrary, the performance of the lifetime based sensor was significantly poorer than expected. The magnitudes of errors induced by the effects of reconnection and microbending in the sensor C, as listed in Table 6.1, were much higher than those in sensor B. It is rather surprising for the former would be expected to perform intrinsically better than the latter in these aspects. Though sensor C was at an early stage of production at that time, the test did show how much difference a device could perform, in practice, from the specification given by the manufacturer. Therefore, it is important that commercial devices be subjected to such intensive scrutiny both in the user's interest and for manufacturers to see the device defects which they do not expect or chose to neglect.

Of course, if the work were not accompanied with an understanding of the working principles of these devices, the status of their development, and their potential, the results of this test would be quite misleading when a decision was to be made to choose right type of sensor for further development. It was shown by later development, as mentioned in Chapter 1, that the lifetime-based scheme is much favoured in terms of performance and cost. That was the reason for the major manufacturer, Luxtron, to substitute the lifetime-based thermometer for the early, intensity-based device in production<sup>[9]</sup>.

## 6.2. Cross comparison to previous experimental devices

It is nearly a decade since the work on a fluorescence decay-based fibre optic sensor scheme at City University was first reported by Grattan and Palmer<sup>[21]</sup>. Since then, a number of experimental devices have been developed at the laboratory. These devices and the experimental results gathered in the due course of the development provide a sound basis to assess the experimental devices produced in this thesis work.

The assessment of various major experimental devices developed previously in the laboratory and those made in this work is presented in Table 6.2, where the work is listed in chronological order. The progress made in sensor development is obvious. The response times of the current devices are correspondingly shorter than those of the previous sensors which used the same sensing materials, due to the efficiencies of the new signal processing schemes. The measurement ranges of fluorescence lifetime based thermometers have been greatly extended into higher temperatures, showing the superiority of the use of PLD techniques for the detection of fluorescence lifetimes over a wide consecutive range. The improvement or absence of deterioration in the measurement accuracy compared to that in the corresponding previous device gives evidence that the PLD schemes have the high noise-suppression capability as like the phase and modulation scheme. For instance, by using the phase and modulation technique, the best measurement deviation achieved was 0.04 °C in the previous LED excited ruby fluorescence device<sup>[29, 85]</sup> with a response time of 10 seconds; in the similar device of this work but using the PLD-PMSR technique, the best deviation achievable is 0.1 °C with a short response time of only 2 seconds. By increasing the response time of the latter device to 10 seconds, its resulting measurement

**Table 6.2:** The assessment of various experimental devices developed at the laboratory.

Year	Sensing Material	Range	$\sigma_n^a$	Response time	Signal Processing technique
1985 [Ref. 84]	Nd: glass (excited by LED)	15 to 130 °C	1 °C	6 s	Pulse Measurement
1987 [Ref. 81]	Nd: glass (excited by LED)	-50 to 200 °C	0.7 °C	3 s	Pulse Measurement
1987 [Ref. 66]	alexandrite (excited by He-Ne laser)	20 to 150 °C	0.3 °C	3 s	Phase and Modulation
1987 [Ref. 85, 29]	ruby (excited by LED)	20 to 160 °C	0.3 °C	10 s	Pulse Measurement
		20 to 160 °C	0.04 °C (at 160 °C)	10 s	Phase and Modulation
1988 [Ref. 45]	alexandrite (excited by LED)	20 to 150 °C	0.3 °C	1 s	Phase and Modulation
This work	ruby (excited by LED)	20 to 450 °C	1 °C	2 s	PLD-PMSR <sup>c</sup> technique
		120 to 140 °C	0.1 °C		
	ruby (excited by He-Ne laser)	90 to 530 °C	0.3 °C	2 s	PLD-PMSR <sup>c</sup> technique
		~370 °C	0.03 °C		
	alexandrite (excited by VLD <sup>b</sup> )	20 to 725 °C	1 °C	< 1 s	PLD-PMTR <sup>d</sup> technique
		20 to 160 °C	< 0.2 °C		
	alexandrite (excited by He-Ne laser)	potentially -100 to 700 °C	1 °C	< 1 s	PLD-PMTR <sup>d</sup> technique
	Cr: LiSAF (excited by VLD <sup>b</sup> )	15 to 150 °C	0.06 °C	< 1 s	PLD-PMTR <sup>d</sup> technique
30 to 100 °C		0.02 °C			

a:  $\sigma_n$  - measurement deviation. b: VLD - visible laser diode. c: PLD-PMSR - as defined in Chapter 3.

d: PLD-PMTR - as defined in Chapter 3.

deviation could be estimated, using the  $\sigma_n/\sqrt{m}$  law to be  $0.1^\circ\text{C}/\sqrt{5}$  and it is of the same order as that of the former device reported by Selli<sup>[85]</sup> and Grattan *et al*<sup>[29]</sup>.

The experimental data of the fluorescence lifetimes of various materials, obtained in the course of study have also been compared to those obtained previously in the laboratory or from other groups of workers. Though there are some slight differences, those obtained from similar materials generally share the same temperature profiles. The slight discrepancy among these data may originate from differences in concentrations of the impurities in the sensing materials, their geometrical shapes and sizes which would exhibit different levels of fluorescence trapping effects and so on.

### 6.3. Conclusions

In this work, the aims set out at the beginning of the study have been fulfilled by:

- (1) The investigation of the established work on the fluorescence thermometry, presented in Chapter 1. It starts from an overview of the development of fibre optic temperature measurement, and examines various exciting sensor schemes, showing the advantageous characteristics of fluorescence thermometry. Then, illustrated by the development of the fluorescence thermometry, it shows that in addition to the search for suitable sensing materials, the development of an effective, thermometry-oriented signal processing electronic scheme for the detection of fluorescence lifetime plays an important role in the development of fluorescence thermometry. Virtually, almost every major progress made in such development could be marked with the introduction of a new signal processing idea. This is not to say that the importance of the development of signal processing schemes could override that of the search for new sensing materials. It is just a matter of fact that the former represents basic underlying work, from which the development of fluorescence thermometry can proceed.
- (2) The exploration of the theoretical basis of the fluorescence in suitable materials, described in Chapter 2. The work is concentrated on the temperature dependence of the lifetime of fluorescence in  $\text{Cr}^{3+}$  doped materials, the great potential of which as temperature sensing elements has been demonstrated in various re-

ported sensor schemes. Two single configurational coordinate models have been proposed, which could closely explain the mechanism of the temperature dependence of the fluorescence lifetimes in materials with high and low crystal field strengths respectively. This shows that such a temperature dependence is intrinsic to the properties of a fluorescent material. Hence, it is reproducible from material to material, and can be of thermometric use. This lays the basis of the entire science of fluorescence thermometry. In addition, the discussion also shows that due to difference between the mechanisms in the temperature dependences of fluorescence in low and high field strength materials, the lifetime of the fluorescence in the former is highly sensitive to temperature variance over a very limited region, while that in the latter could exhibit a moderate sensitivity to temperatures over a wide region. These features have been exploited in this work in different sensor systems.

- (3) The development of a whole category of effective electronic signal processing schemes, the "phase-locked detection of fluorescence lifetimes," is described in Chapter 3. Such a basic scheme shows the advantages of the phase and modulation technique for the high precision measurement of fluorescence lifetimes. However, unlike the phase and modulation technique, the PLD technique is capable of covering a wide consecutive measurement range, for the modulation frequency is automatically adapted to the measured lifetime. Furthermore, the PLD-PMTR scheme devised in this work has overcome the vital shortcoming of the previous PLD and other phase modulation schemes, that is its vulnerability to the excitation light leakage. Consequently it can greatly enhance the performance and cut the cost of a related fluorescence thermometer.
- (4) The development of experimental thermometer systems for a range of temperatures was carried out and is presented in Chapter 4. Two  $\text{Cr}^{3+}$  activated refractory materials with high strength crystal fields, ruby and alexandrite, are used for wide range and high temperature measurement. Ruby and alexandrite are capable for measurement over the regions from  $-15$  to  $530$  °C and from  $-100$  to  $725$  °C respectively. The lower temperature measurement limits are set by the insensitiveness of the lifetimes to temperature variance or the ambiguity of such

temperature dependence at low temperatures. The higher the crystal field strength of the material is, the higher temperature the lower measurement limit shifts towards.

The highest temperature that a fluorescent material is capable of measuring is limited by the nonradiative transitions occurring over high temperature region, no matter whether the material is of high or low crystal field strength. Such a temperature measurement limit is subject to two parameters,  $\Delta E_q$  and  $\beta$  which are defined by a single configurational coordinate model described in Chapter 2, and are intrinsic to the specific material.

The use of Cr:LiSAF for temperature measurement over the biomedical range has demonstrated that the low field strength material is particularly useful for high resolution measurement over a limited temperature region. The 0.02 °C measurement resolution achieved with 1 second response time, listed in Table 6.2, is the best which has been achieved from a fluorescent sensing material, over the biomedical region in the laboratory.

The close fit of the two single configurational coordinate models to the lifetime data of corresponding materials has shown the great potentials for them to be used as calibration formulae for a category of Cr<sup>3+</sup> fluorescence based thermometers. It is expected that by using these models, such a thermometer could only need to be calibrated at an appropriate single temperature point to correct the systematic error introduced by the time-constant of the entire electronic appliance.

In addition to the accomplishment of the preset objectives, an attempt has been made to extend the consecutive measurement range of fibre optic temperature sensor further to cover the temperature region from room temperature (or possibly lower) to 1000 °C and beyond, as discussed in Chapter 5. The experiment described in that Chapter convincingly illustrates the feasibility of a scheme based on the cross referencing between blackbody radiation and fluorescence lifetime to achieve this target. The development of such a scheme is a subject of future study. Further to the schemes being demonstrated in the

laboratory, the work has been published, during the last few years, in the International literature.

## 6.4. Discussion and future work

### 6.4.1. Cryogenic temperature measurement

This thesis study has been concentrated on the temperature measurement from room temperature to temperatures as high as the fluorescence thermometry could reasonably cover. Rather little effort has been expensed on the investigation of the use of fluorescence thermometry in the sub-room temperature region. In fact, the active research work in the area of superconductors and the optimistic expectation of the applications of such research indicate a promising potential market for dedicated fibre optic thermometers, and fluorescence thermometry does appear to have the potential for significant use in cryogenic region.

As mentioned in Chapter 4, the data from Walling *et al*<sup>[51]</sup> shows the alexandrite fluorescence lifetime is capable to be used for temperature measurement down to -100 °C (~ 170 K). To extend the measurable temperature to further lower ranges, sensing materials with crystal field strengths lower than that of alexandrite, such as emerald formula and Cr<sup>3+</sup> doped GSGG could be useful. According to the data from Fonger and Struck<sup>[52]</sup>, as shown in Figure 6.1, the emerald fluorescence lifetime has the potential for thermometric use

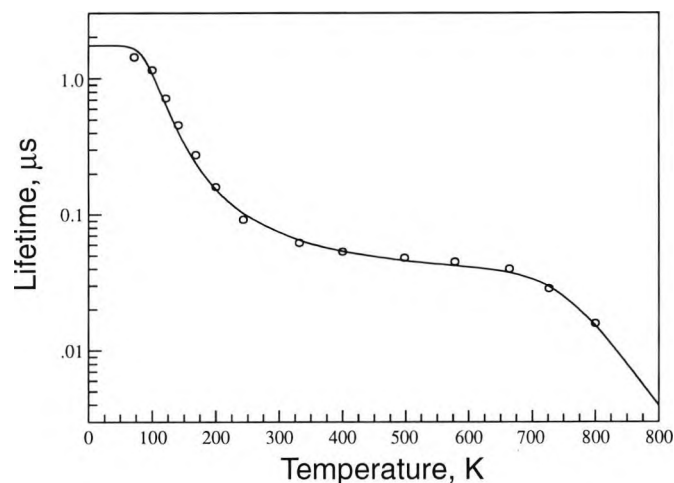


**Figure 6.1:** Temperature dependence of emerald fluorescence lifetime from Fonger and Struck<sup>[52]</sup>.

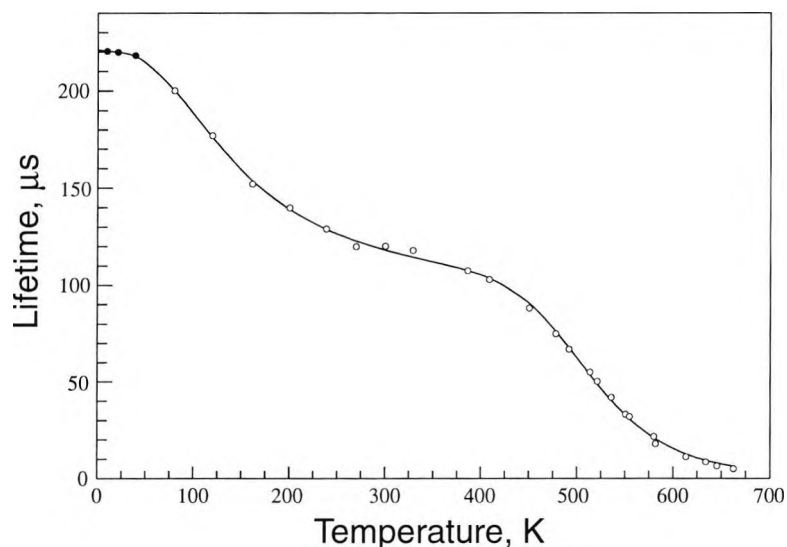


**Figure 6.2:** Temperature dependence of GSGG:Cr<sup>3+</sup> fluorescence lifetime. o o o: data from Armagan and Bartolo [86]. • • •: data from Healy et al [87].

down to 100 K (~ -173 °C). With reference to the data obtained by Armagan and Bartolo [86] and those from Healy et al [87], the GSGG:Cr<sup>3+</sup> fluorescence lifetime, shown in Figure 6.2, could be used down to 50 K or even lower. The test of the uses of these materials in the cryogenic region is worthwhile in future work. In addition, the uses of low crystal field strength materials, such Cr:LiBAF mentioned in Chapter 2, as well as other non-Cr<sup>3+</sup> activated materials, are also worth examination.

#### 6.4.2. Limitation of the signal processing schemes

There are two shortcomings in the PLD schemes. First, it is not a economic way to use the PLD technique for multi-point temperature measurement. As the modulation cycle of the excitation light is related to the temperature of the measurement point, the use of the PLD technique requires a separate light source for each measurement point, and also a dedicated electronic circuit is needed for each point of measurement. Therefore, the cost of using the PLD scheme for multi-point measurement is expected to be higher than that using the pulse measurement technique. The latter allows the sharing of a single excitation light source among a number of measurement points without particular difficulty, and it is possible to address each measurement point, through multiplexing, by the same electronic signal processing circuit.

The second shortage is that the modulation frequency of the excitation light should be able to vary continuously over a specific region and to be controlled by an electrical signal. This has excluded the use of the PLD technique with flash lamps and some pulsed laser sources.

As far as the  $\text{Cr}^{3+}$  doped materials are used, the second shortage has no much significance, for a laser diode emitting at 635 nm is rather satisfying as the excitation source. This sort of visible laser diode is already commercially available at a price less than half of that of its counterpart, He-Ne laser, and a steady decrease in its price has been seen in past two years. However, as for the applications of PLD schemes in multipoint measurement, a satisfactory solution to meet the first shortage has not yet been conceived. By considering the attractive characteristics, it is perhaps worthy of looking for such a solution. It might be needed to introduce some fundamental changes in the PLD schemes or a brand new idea for multipoint temperature measurement applications.

### 6.4.3. Investigation of other sensing materials

Search for even better sensing materials is always a subject of future work. In the family of  $\text{Cr}^{3+}$  doped materials, those which have the potentials for thermometric uses and have not been thoroughly examined or not at all for these uses are still in quite long list. Further, so far, only have  $\text{Cr}^{3+}$  doped crystalline materials been tested and the  $\text{Cr}^{3+}$  doped glassy solids were ignored. This is due to the low quantum yield of transition metal ions in amorphous solids. As quoted by Andrews *et al* [88], the luminescence quantum yield of  $\text{Cr}^{3+}$  ion at ambient temperature is about 0.1 in many common glass whereas in crystalline hosts its yield is frequently close to unity. Nevertheless, with the availability of cheap, compact and high power suitable light sources, e.g. visible laser diodes, the thermometric use of these materials is possibly feasible, for at least these materials are cheap and easy to fabricate and the bonding of glassy materials onto the tips of fibre probes is relatively simple due to their low deformation temperatures.

It is interesting to notice the recent results from the research work on  $\text{Cr}^{3+}$  doped glasses by Rasheed *et al* [89] and Henderson *et al* [90]. Rasheed *et al* [89] have discussed the optical properties of a number of  $\text{Cr}^{3+}$  doped silicate glasses with compositions chosen to

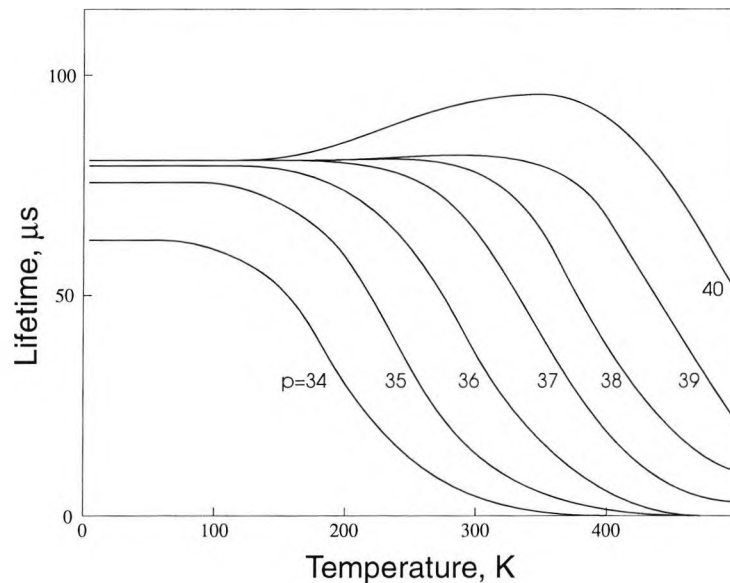


**Figure 6.3:** Temperature dependence of the  $\text{Cr}^{3+}$  fluorescence lifetime calculated assuming different values of  $p$  by Henderson *et al* [90].

vary the average value of strength of the octahedral crystal field at the  $\text{Cr}^{3+}$  ion site. Henderson *et al* [90] have shown the calculated results for temperature dependences of the  $\text{Cr}^{3+}$  luminescence lifetimes in glasses with different values of crystal field strength, as depicted in Figure 6.3 where  $p$  is a function of crystal field strength. These results indicate that it is possible to produce a glassy fluorescent material with desired temperature dependence of fluorescence lifetime to cater for different thermometric applications by choosing appropriate compositions for the glass.

## 6.5. Further potential of this work

Apart from the thermometric applications discussed here, the entire category of PLD techniques devised here are equally applicable to other lifetime or time-constant based sensor schemes. For instance, recently Draxler and Lippitsch [91] have illustrated the potentials of the fluorescence lifetime based measurement in chemical sensing area. An example is the dependence of the fluorescence lifetime on oxygen pressure in the complex tris(2,2'-dipyridyl)ruthenium (II) dichloride hydrate. This could result in a oxygen sensor with the resolution and accuracy being easily brought to a few torr of oxygen as demonstrated by the work of Lippitsch *et al* [92]. Another example is the pH sensing using the

fluorescence lifetime of norharman in the range pH 5 to 12<sup>[91]</sup>. The possibility of using lifetime-based measurement in the sensing of metal ions has also been considered<sup>[91]</sup>.

A further potential application of this work is in the high pressure (1 MPa to 100 GPa) measurement. The calibration of the shift of the ruby fluorescence line  $R_1$  as a function of pressure has already provided an important internal pressure sensor for high-pressure experiments. Indeed, this shift is recognised as a suitable secondary pressure standard<sup>[93]</sup> up to 100 GPa. It has been shown by Eggert *et al*<sup>[94]</sup> that in a nonhydrostatic environment the fluorescence lifetime of the  $R$  line also exhibits a significant pressure dependence. Similar pressure induced  $R$  line shift in alexandrite has also been observed by various groups of workers<sup>[95-97]</sup>. It is suggested by Jahren *et al*<sup>[97]</sup> that the alexandrite fluorescence could provide an alternative to the ruby-fluorescence scale. The pressure dependence of the lifetime of alexandrite  $R$ -line fluorescence has also been observed<sup>[96]</sup>, as shown in Figure 6.4. These are strongly implication of the potential of the lifetime-based measurement in the high pressure measurement applications.

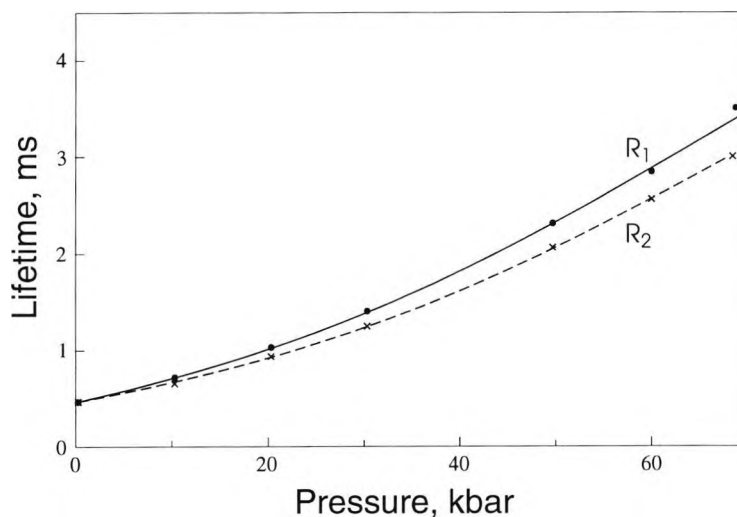


**Figure 6.4:** Pressure dependence of the lifetime of alexandrite R-line fluorescence in hydrostatic environment from Jia *et al*<sup>[96]</sup>.

## References

---

- 1 Johnston, J. S. (1987). Editorial of special issues on temperature. Measurement and Control 20: 5.
- 2 Grattan, K. T. V. (1991). Fibre optic techniques for temperature sensing. In: Fibre Optic Chemical Sensors and Biosensors, Vol. II, Ed. by O. S. Wolfbeis. (London: CRC Press): 151 - 192.
- 3 Dixon, J. (1987). Industrial radiation thermometry. Measurement and Control 20 (7): 11 - 16.
- 4 Midwinter, J. (1985). Current status of optical communications technology. Journal of Lightwave Technology LT3: 927.
- 5 Institute of Measurement and Control, UK. (1982). Symposium on Optical Sensors and Optical Techniques in Instrumentation, London, November, 1981, collected papers. Pub: Institute of Measurement and Control, London, 1982.
- 6 Harmer, A. L. (1988). Fibre optic sensors for sale? In: Proceedings of Optical Fibre Sensors Conference OFS '88, New Orleans, January 1988. Pub: OSA.
- 7 Tortishell, G. (1987, 1988). Reports to UK Optical Sensors Collaborative Association, Unpublished, 1987, 1988.
- 8 Grattan, K. T. V. (1987). The use of fibre optic techniques for temperature measurement. Measurement and Control 20 (7): 32 - 39.
- 9 Wickersheim, K. A. (1992). Fiberoptic thermometry: an overview. In: Temperature - Its Measurement and Control in Science and Industry, Vol.6, Part 2 (New York: American Institute of Physics), pp.711 - 714.
- 10 Jones, B. E. and Spooner, R. C. (1984). An optical fibre pressure sensor using a holographic shutter modulator with two wavelength intensity referencing. SPIE Proceeding 514: 223.
- 11 Meggitt, B. T., Palmer, A. W. and Grattan, K. T. V. (1988). Fibre optic sensors using coherence properties - signal processing aspects. International Journal of Optoelectronics 3 (6): 451 -464.

- 12 Bosselmann, Th. and Ulrich, T. (1984). High accuracy position sensing with fibre coupled white light interferometers. In: Proceeding of 2nd Conference on Optical Fibre Sensors (OFS '84). SPIE Proceedings 514: 361.
- 13 Rozzel, T., Johnson, C. C., Durney, C. H., Lords, J. L. and Olson, R. G. (1974). A nonperturbing temperature sensor for measurements in electromagnetic fields. Journal of Microwave Power 9 (3):241.
- 14 Brenci, M. (1984). Thermochromic transducer optical fibre temperature sensor. SPIE Proceedings 515: 155, 1985.
- 15 Dakin, J. P., Pratt, D. J., Bibby, G. W. and Ross, J. N. (1985). Distributed anti-Stokes ratio thermometry. 3rd International Conference on Optical Fiber Sensors, Postdeadline Session, San Diego, USA, February 1985.
- 16 Dakin, J. P., Pratt, D. J., Bibby, G. W. and Ross, J. N. (1985). Distributed optical fibre Raman temperature sensor using a semiconductor light source and detector. *Electron. Lett.* 21: 569.
- 17 Knox, J. M., Marshall, P. M. and Murray, R. T. (1983). Birefringent filter temperature sensor, Proc. 1st Conf. Opt. Fibre Sens. (OFS 83) 1983, Pub: IEE, London, p.1.
- 18 Sholes, R. R. and Small, J. G. (1980). Fluorescent decay thermometer with biological applications. Review of Scientific Instruments 51 (7): 882-884.
- 19 Wickersheim, K. A. and Alves, R. V. (1982). Fluoroptic thermometry: a new RF-immune technology. *Biomedical Thermology*. Pub: Alan Liss, New York, pp.547-554.]
- 20 Bosselmann, Th., Reule, A. and Schröder, J. (1984). Fibre-optic temperature sensor using fluorescence decay time. In: Proceeding of 2nd Conference on Optical Fibre Sensors (OFS '84). SPIE Proceedings 514: 151 - 154.
- 21 Grattan, K. T. V. and Palmer, A. W. (1984). A fibre optic temperature sensor using fluorescence decay. SPIE proceedings 492: 535-542.
- 22 Saaski, E. (1986). A family of fibre optic sensors using cavity resonator microshifts. In: Proceeding of 4th International Conference on Optical Fibre Sensors, 1986, Tokyo.
- 23 Saaski, E. and Hartl, J. (1987). U.S. Patent 4,678,904 (7 July 1987).

- 24 Beheim, G. (1986). Fibre-optic thermometer using semiconductor etalon sensor. *Electron lett.*, Vol. 22 (5), pp. 238-239.
- 25 Christensen, D. A. (1977). A new non-perturbing temperature probe using semiconductor band edge shift. *Journal of Bioengineering*, vol.1, pp.541-545.
- 26 Kyuma, K., Tai, S., Sawada, T. and Nunonshita, M. (1982). *IEEE Journal of Quantum Electronics* QE18, 676.
- 27 Dakin, J. P. and Kahn, D. A. (1977). A novel fibre optic temperature probe, *Opt. Quant. Electron.*, 9, 540.
- 28 Wickersheim, K. A. and Sun, M. H. (1987). Fiberoptic thermometry and its applications. *Journal of Microwave Power* 22 (2): 85 - 94.
- 29 Grattan, K. T. V., Selli, R. K. and Palmer, A. W. (1988). Ruby decay-time fluorescence thermometer in a fiber-optic configuration. *Review of Scientific Instrument* 59 (8): 1328 - 1335.
- 30 Zhang, Z. Y., Grattan, K. T. V., Palmer, A. W., Summers, R., Hughes, S. and Summan, R. (1993). Cr: LiSAF fluorescence lifetime based fibre optic thermometer and its applications in clinical RF heat treatment. *In: International Conference of Biomedical Optics '93, Los Angeles, California, USA, January 1993. SPIE Proceedings 1885: 300 - 305.*
- 31 Zhang, Z. Y., Grattan, K. T. V. and Palmer, A. W. (1993). Phase-locked detection of fluorescence lifetime and its thermometric applications. *In: International Conference of Biomedical Optics '93, Los Angeles, California, USA, January 1993. SPIE Proceedings 1885: 228 - 239.*
- 32 Windhorn, T. H. and Cain, C. H. (1979). Optically active binary liquid crystal thermometry. *IEEE Transactions on Biomedical Engineering* 26 (3): 148.
- 33 Saaski, E. and Hartl, J. (1992). Thin-film Fabry Perot temperature sensors. *In: Temperature - Its Measurement and Control in Science and Industry, Vol.6, Part 2 (New York: American Institute of Physics), pp.731 - 734.*
- 34 Accufiber, Inc. (1988). Model 100 Multi-channel optical fiber thermometer system. Publicity data, Accufiber, Inc., Beaverton, Oregon, U.S.A.

- 35 Schulman, J. H. and Klick, C. C. (1987). Fluorescence. In: McGraw-Hill Encyclopedia of Science & Technology. (New York, St. Louis, San Francisco: McGraw-Hill). ]
- 36 Butler, K. H. (1980). Fluorescent lamp phosphors, (Pennsylvania: Pennsylvania State University Press) Chapter 4, p.54.
- 37 Payne, S. A., Chase, L. L., Smith, L. K., Kway, W. L. and Newkirk, H. W. (1989). Laser performance of  $\text{LiSrAlF}_6:\text{Cr}^{3+}$ . Journal of Applied Physics 66 (3): 1051 - 1056.
- 38 Zhang, Z. Y., Grattan, K. T. V. and Palmer, A. W. (1992a). Sensitive fibre optic thermometer using Cr:LiSAF fluorescence for bio-medical sensing applications. In: Proceedings of 8th Optical Fiber Sensors Conference, Monterey, California, Jan. 1992, pp.93 - 96.
- 39 Imbusch, G. F. (1978). Inorganic luminescence. In: Luminescence spectroscopy, ed. by M. D. Lumb, Chapter 1, p.72. (London, New York, San Francisco: Academic Press).
- 40 Ovren, C., Adolleson, M. and Hök, B. (1983). Fibre optic systems for temperature and vibration measurements in industrial applications. In: Proc. Int. Conf. Optical Techniques in Process Control, The Hague, 1983. (Pub: BHRA - British Hydromechanical Research Association, Cranfield, Bedford, UK).
- 41 James, K. A., Quick, W. H. and Strahan, V. H. (1979). Fiber optics: the way to true digital sensors?. Control Engineering 26 (2): 30 - 33.
- 42 Sun, M. (1992). Fiberoptic thermometry based on photoluminescent decay times. In: Temperature - Its Measurement and Control in Science and Industry, Vol.6, Part 2 (New York: American Institute of Physics), pp.715 - 719.
- 43 Wickersheim, K. A. (1991). Application of fibre optic thermometry to the monitoring of winding temperatures in medium and large power transformers. SPIE Proceedings 1584: 3 - 14.]
- 44 Dowell, L. J. and Gillies, G. T. (1990). Errors caused by baseline offset and noise in the estimation of exponential lifetimes. Review of Scientific Instruments 62 (1): 242-243.

- 45 Augousti, A. T., Grattan, K. T. V. and Palmer, A. W. (1988). Visible-LED pumped fiber-optic temperature sensor. IEEE Transactions on Instrumentation and Measurement 37 (3): 470 - 472.
- 46 Bosselmann, Th. (1983). UK Patent Application GB 2,113,837A.
- 47 Zhang, Z. Y., Grattan, K. T. V. and Palmer, A. W. (1991). A novel signal processing scheme for a fluorescence based fibre-optic temperature sensor. Review of Scientific Instruments 62 (7): 1735 - 1742.
- 48 Fernicola, V. and Crovini, L. (1992). Two fluorescent decay-time thermometers. In: 7th International Symposium on Temperature, Toronto, Canada, April 30, 1992.
- 49 Zhang, Z. Y., Grattan, K. T. V. and Palmer, A. W. (1992b). Fibre-optic high temperature sensor based on the fluorescence lifetime of alexandrite. Review of Scientific Instruments 63 (5): 3177 - 3181.
- 50 Sugano, S., Tanabe, Y. and Kamimura, H. (1970). Multiplets of transition-metal ions in crystals. (New York and London: Academic Press): 107-112.
- 51 Walling, J. C., Peterson, O. G., Jenssen, H. P., Morris, R. C. and O'Dell, E. W. (1980). Tunable alexandrite lasers. IEEE Journal of Quantum Electronics QE-16 (12): 1302-1315.
- 52 Fonger, W. H. and Struck, C. W. (1975). Temperature dependences of Cr<sup>+3</sup> radiative and nonradiative transitions in ruby and emerald. Physical Review B 11 9: 3251-3260.
- 53 Payne, S. A., Chase, L. L. and Wilke, G. D. (1989b). Optical spectroscopy of the new laser materials, LiSrAlF<sub>6</sub>:Cr<sup>3+</sup> and LiCaAlF<sub>6</sub>:Cr<sup>3+</sup>. Journal of Luminescence 44 (3):167-176.
- 54 Stalder, M., Chai, B. H. T. and Bass, M. (1991). Crystal growth and spectroscopy of Cr:LiBaAlF<sub>6</sub>. Paper presented at the Advanced Solid State Lasers Topical Meeting, Hilton Head Island, SC, March 1991.
- 55 Grattan, K. T. V., Manwell, J. D., Sim, S. M. L. and Willson, C. A. (1987). Lifetime investigation of fluorescence from neodymium-yttrium-aluminum garnet at elevated-temperature. Optics Communications 62 (2): 104-107.

- 56 Gayen, S. K., Wang, W. B., Petricevic, V., Dorsinville, R. and Alfano, R. R. (1985). Picosecond excite-and-probe absorption measurement of the  ${}^4T_2$  state nonradiative lifetime in ruby. Applied Physics Letters 47 (5): 455-457.
- 57 Gayen, S. K., Wang, W. B., Petricevic, V. and Alfano, R. R. (1986). Nonradiative transition dynamics in alexandrite. Applied Physics Letters 49 (8): 437-439.
- 58 Suchocki, A. B., Gilliland, G. D., Powell, R. C., Bowen, J. M. and Walling, J. C. (1987). Spectroscopic properties of alexandrite crystals II. Journal of Luminescence 37 (1): 29-37.
- 59 Zhang, Z. Y., Grattan, K. T. V. and Palmer, A. W. (1993). Thermal characteristics of alexandrite fluorescence decay at high temperatures, induced by a visible laser diode emission. Journal of Applied Physics 73 (7): 3493 - 3498.
- 60 Nelson, D. F. and Sturge, M. D. (1965). Relation between absorption and emission in the region of the R lines of ruby. Physical Review 137 (4A): A1117-A1130.
- 61 Weinstein, B. A. (1986). Ruby thermometer for cryobaric diamond-anvil cell. Review of Scientific Instruments 57 5: 910-913.
- 62 Stalder, M, Chai, B. H. T. and Bass, M. (1991b). Flashlamp pumped Cr:LiSrAlF<sub>6</sub> laser. Applied Physics Letters 58 (3): 216-218.
- 63 Zhang, Z. Y., Grattan, K. T. V. and Palmer, A. W. (1992b). Fiber optic temperature sensor based on the cross referencing between blackbody radiation and fluorescence lifetime. Review of Scientific Instruments 63 (5): 3177 - 3181.
- 64 Lakowicz, J. R. (1983). Principles of fluorescence spectroscopy. (New York and London: Plenum Press).
- 65 Best, R. E. (1984). Phase-Locked Loops Theory, Design, and Applications. (New York: McGraw-Hill).
- 66 Augousti, A. T., Grattan, K. T. V. and Palmer, A. W. (1987). A laser-pumped temperature sensor using fluorescent decay time of alexandrite. Journal of Lightwave Technology LT-5 (6): 759 - 762.
- 67 Noel, B. W., Turley, W. D., Lewis, W., Tobin, K. W. and Beshears, D. L. (1992). Phosphor thermometry on turbine-engine blades and vanes. In: the 7th International Symposium on Temperature, Toronto, 30 April, 1992.

- 68 Wickersheim, K. and Sun, M. (1985). Phosphors and fibre optics remove doubt from difficult temperature measurements. Research & Development (November): 114 - 119.
- 69 Evtuhov, V. and Neeland, J. K. (1966). Properties of ruby as a laser material. In: Laser, Volume I. Ed. by A. K. Levine. (London: Edward Arnold Ltd). pp. 13.
- 70 Fibreguide Industries (1989). Manufacturer's Data, 1989.
- 71 Johnson Matthey Ltd. (1989). "Easiflo" solder. Manufacturer's Data.
- 72 Burns, G. and Nathan, M. (1963). Quantum efficiency of ruby. Journal of Applied Physics 34 (3): 703 - 705.
- 73 Walling, J. C. and Peterson, O. G. (1980). High gain laser performance in alexandrite. IEEE Journal of Quantum Electronics QE-16 (2): 119 - 120.
- 74 Walling, J. C., Peterson, O. G. and Morris, R. C. (1980b). Tunable CW alexandrite laser. IEEE Journal of Quantum Electronics QE-16 (2): 120 - 121.
- 75 Hitz, C. B. (1981). News: Allied formally introduces alexandrite, pointing out wide range of applications. Laser Focus 17: 36 - 42.
- 76 Powell, R. C., Xi, L., Gang, X., Quarles, G. J. and Walling, J. C. (1985). Spectroscopic properties of alexandrite crystals. Physical Review B 32 (5): 2788-2797.
- 77 Henderson, B. and Imbusch, G. F. (1989). Optical spectroscopy of Inorganic solids. (Oxford: Clarendon Press).
- 78 McClure, D. S. (1962). Optical spectra of transition-metal ions in corundum. The Journal of Chemical Physics 36 (10): 2757 - 2779.
- 79 Bugos, A. R., Allison, S. W., and Cates, M. R. (1991). Laser-induced fluorescent properties of europium-doped scandium orthophosphate phosphors for high-temperature sensing applications. IEEE Proceedings of 1991 Southeast Conference 1&2: 1143 - 1147.
- 80 Meyer-Arendt, J. R. (1984). Introduction to Classical and Modern Optics. (New York: Prentice-Hall Inc.). pp.466 - 470.

- 81 Grattan, K. T. V., Palmer, A. W. and Willson, C. A. (1987b). A miniaturised microcomputer-based neodymium 'decay-time' temperature sensor. Journal of Physics E: Scientific Instruments 20: 1201-1205.
- 82 Wickersheim, K. A. and Hyatt, W. D. (1990). Commercial applications of fiberoptic temperature measurement. SPIE Proceedings 1267: 84 - 96.
- 83 Harmer, A. L. (1986). Fibre optic sensors for offshore process control instrumentation. In: Proceedings of Optical Fibre Sensors Conference (OFS '86), Informal Workshop at Tusukuba Science City, 1986, VII. Pub: Institute of Electronics and Communication Engineers of Japan, Tokyo, 1986.
- 84 Grattan, K. T. V. and Palmer, A. W. (1985). Infrared fluorescence "decay-time" temperature sensor. Review of Scientific Instruments 56 (9): 1784 - 1787.
- 85 Selli, R. K. (1987). Fibre optic temperature sensors using fluorescent phenomena. PhD Thesis. (London: City University).
- 86 Armagan, G. and Bartolo, B. D. (1988). Mechanism for the thermal dependence of the Cr to Nd energy transfer in garnets. IEEE Journal of Quantum Electronics 24 (6): 974 - 978.
- 87 Healy, S. M., Donnelly, C. J., Glynn, T. J., Imbusch, G. F. and Morgan, G. P. (1990). Temperature dependence of the luminescence of GSGG:Cr<sup>3+</sup>. Journal of Luminescence 46 (1): 1 - 7.
- 88 Andrews, L. J., Beall, G. H., and Lempicki, A. (1986). Journal of Luminescence 36: 65 - 75.
- 89 Rasheed, F., O'Donnell, K. P., Henderson, B. and Hollis, D. B. (1991). Disorder and the optical spectroscopy of Cr<sup>3+</sup> -doped glasses: I. Silicate glasses. Journal of Physics - Condensed Matter 3 (12): 1915 - 1930.
- 90 Henderson, B., Yamaga, M., Gao, Y. and O'Donnell, K. P. (1992). Disorder and nonradiative decay of Cr<sup>3+</sup> -doped glasses. Physical Review B 46 (2): 652 - 661.
- 91 Draxler, S. and Lippitsch, M. E. (1993). Optical sensors based on fluorescence decay time. Proceedings of the Symposium on Chemical Sensors II, Proceedings 93-7, ed. by M. Butler *et al.* (Pennington: The Electrochemical Society): 69 -73.

- 92 Lippitsch, M. E., Pusterhofer, J., Leiner, M. J. P. and Wolfbeis, O. S. (1988). Fibre-optic oxygen sensor with the fluorescence decay time as the information carrier. Analytica Chimica Acta 205 (1-2): 1 - 6.
- 93 Menoni C. S. and Spain, I. L. (1983). Ultra-high pressure measurement. In: High Pressure Measurement Techniques, ed. by G. N. Peggs. (London and New York: Applied Science Publishers): 125 - 175.
- 94 Eggert, J. H., Goettel, K. A. and Silvera, I. F. (1989). Ruby at high pressure - II. Fluorescence lifetime of the R line to 130 GPa. Physical Review B 40 (8): 5733 - 5738.
- 95 Kottke, T. and Williams, F. (1983). Pressure dependence of the alexandrite emission spectrum. Physical Review B 28 (4): 1923 - 1927.
- 96 Jia, W., Shang, Y. S., Tang, R. M. and Yao, Z. Y. (1984). Pressure effects of fluorescence R-lines of chrysoberyl  $\text{BeAl}_2\text{O}_4:\text{Cr}^{3+}$ . Journal of luminescence 31 & 32: 272 - 274.
- 97 Jähren, A. H., Krüger, M. B. and Jeanloz, R. (1992). Alexandrite as a high-temperature pressure calibrant, and implications for the ruby-fluorescence scale. Journal of Applied Physics 71 (4): 1579 - 1582.



## Appendix B:

### A list of publications by the author relevant to the thesis:

---

1. Zhang, Z.Y., Grattan, K.T.V. and Palmer, A.W. (1993). Temperature dependences of fluorescence lifetimes in Cr<sup>3+</sup> -doped insulating crystals. Physical Review B 48 (11): 7772-7778.
2. Zhang, Z.Y., Grattan, K.T.V. and Palmer, A.W. (1993). Phase-locked detection of fluorescence lifetime. Review of Scientific Instruments 64 (9): 2531-2540.
3. Zhang, Z.Y., Grattan, K.T.V. and Palmer, A.W. (1993). Temperature dependences of fluorescence decay in Cr<sup>3+</sup> doped insulating crystals for thermometric applications. Paper to be presented on the 5th Symposium on Temperature and Thermal Measurement in Industry and Science, Prague, November 1993.
4. Zhang, Z.Y., Grattan, K.T.V. and Palmer, A.W. (1993). Fiber optic thermometry based on fluorescence lifetimes of Cr<sup>3+</sup> doped materials. In: ISMTII '93 - Second International Symposium on Measurement Technology & Intelligent Instruments, Wuhan - Three Gorges - Chongqing, China, 29 October - 5 November, 1993. SPIE Proceedings 2101 (1): 476 - 482.
5. Zhang, Z.Y. (1994). Amplifiers. In: Concise encyclopedia of measurement and instrumentation, ed. by L. Finkelstein and K.T.V. Grattan. (Oxford: Pergamon Press).
6. Zhang, Z.Y., Grattan, K.T.V. and Palmer, A.W. (1993). Thermal characteristics of alexandrite fluorescence decay at high temperatures, induced by a visible laser diode emission. Journal of Applied Physics 73 (7): 3493 -3498.
7. Zhang, Z.Y., Grattan, K.T.V. and Palmer, A.W., Summers, R., Summan, R., Hughes, S. (1993). Cr:LiSAF fluorescence lifetime based fiber optic thermometer and its applications in clinical RF heat treatment. In: International Conference of Biomedical Optics '93, Los Angeles, California, USA, Jan. 1993. SPIE Proceeding 1885: 300 - 305.
8. Zhang, Z.Y., Grattan, K.T.V. and Palmer, A.W. (1993). Phase-locked detection of fluorescence lifetime and its thermometric applications. In: International Conference of Biomedical Optics '93, Los Angeles, California, USA, Jan. 1993. SPIE Proceedings 1885: 228 - 239.

9. Zhang, Z.Y., Grattan, K.T.V. and Palmer, A.W. (1992). Fiber-optic high-temperature sensor based on the fluorescence lifetime of alexandrite. Review of Scientific Instruments 63 (8): 3869-3873.
10. Zhang, Z.Y., Grattan, K.T.V. and Palmer, A.W. (1992). Fiber optic temperature sensor based on the cross referencing between blackbody radiation and fluorescence lifetime. Review Scientific Instruments 63 (5): 3177-3181.
11. Zhang, Z.Y., Grattan, K.T.V. and Palmer, A.W. (1992). Sensitive fiber optic thermo-meter using Cr:LiSAF fluorescence for bio-medical sensing applications. In: 8th Optical Fiber Sensors Conference, Monterey, California, Jan. 1992, Proceedings. IEEE Lasers and Electro-Optics Society and Optical Society of America, pp.93-96.
12. Zhang, Z.Y., Grattan, K.T.V. and Palmer, A.W. (1991). A novel signal processing scheme for a fluorescence based fiber-optic temperature sensor. Review of Scientific Instruments 62 (7): 1735-1742.
13. Grattan, K.T.V., Palmer, A.W. and Zhang, Z.Y. (1991). Development of a high-temperature fiber-optic thermometer probe using fluorescent decay. Review of Scientific Instruments 62 (5): 1210-1213.
14. Zhang, Z.Y., Grattan, K.T.V. and Palmer, A.W. (1991). A novel signal processing scheme for a ruby-fluorescence-based fiber optic temperature sensor. SPIE Proceedings 1511: 264-274.